Department of Precision and Microsystems Engineering

Photonic Micro-Mechanical Acoustic Emission Sensors for Untrasonic Non-Destructive Testing

Xinshuo Zhang

Report no : 2023.079
Coach : Dr. Peter Steeneken, Dr. Wouter Westerveld
Professor : Dr. Peter Steeneken, Dr. Wouter Westerveld
Type of report : MSc. Thesis
Date : 24 August 2023

Graduation Thesis

Photonic Micro-Mechanical Acoustic Emission Sensors for Ultrasonic Non-Destructive Testing

Msc. Mechanical Engineering
Xinshuo Zhang

Delft University of Technology

TU Delft

Graduation Thesis

Photonic Micro-Mechanical Acoustic Emission Sensors for Ultrasonic Non-Destructive Testing

by

Xinshuo Zhang

Student Name	Student Number
X. Zhang	5464676

Supervisor:	P. Steeneken
	W. Westerveld
Project Duration:	Aug, 2022 - Aug, 2023
Faculty:	3ME Department, Delft

Cover by Xinshuo Zhang

TU Delft

Abstract

Non-Destructive Testing (NDT) of infrastructures has become an increasingly prominent topic in contemporary society with great significance in terms of safety, economy and environmental protection. Acoustic Emission (AE) technology is a representative NDT technology based on passive ultrasonic guided waves, which has the advantages of large coverage, low energy consumption and rapidity but also puts forward higher requirements on performance specifications of sensors, such as sensitivity, bandwidth, signal-to-noise ratio and miniaturization. Silicon photonics employs silicon as an optical medium to create sub-micron precision photonic systems, which provides promising scope for next-generation sensors with ultra-high sensitivity, small footprint and special functionalities. Oriented towards the requirements from AE applications, this project proposes the first silicon photonic micro-mechanical AE sensor based on micro-machined membranes, with an ambition of replacing the conventional piezoelectric sensors. The prototype design presented in this work includes two options with different cladding materials, which is capable of a peak velocity sensitivity of more than $75 dB[V/(m/s)]$ and a wide operating frequency range of $100 \sim 1000\ kHz$. The overall performance of the proposed design is comparable to that of mainstream piezoelectric AE sensors, while the footprint is reduced to about $1/40$. In the design process, a complete design methodology for opto-mechanical AE sensors is developed, which allows rapid design with good agreement with simulation results.

Contents

1

Introduction

With the development of civil engineering, the application of a wide range of construction materials has enabled highly functional, highly reliable and complex architectural structures. Structural steel, as a typical example, refers to a category of steel used in the manufacture of architectural constructions. Being one of the most common materials used in commercial and industrial building constructions [1], structural steel usually has high strength, stiffness, toughness and good ductility, and can be machined into varieties of shapes. Depending on the requirements, the composition, size, cross-sectional shape and other parameters of the steel can be changed to achieve different functions. Modern construction materials, represented by structural steel and concrete, enable the rapid and cost-efficient construction of infrastructure and have significantly extended the service life. This has not only brought many conveniences to our lives but also been the cornerstone for the further spread and development of human civilization.

However, the increase in service life inevitably leads to an accumulation of risk of structural damage and degradation. Such process may occur in different forms such as corrosion, fatigue cracking and strength reduction [2, 3]. The extent of these regimes usually depends on the applied loads and external environment, but are also related to the properties of the material itself, such as corrosion resistance, micro characteristics, crystal orientation and grain boundary structures [4]. At one time, the assessment, inspection and maintenance of architectural structures were mainly based on preventive approaches. However, for lack of real-time feedback, such methods are not able to deal with unpredictable loading events. For modern buildings with complex structures and large scale, the need for safety can no longer be fulfilled by preventive engineering calculations alone. In fact, the maintenance, restoration and improvement of potentially degraded infrastructures has become a major issue for human society on many levels. From an economic point of view, the absence of timely maintenance of infrastructure can lead to high costs of reconstruction [5]. In addition, studies [6] have shown that building construction projects have a significant impact on the environment in terms of pollution, resource use and habitat destruction. From an environmental perspective, improving the lifetime of infrastructures and achieving efficient use of construction materials through proper structural monitoring are of great ecological importance.

In this context, the *non-destructive testing (NDT)* and *structural health monitoring (SHM)* techniques for architecture constructions have emerged and are of increasing importance in the health assessment, *remaining useful life (RUL)* prediction and *condition-based maintenance (CBM)* of building structures [7]. NDT and SHM technology is concerned with identifying and characterising defects on the surface and interior of materials or components without cutting or otherwise altering the original properties of the object [8], thus causing little to none damage to the surface texture, structural integrity and future usefulness. In general, NDT technology starts with data collection by multiple mount-on sensors. The signals are then interpreted and attributed to provide reliable guidance for maintenance. Various approaches, such as ultrasonic bulk waves [9], X-ray Computed Tomography (CT) [10, 11, 12] and infrared thermography [13, 14, 15], have been developed for the health evaluation of structures. Though having successful applications, the above methods show weaknesses of being cumbersome and slow in the inspection of large structures. In contrast, the *ultrasonic guided waves (UGW)* [16] offers a highly advantageous solution. Guided wave inspection was originally applied for integrity assessment

of large-scale pipelines. Owing to the unique ability to be self-confined in thin-wall structures, guided waves can achieve large-scale and long-distance propagation with minimal attenuation and energy loss [17], and are thus capable of identifying defects with considerable sensitivity and high efficiency at large distances. UGW technology can fit for various architectural materials and has been used for non-destructive testing of structural steel, concretes, pipes and functional coatings.

UGW technology can be broadly divided into two categories depending on the generation of guided waves, as illustrated in Fig. 1.1. Active UGW techniques artificially generate ultrasonic signals with external sources, such as piezoelectric actuators, while passive UGW techniques work with noise generated spontaneously by structural defects. *Acoustic emission (AE)* technology is a typical passive UGW technique, whose working principle and operation methodology will be discussed in detail in Chapter. 2. Briefly, the acoustic emission technique is based on the detection of the generation and growth of structural damages by means of passive sensors on the surface of objects. It has the following advantages over conventional NDT techniques:

- As a passive method, AE technology does not require wave sources and therefore consumes less energy.
- AE technology is able to capture the ongoing deterioration in real-time without any disturbance to the specimen.
- AE technology involves ultrasonic sensors fixed to the surface of the specimen in a proper distribution, without being moved around or the access to both side of the structure.
- Damage processes can observe during the entire load history without the need to stop loading as is the case with, for example, ultrasonic analysis techniques.

In addition, AE technology provides direct reflection of failure mechanisms and allows remote operation. The application of AE technology is expected to significantly reduce the long-term cost in structural health monitoring, saving human resources and energy consumption in the process.

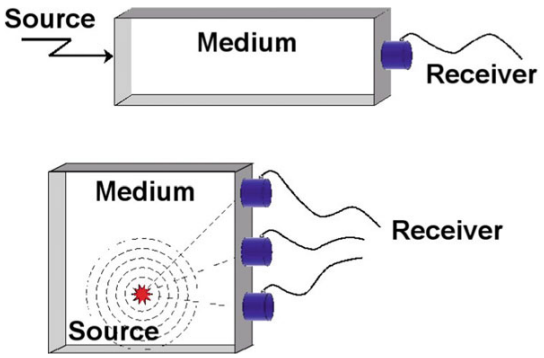

Figure 1.1: Working principle of active and passive UGW technologies, reproduced from [18].

However, it is currently still not realistic for AE technology to stand alone but more suited to be complementary to other NDT technologies due to some challenges, including but not limited to:

- AE technology is not capable of detecting damage that does not change over time.
- AE technology can only detect and localize defects without any detailed description on, for example, their shape or size.
- For non-homogeneous materials, such as concrete, signals with a wavelength comparable to the scale of scattered inclusions may produce dissimilar acoustic emission results.
- AE signals are usually quite weak, thus placing higher demands on both sensor performance and signal post-processing.

This paper takes AE technology as the main research background. In a general workflow, the acoustic emission waves can be detected by an array of sensors from a distance, and the location of the noise source can be deduced from the signal waveform and arrival time recorded by each sensor. During this process, the application of high performance sensors plays a very important part, which

largely determines the signal recognition capability, detection range and positioning accuracy of the system.

Varieties of high performance sensors have already been developed, whose successful application has contributed significantly to the maturity and diffusion of AE technology. As the relevant fundamental science advances, there is also expectation that sensors based on different operating principles will be applied to AE technology to achieve sensitivity or functionality beyond that of conventional sensors. Photonic micro-mechanical sensors are an prospective alternative that applies light as the signal carrier and is fabricated with micro-machining technology. As some prototypes have been developed, their potential in the field of high-performance sensing technology is gradually attracting attention. For Non-destructive testing based on AE technology, it is of great interest to understand the capabilities of photonic micro-mechanical sensors and to explore the prospects for their application, which is the main research question of this project.

In the present project, an opto-mechanical ultrasonic wave sensor based on the silicon photonic platform is investigated. The primary design target is to replace conventional piezoelectric sensors in ultrasonic guided wave NDT instruments based on acoustic emission technology to achieve comparable or even higher performance. To achieve this, the thesis presents a pioneering membrane-based opto-mechanical sensor configuration. Due to the lack of information about fabrication and testing, this work employs some assumptions in order to obtain as specific a design solution as possible. For the wide range of possibilities that may be faced in practice, design guidelines for different realities are provided. Finally, on the basis of design evaluation and reflection, an outlook for future work is performed.

The thesis is organised as follows. In Chapter. 2, the acoustic emission technology is introduced in terms of the physical mechanism, operation principles and sensing technology. Chapter 3 provides a brief introduction on silicon photonics, followed by the fundamentals of optical waveguides and micro-ring resonators. An example of optical micro-machined ultrasonic sensors is also provided. In Chapter 4, technical specifications are presented, based on the technical specifications provided by the company SHM-Next. Fundamentals of fabrication technologies are also introduced as a basis for design. Conceptual design is proposed in Chapter. 5. Chapter 6 provides the modeling and simulation strategies. In Chapter 7, 8, the opto-mechanical system is decomposed into mechanical and optical aspects, in which design methodology and criteria are presented and explained on the basis of theoretical analyses. A complete opto-mechanical design is performed in the first part of Chapter. 9, followed by two prototype designs with design process, assessment and reflections. A design proposal and the conclusion are provided in Chapter 10 to provide a complete presentation for the final design and future outlooks for the company.

2

Acoustic Emission Technology

2.1. Acoustic Emission

Acoustic emission (AE) technology is one of the promising approaches for ultrasonic guided wave inspection [19]. In any material or structure, the redistribution of local stress generates noise, which is known as acoustic emission. The identification and localisation of noise sources, often referred to as acoustic emission events, are the main objectives in the implementation of AE technology for structural inspection.

Before going any further into specific discussions on techniques, it is necessary to understand the mechanisms by which the AE phenomenon occurs. Acoustic emission can be thought of as tiny earthquakes in the material. Crack initiation and growth is one of the most important AE sources. As a crack is generated, its dimensions increase suddenly from zero. The formation of new surfaces causes sudden changes in stress and displacement of material in the vicinity of the crack [20]. This is accompanied by a rapid release of energy, which propagates in the form of high frequency elastic waves ranging from $20\ kHz$ to $1\ MHz$ [21, 22]. In addition to crack growth, such transient elastic waves may also be generated by dislocation movement, plastic deformation, crack face fretting or fibre breakage. The energy of acoustic emission is usually proportional to the strain energy released from the newly generated crack surfaces [23].

There are two main types of acoustic emissions, as shown in Fig. 2.1. Burst emission refers to discrete signals caused by individual AE events, while continuous emission demonstrates sustained signals due to constant friction or intensive AE events. Since most AE techniques are developed for dealing with burst emission, only discrete signals will be considered in the following discussion.

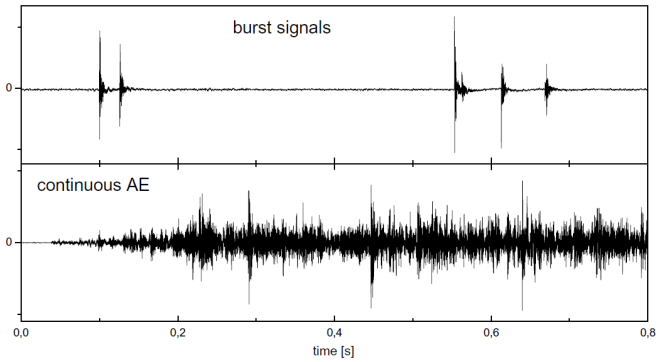

Figure 2.1: Examples of burst and continuous acoustic emission waves, reproduced from [18].

In most cases, the high frequency elastic waves of acoustic emission are detected by transducers attached to the surface of the structure. The arrival time recorded by distributed sensors corresponds to the propagation distances, and the crack location can be subsequently determined with triangulation algorithms [24]. Fig. 2.2 provides an illustration of the localization strategy. In conventional AE systems,

each sensor captures an ultrasonic wave signal exceeding a set threshold, from which the maximum value of amplitude is picked as a representative. By multiplying the arrival time detected at each sensor by the speed of sound, the distance from the sensor to the wave source can be inverted, labelled as d_1, d_2 and d_3 in Fig. 2.2. The position of the wave source can be uniquely determined by considering the calculated distances from at least three sensors. In this method, correct guided wave information, such as mode and speed, and precise time measurements are essential for achieving the detection and localization of small structural damage. The former relies heavily on proper sensor arrangement and signal processing, while the latter is more dependent on sensor performance.

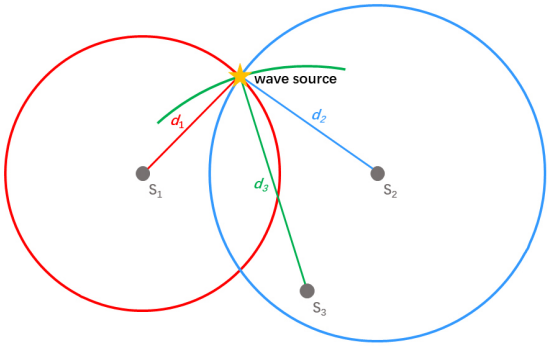

Figure 2.2: Schematic diagram of the triangulation searching strategy.

As an example of the application of AE technology in constructions, the health monitoring of steel bridges provides a good indication of its principles [25]. In steel bridges, the fatigue crack in deck plates at part intersections is an important cause of structural failure. Under external loads, the cracks will grow until they completely penetrate the deck plates. AE technology, enabled by its high sensitivity and large inspection area, is an ideal means of carrying out real-time monitoring over these cracks. SHM Next in the Netherlands has implemented AE technology for the health monitoring of steel bridges, obtaining good results in both laboratory and practical tests. AE technology has also been successfully demonstrated for structural health monitoring of composite materials and concrete structures [26]. During the tests, a full-size prestressed concrete bridge was subjected to a series of loading and unloading cycles where the load progressively increased until its failure. By analysing the recorded data, AE techniques were proved effective for structural monitoring and damage identification.

However, according to current researches, specific challenges for the application of AE techniques have emerged in structural health monitoring. A typical problem is wave mode identification. Ultrasonic guided waves are multi-modal in character. In thin-wall metallic structures, AE signals can be described as a combination of multiple wave modes, among which the two most contributing ones are namely *symmetric (S0)* and *antisymmetric (A0)* Lamb waves. For a certain AE signal, different frequency components propagate at different speeds. As the propagation distance increases, the amplitude of the signal decreases, which is referred to as the dispersion phenomenon. Stronger dispersion indicates a sharper decay of the wave amplitude with regard to distance. The dispersion of S0 and A0 Lamb waves is usually different for a given operating frequency range, as shown in Fig. 2.3, which may result in a change in the relative wave amplitude when being detected.

In conventional AE systems, each sensor determines the arrival time of acoustic waves by capturing the maximum amplitude signal above a pre-set threshold. Therefore, for acoustic emission systems that utilize distributed sensors for localization, the correct identification of wave modes and the correspondent sound speed becomes an important issue. Switching of the dominant wave mode may occur among different sensor locations, and the wrong identification of wave modes can lead to incorrect distance estimation or even failure to find cracks. As an example, the dispersion of S0 and A0 waves at $0.5\,m$ and $2\,m$ away from a simplified AE source is shown in Fig. 2.4, where the ratio of the S0 to A0 waves is set $6/5$ at the source. After $0.5\,m$ of propagation, the S0 wave remains dominant, while the A0 wave takes over as the dominant wave at $2\,m$ away due to weaker dispersion.

A feasible solution for this problem is the *quasi-beamforming (QBF)* technology [25]. In this approach, acoustic wave sensors are installed in close proximity to each other to minimize the effects of interfering factors such as dispersion, signal attenuation and structural geometry variation in the measurement area. Based on the guided wave characteristics and the arrival time of the signals, a

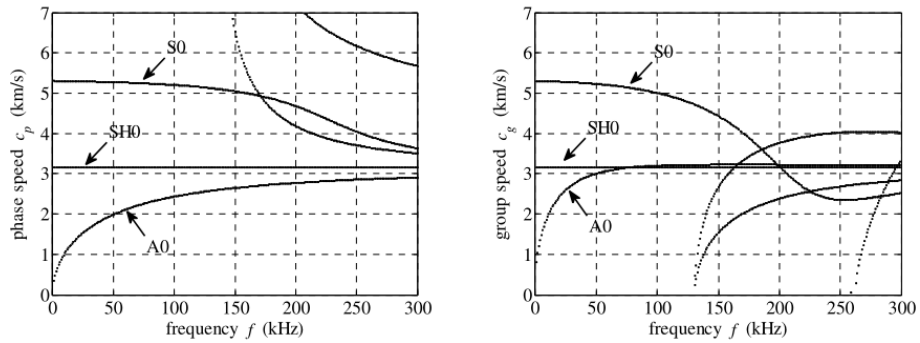

Figure 2.3: The dispersion curves for a $12\ mm$ thick steel plate: phase speed and group speed, reproduced from [25]

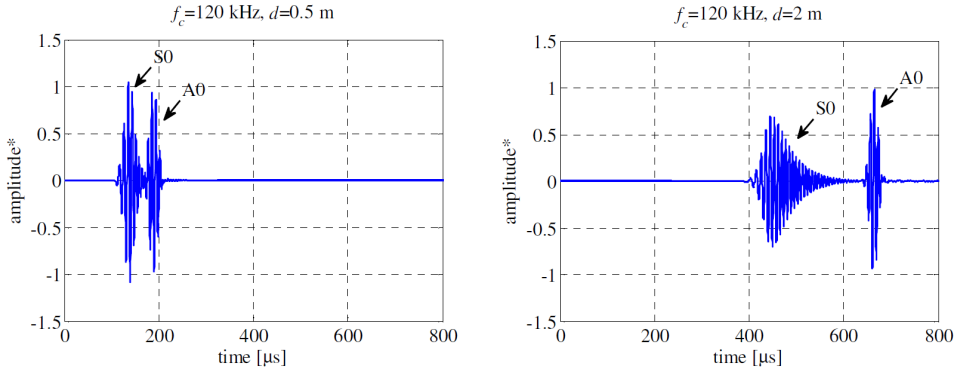

Figure 2.4: The AE signals simulated at $0.5\ m$ and $2\ m$ away from the AE source, reproduced from [25]

beamforming formulation for locating the wave source is derived and the wave speed is estimated. For each set of recorded waveforms, the most reasonable wave mode is determined in an optimization routine in accordance with the dispersion curves. Practical tests have been carried out in a section of the Van Brienenoord bridge in Rotterdam [25]. Compared to the conventional acoustic emission devices, an improved localization map of fatigue cracks is obtained, while the cost and effort for instrument installation is reduced.

In addition to wave mode identification, precise guided wave detection also has a direct impact on the practical results of AE systems. Sensor performance is one of the most influential factors on the detection result, which fundamentally determines the accuracy of signal measurement. Some solutions have already been proposed for AE wave detection and will be discussed in detail in the next section. As prior knowledge, the operating principle and performance specifications of AE sensor are first introduced.

2.2. Sensing Technology

In principle, acoustic emission signals are first detected in the form of motion at the surface of the structure and are subsequently converted into electrical signals by transducers. For common plate-like metallic structures mentioned in Section 2.1, the wavelength of dominant Lamb waves is comparable to the plate thickness [18], which is much larger than the scale of AE sensors. Thus, the input signal of spatially fixed AE sensors can be expressed as one-dimensional motion perpendicular to the surface with only time variable t. The sensor response is mathematically formulated as

$$g(t) = L\left[f(t)\right] \tag{2.1}$$

Eq. 2.1 can be illustrated by the linear system in Fig. 2.5, where the input $f(t)$ of the surface motion is converted to the electrical output $g(t)$ by transfer function L of the AE sensor.

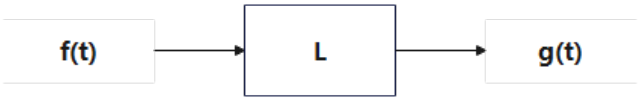

Figure 2.5: Schematic diagram of a linear system.

By definition, the input $f(t)$ can be expressed as its convolution with the Dirac delta function $\delta(t)$

$$f(t) = f(t) * \delta(t) \tag{2.2}$$

where the symbol $*$ refers to the convolution, defined by

$$a(t) * b(t) = \int a(t-\tau)b(\tau)d\tau \tag{2.3}$$

Thus, for a linear system, Eq. 2.1 can be transformed into

$$g(t) = L\left[f(t) * \delta(t)\right] = f(t) * L\left[\delta(t)\right] = f(t) * w(t) \tag{2.4}$$

where $w(t)$ or $L\left[\delta(t)\right]$ refers to the impulse response of the system. The Fourier transform of the above equation yields

$$G(f) = F(f)W(f) \tag{2.5}$$

where $G(f)$, $F(f)$ and $W(f)$ are respectively the Fourier transforms of $g(t)$, $f(t)$ and $w(t)$. Eq. 2.4 and Eq. 2.5 represents the response of the sensor to input signals in the time and frequency domains. $W(f)$ is also often referred to as the transfer function or frequency response of the sensor, which actually represents the impulse response. In practice, the characterization of AE sensors is usually equivalent to the determination of the frequency response $W(f)$.

2.2.1. Performance Specifications

For typical AE systems, the most important performance specification of sensors is *sensitivity*. In practice, the AE signal amplitude is affected by many factors, such as wave dispersion, material attenuation, geometrical spreading and medium discontinuities, combined with external noises from traffic and weather, etc [25]. Therefore, despite the theoretically low attenuation and long propagation distance of UGW, the strength of AE signals can diminish dramatically a few meters away from the source in reality. Sensors with higher sensitivity are supposed to capture the subtle signals more effectively, enabling a larger range of damage detection and localization. In addition, the *bandwidth* determines the availability of sensors for signals around the centre frequency. Larger bandwidth enables the detection of AE signals over a larger frequency range. The matching of sensor bandwidth to the propagation characteristics of UGW is one of the main concerns of current AE technology.

The overall performance of AE sensors can be characterised by the so-called *frequency response curves* or *calibration curves*. An example is provided in Fig. 2.6

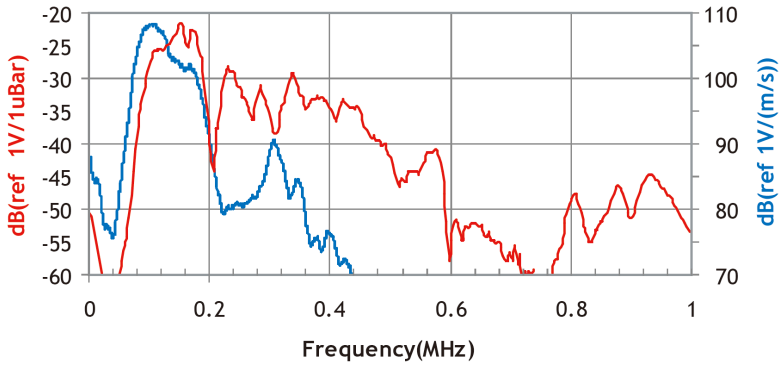

Figure 2.6: Frequency response curve of R15I-AST Sensor® by Physical Acoustics.

In the plot, the performance of the AE sensor is represented with curves of frequency response over a given frequency range. The unit $[dB(V/\mu bar)]$ stands for the voltage output $[V]$ per unit acoustic pressure input, which is not considered in the present design, and the other unit $[dB(V/(m/s))]$ will be explained later.

In practice, high sensitivity and large bandwidth are usually not available simultaneously on AE sensors. Depending on their characteristics, AE sensors can be classified into two main types, namely resonant and broadband sensors. Resonant sensors usually provide higher sensitivity within a narrow frequency range around the resonance, while broadband sensors allow larger detection range with relatively flat sensitivity. Examples for typical frequency responses of the two types are provided in Fig. 2.7.

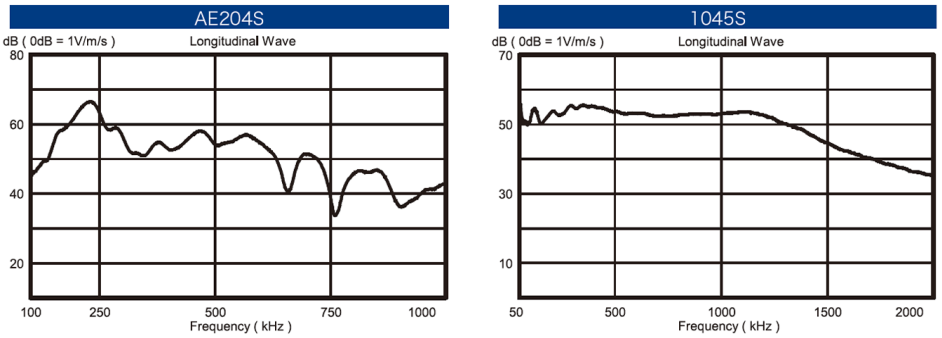

Figure 2.7: Frequency response curves of resonant AE204S® and broadband 1045S® acoustic emission sensors by Fuji Ceramics Corporation.

In engineering application, the sensitivity and bandwidth of AE sensors are defined in various ways depending on the usage scenario and sensor type.

Sensitivity

The sensitivity of AE sensors is generally defined as the voltage response to input motion signals, of which two commonly used are *displacement sensitivity* and *velocity sensitivity*.

From the perspective of the sensor principle, such voltage response is directly made to local displacement signals of certain frequencies by the elastic elements inside AE sensors. This type of frequency response is called *displacement sensitivity*, expressed by the unit $[V/nm]$. The displacement sensitivity directly determines the possibility of AE sensors with a certain noise level to detect signals at a given frequency. According to the current state of the art, displacement signals down to $1\,nm$ scale can be detected by mainstream AE sensors.

On the other aspect, as introduced in Section 2.1, the AE signal is fundamentally rapid energy release brought about by permanent deformation or cracking of materials, normally in the form of pulse-like stress wave. Considering that the energy of waves propagating in solid is directly reflected by the particle velocity, the frequency response to normal velocity on the surface describes more intuitively the sensitivity of AE sensors to signals with certain intensity. Therefore, from the prospective of AE mechanism, the sensitivity of AE sensors can also be represented by their voltage output per unit velocity, with the unit $[V/(m/s)]$. Such kind of frequency response is named as *velocity sensitivity*.

In engineering applications, the velocity sensitivity is also commonly defined in terms of a logarithmic function, as

$$Velocity\ \ Sensitivity\,[dB] = 20\log_{10}\left(\frac{Velocity\ \ Sensitivity\,[V/(m/s)]}{1\,[V/(m/s)]}\right) \tag{2.6}$$

It should be noted that the sensitivity in either unit should be specified simultaneously with the signal frequency. Therefore, there is no essential difference between the displacement and velocity sensitivity, which can be converted into each other by the factor $2\pi f$ [27].

On the plot of frequency response curves, the sensitivity of AE sensors at a given frequency can be derived from the corresponding value of response. For example, the R15I-AST Sensor® in Fig. 2.6 offers a velocity sensitivity of about $75 \sim 109\,dB$ in the range of $50 \sim 400\,kHz$, with the maximum sensitivity obtained at around $100\,kHz$. It is noted that many commercial AE sensors are integrated

with pre-amplifiers. For example, the above mentioned R15I-AST Sensor® comes with a $40\ dB$ pre-amplifier, thus the actual sensitivity of the piezoelectric element ranges from about 35 to $69\ dB$.

Bandwidth

The bandwidth of AE sensors is more commonly referred to in engineering as the *operating frequency range*, representing the range of frequency where the sensors are able to provide sufficient response.

There are multiple ways to define the operating frequency range of AE sensors. For broadband sensors, it usually refers to the frequency range of smooth response. For resonant sensors, which are significantly more sensitive at resonance frequencies, the operating frequency range usually refers to the range corresponding to a $10\ dB$-drop response than maximum. Alternatively, the range where the responses are greater than a set value, such as $50\ dB$, is also considered as the operating frequency range of sensors in many applications.

Most of the above definitions are generated from conventional piezoelectric AE sensors. Since the response of piezoelectric AE sensors is based on the complex constitutive laws of piezoelectric materials such as lead zirconate titanate (PZT) [18], it is hardly the case that the frequency response curves present a regular shape. Thus, in the definition of sensor bandwidth, individual low-response dips within the frequency range are usually ignored in favor of the overall response level of sensors.

On frequency response curves, the bandwidth of AE sensors can be estimated with the frequency range where the required sensitivity is satisfied. For example, it is claimed on the data sheet of R15I-AST Sensor® that the sensor operates within the range of$50 \sim 400\ kHz$, which implies that the third definition above is employed and the threshold is set to $35\ dB$ without the pre-amplifier.

Other Specifications

For actual AE sensors, the *signal-to-noise ratio (SNR)* or *noise level* is often taken into consideration. The higher the SNR, the more likely it is that the sensor is able to isolate AE signals without omissions. The miniaturisation of sensors is also of great interest for AE applications, especially QBF technology, due to the need for proximity among sensors to avoid possible wave mode confusions.

2.2.2. State-of-Art Acoustic Emission Sensors

The state-of-art AE sensors in research and practical applications can be broadly classified into two main categories: *piezoelectric sensors* and *micro-electro-mechanical-system (MEMS) sensors*. An introduction to their respective operation principles, state-of-art development, advantages and challenges is given as follows.

Piezoelectric Sensors

Piezoelectric transducers are widely used for ultrasonic detection in medical imaging and industrial structural health monitoring [28]. The physical basis of piezoelectric transducers is the piezoelectric effect of materials, first discovered by French physicists Jacques and Pierre Curie in 1880 [29]. Under applied loads, certain solid materials, such as crystals, ceramics and piezoelectric polymers, experience electric charge accumulation in response to mechanical stress. In this process, mechanical signals are converted into electrical signals that can be read out directly by electrical interrogation systems.

Piezoelectric sensors have long been one of the main components of active and passive UGW technology. One of the most outstanding features of piezoelectric sensors compared to other types is that they can act as either sensors or actuators, relying on opposite signal conversion pathways. Since active wave sources are not needed in AE systems, piezoelectric sensors work exclusively on signal detection and are available in both resonant and broadband types. The typical structure of piezoelectric resonant AE sensors is shown in Fig. 2.8.

At present, one of the most prospective studies on piezoelectric AE sensors is about embedded sensors, especially cement-based piezoelectric composites with cement as the matrix and ceramics as the functional phase, which offer the prospect of improving the compatibility of piezoelectric sensors with construction materials [30]. Recently, feasibility tests for type 1-3 cement-based piezoelectric sensors have been carried out on large bridge structures [31], with increased operating frequency of $20 - 1000\ kHz$ and enhanced signal recognition ability.

Piezoelectric sensors have gained much popularity mainly due to their stability, accessibility, technical maturity and cost advantages, which are currently the most common type of sensor in AE techniques

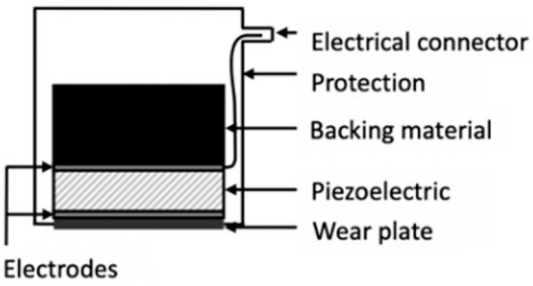

Figure 2.8: Structure of typical AE sensors based on PZT elements, reproduced from [18].

[32]. The downside is, as mentioned above, the operation of conventional piezoelectric AE sensors relies on the intrinsic constitutive laws of piezoelectric materials, resulting in limited design space. Due to the complexity of the constitutive laws, it is difficult to find analytical solutions in three-dimensional cases. Therefore, the analysis of piezoelectric sensor performance in design phase is usually carried out with the finite element method (FEM), which hinders the designers' prediction and understanding of the final outcomes to some extent. In addition, the difficulties with miniaturisation and large-scale electrical wiring for transducer arrays have called for technique iterations to achieve higher performance, efficiency and reliability.

Micro-Electro-Mechanical-System (MEMS) Sensors

Micro-electro-mechanical-system (MEMS) sensors are a promising alternative for conventional piezoelectric sensors. These sensors are designed and manufactured based on micro-machining techniques [33], allowing for system miniaturisation and mass manufacturing.

Jan Niklas Haus et al. [34] have proposed a piezoresistive MEMS ultrasonic vibrometer that integrates a micro cantilever beam into a microcircuit. The micro cantilever beam is processed by laser-contouring the deformation-sensitive silicon membrane of a cavity-in-glass pressure sensor [35], the root of which is connected to a p-doped piezoresistor, as shown in Fig. 2.9. The incoming ultrasonic guided waves trigger a local displacement at the measurement site, which drives the micro cantilever beam to vibrate. The deformation brought by vibration leads to a resistance change, which is then converted by a Wheatstone bridge into electrical signals. There are actually two signal conversions in the process. The acoustic pressure signal is first converted to the deformation of the micro cantilever beam, and then to the potential difference in the circuit, which can be measured and recorded by an external electrical system. The change in resistance is the key intermediate link in the whole signal conversion process, and the sensitivity of the sensor is determined by both the bending stiffness of the micro cantilever beam and the piezoresistivity coefficient of the p-doped piezoresistor. The functionality and usability of the MEMS vibrometer have been demonstrated on a customized test rig.

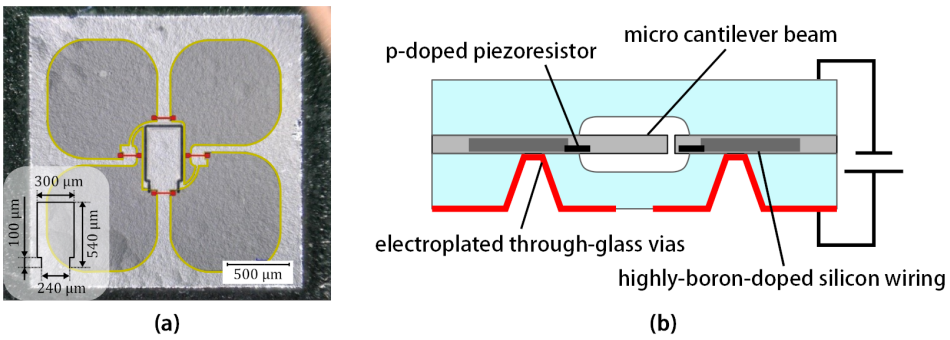

Figure 2.9: (a) Microscopic image of the chip surface before encapsulation, showing the laser cuts in the silicon membrane and the Wheatstone bridge doping scheme, reproduced from [34]. (b) Schematic cross-sections of the MEMS sensor for UGW structural health monitoring, adapted from [34].

Apart from piezoresistive MEMS sensors, piezoelectric and capacitive MEMS ultrasonic transducers (PMUTs and CMUTs) have already been developed for AE sensing [33]. PMUTs are developed on the basis of thin film deposition techniques, by which micro resonators with piezoelectric layers can be

fabricated [36]. Similar to conventional piezoelectric sensors, the AE waves induce mechanical strain on the resonators, resulting in electrical displacements. CMUTs are based on the principle of capacitors, which converts local displacement brought up by AE waves into changes in capacitance. Fig. 2.10 shows a broadband CMUT developed and characterized by P.Batuad et al. [37]. A signal-to-noise ratio of $20\,dB$ at the resonance frequency is achieved.

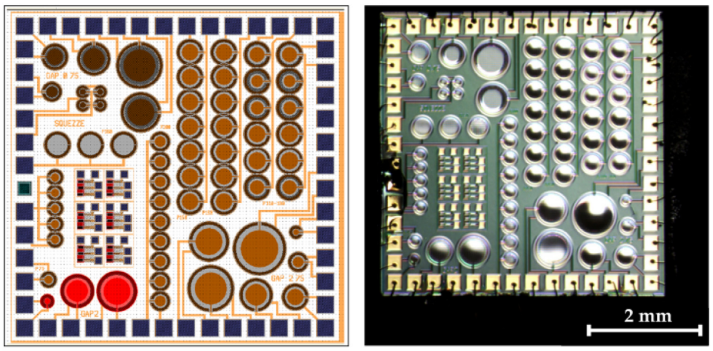

Figure 2.10: (a) Layout (b) fabricated broadband CMUT chip for AE measurements, reproduced from [37].

J. Welsch et al. [38] proposed a polymer-based capacitive micro-machined ultrasound transducer (polyCMUT) for AE sensing in fiber-reinforced polymers. The transducer is claimed to have a low acoustic impedance ($\simeq 3.5\,MRayl$) close to that of the fibre-reinforced polymers, implying a reduced signal loss. The potential for AE detection is verified by standard *pencil lead break (PLB)* tests. CMUTs have advantages of broad bandwidth, high sensitivity and efficiency, good integrated circuit compatibility and geometry flexibility [33]. The downside is that the operation of CMUTs requires constant DC bias voltage, which may pose challenges on long-term durability for AE applications [39].

The above categories of MEMS ultrasonic sensors share a common feature that the transduction components are all coupled with micro-mechanical resonators to improve the signal-to-noise ratio. Although the transduction mechanisms are different, the primary function of all these ultrasonic sensors is to convert the mechanical input signals into readable and processable electrical signals.

Although some progress has been made, there is still a way to go to achieve comparable performance on MEMS AE sensors with conventional piezoelectric sensors. In particular, the sensitivity of mainstream MEMS sensors requires improvements, which is still hardly so high as that of piezoelectric sensors in recent a few years. One of the best examples is provided by [40], where a maximum velocity sensitivity of $148\,V/(m/s)$ ($43.3\,dB$) is obtained. This is already close to the mainstream level at $50 \sim 70\,dB$ of piezoelectric AE sensors. So far, the testing of most proposed MEMS-based AE sensors has been obtained in laboratory environments instead of real commercial application. This has significantly weakened the persuasive power of such novel sensors in terms of robustness compared to conventional piezoelectric sensors. In practical applications, robust and long-life packaging design is required to withstand harsh environments.

3

Photonics

3.1. Silicon Photonics

Over the past a few decades, photonic technologies have been evolving rapidly [41], in which light is employed as the information carrier, showing great potential to complement or replace conventional electronics in many areas. Photonics started with the research on laser in 1960 [42]. Since then, various optical components have been developed for telecoms and sensing needs, including laser diodes, optical fibers, modulators and photodetectors, etc. By integrating the above components together in on-chip circuits, which is referred to as Photonic Integrated Circuits (PIC), a wide range of functions can be achieve including high-precision sensing and computing.

Silicon, as a commonly used material in the electronics industry, also plays an important role in photonics. Such silicon-on-insulator (SOI) platform is often referred to categorised as silicon photonics. Owing to its robustness, accessibility, high refractive index and high transparency, silicon is an ideal and practical optical medium. In addition, silicon photonic systems hold considerable industrial promise as they can be manufactured on the existing omplementary metal oxide semiconductor (CMOS) infrastructure of the semiconductor industry, enabling low cost and reliable mass-fabrication. In recent years, a number of advanced standardized platforms have been established, offering a wide range of high-performance photonic components [43, 44, 45, 46].

In the field of sensing technology, integrated photonic sensors based on interferometers or optical resonators perform a wide variety of functions such as temperature monitoring, ultrasonic detection and biosensing, which give perspectives to a multitude of chemical, biological and architectural applications [42]. Photonic sensors offer a lot of unique advantages over the conventional types. Driven by totally different principles, photonic sensors can reach excellent performance, for example, ultra-high sensitivity and low detection limits. Having electrons replaced by photons as the signal carrier, the photonic systems are resistant against the effect of electromagnetic interference [47]. In addition, photonic sensors allow for smaller device sizes or large-scale integrated arrays due to their small footprints [48].

3.2. Optical Waveguides

The optical waveguides are the most fundamental component of photonic devices. The simplest optical waveguide consists of a slab or rod with a refractive index higher than that of the surroundings, whose working principle can be described in multiple ways. The well-known ray optics provides a simple model to explain the working principal of optical waveguides. From the perspective of geometrical optics, light is partially reflected and partially transmitted as it propagates through the interface of different media, with the reflective ray being symmetric and refractive trajectories following Snell's law,

$$n_1 \sin\theta_1 = n_2 \sin\theta_2 \tag{3.1}$$

where n_1, n_2 are respectively the refractive index of medium 1 and 2, defined by the ratio of light speeds in the medium to that in vacuum. θ_1, θ_2 represent the angles of incidence and refraction. The scenario is shown in Fig. 3.1 (a), assuming $n_1 > n_2$.

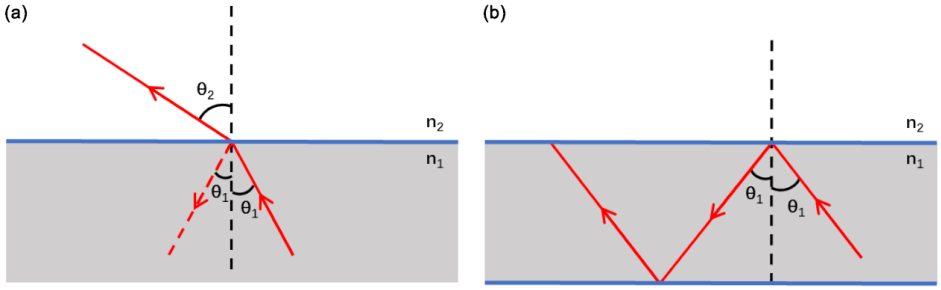

Figure 3.1: Schematic diagram of refraction.

Since the medium 2 has a relatively lower refractive index, the refractive angle θ_2 is larger and will approach $90°$ as the incidence angle θ_1 increases. It is deduced that there is a critical incident angle θ_c such that the refracted rays in medium 2 cease to exist at all greater angles of incidence, as shown in fig. 3.1 (b). The phenomenon that the light propagates completely in medium 1 is referred to as *total internal reflection (TIR)*. The medium with relatively higher refractive index that transmits light "without loss" is called a *waveguide*.

The above model of ray optics provides a preliminary, though inaccurate, explanation for the total reflection phenomenon. Considering the nature of light as electromagnetic waves, a more complete description of light propagation in waveguides can be obtained from Maxwell's electromagnetic theory. For monochromatic light in a passive, isotropic linear dielectric medium, the Maxwell's equations are given by [49]

$$\nabla \times \vec{E} = -j\mu_0\omega\vec{H} \tag{3.2}$$
$$\nabla \times \vec{H} = j\omega\epsilon\vec{E} \tag{3.3}$$
$$\nabla \cdot \epsilon\vec{E} = 0 \tag{3.4}$$
$$\nabla \cdot \vec{H} = 0 \tag{3.5}$$

where μ_0 is the vacuum permeability, ϵ the permittivity, and ω the angular frequency. According to the Helmholtz wave equation

$$(\nabla^2 + n^2k^2)\vec{E} = 0 \tag{3.6}$$
$$(\nabla^2 + n^2k^2)\vec{H} = 0 \tag{3.7}$$

with $k = \omega/c$ the wave number in vacuum [49], and the continuity conditions of the tangential electromagnetic field components at the interface of the waveguide and its surroundings, the TE and TM modes of the propagating light can be obtained, of which the field distribution on the cross section of a silicon-on-insulator slab waveguide is illustrated below,

Fig. 3.2 (a) and (b) provide schematic diagrams of the electric and magnetic fields of three supported guided modes, respectively. As is shown in the picture, the electromagnetic field of light is actually not confined completely to the inside of the waveguide but with some "leakage". The field outside the core of waveguides is referred to as the *evanescent field*, correlating with both the optical coupling and losses.

Waveguides can be broadly categorized into two types [50]. The first is the above mentioned *slab waveguide* or *planar waveguide*, referring to a two-dimensional layer with higher refractive index, in which light is guided in one direction. The other type is called *channel waveguide*, which can be formed by restricting the dimensions in the width direction. Channel waveguides can achieve dual-directional guidance of light and are thus extensively used in photonic devices, such as photo-diodes or optical resonators. There are three main types of channel waveguides, respectively the strip waveguides, rib waveguides and slot waveguides, as shown in Fig. 3.3.

Here, the sensitivity of waveguides describes the interaction of guided light with the surrounding medium, which is related to the strength of evanescent fields. Theoretically, rib waveguides achieve the lowest loss and sensitivity.

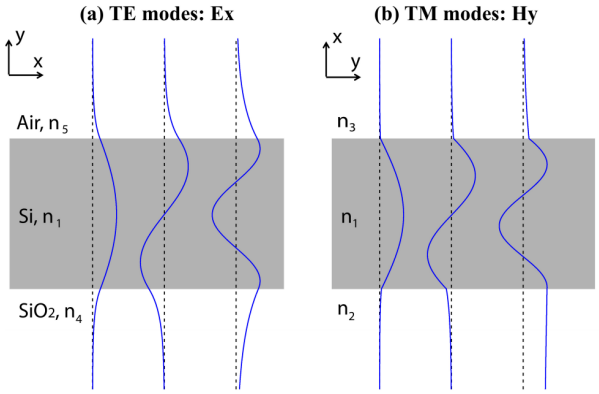

Figure 3.2: TE and TM modes of light propagating orthogonal to the xy plane in a slab waveguide, reproduced from [42]

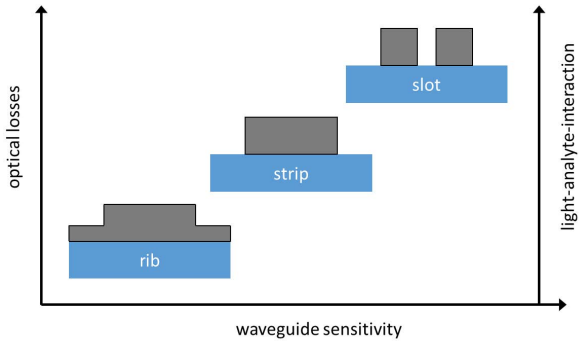

Figure 3.3: Typical rib, strip and slot waveguides, reproduced from [47].

3.3. Micro-Ring Resonator

Micro-ring resonators (MRR) are a typical photonic device based on evanescent-coupling, which is widely used as the functional element of photonic sensors. In general, a ring-shaped waveguide is placed in the physical environment of interest, to which the light is coupled from closely passing waveguides via evanescence field, shown in Fig. 3.4 (a).

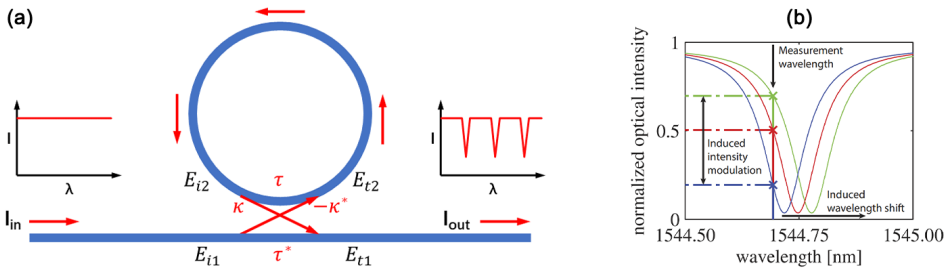

Figure 3.4: Operational principle of micro-ring resonators. (a) Schematic diagram of a micro-ring resonator with one coupler. (b) Transmission curves of a laser with physically induced wavelength shift, reproduced from [42].

If the optical path of the ring is an integer multiple of the light wavelength, the light propagating in the ring resonator will be in phase with that in the coupler after one revolution, which leads to interference. As a result, resonant peaks will appear on the transmission spectrum [47], with the resonance condition

$$m \cdot \lambda_m = n_e(\lambda_m, \chi) \cdot L(\chi) \tag{3.8}$$

where λ_m is the resonance wavelength, m is the resonance number, n_e is the effective refractive index of the ring waveguide, L is the circumference of the ring, and χ represents an influential physical parameter. The changes in the ring circumference or effective refractive index triggered by χ can result

in a shift in the optical resonance, as shown in Fig. 3.4 (b), which can be subsequently read out by interrogation systems.

A concrete description of the coupling process can be provided by means of the so-called *Transmission Matrix*. For a micro-ring resonator system made of single-mode waveguide, the unidirectional coupling with one zero-loss coupler can be expressed as [42]

$$\begin{pmatrix} E_{t1} \\ E_{t2} \end{pmatrix} = \begin{pmatrix} \tau^* & \kappa \\ -\kappa^* & \tau \end{pmatrix} \begin{pmatrix} E_{i1} \\ E_{i2} \end{pmatrix} \tag{3.9}$$

where E_i and E_t refer to the normalized complex mode amplitudes, with subscript i and t indicating "input" and "transmission", subscript 1 and 2 indicating the bus waveguide and the micro-ring resonator, respectively. τ and κ refer to the transmission coefficient and the coupling parameter, satisfying

$$|\kappa|^2 + |\tau|^2 = 1 \tag{3.10}$$

and $*$ denotes their conjugated complex value. Within one round trip in the ring, the wave experiences a phase delay ϕ_r and a loss

$$E_{i2} = \alpha e^{j\phi_r} E_{t2} \tag{3.11}$$

where α is the loss coefficient. With the above definitions and equations, the transmittance in the system can be obtained

$$T \equiv \frac{|E_{t1}|^2}{|E_{i1}|^2} = \frac{\alpha^2 + \tau^2 - 2\alpha\tau cos\theta}{1 + \alpha^2\tau^2 - 2\alpha\tau cos\theta} \tag{3.12}$$

or

$$T = 1 - \frac{(1-\alpha^2)(1-\tau^2)}{(1-\alpha\tau)^2 + 4\alpha\tau \sin^2\frac{\theta}{2}} \tag{3.13}$$

where $\theta = \phi_r + \phi_\tau$ is the phase delay of traveling through the ring and the single coupler. For simplicity, the transmission coefficient τ is assumed real, zero-loss and without phase-related terms. For typical silicon-on-insulator ring resonators, the ϕ_τ is small, thus the overall phase delay can be estimated with

$$\theta \approx \phi_r = \frac{2\pi n_e}{\lambda} 2\pi b \tag{3.14}$$

where n_e refers to the effective refractive index, and b the ring radius.

Eq. 3.12 and Eq. 3.14 actually provide the transmission spectrum of the micro-ring resonator, on which resonance peaks occur at $\theta = 2m\pi$. The resonance peaks can be characterised by a series of metrics:

- *Full Width at Half Maximum (FWHM)*, also known as the $3-dB$ bandwidth, provides an estimation for the width of resonance peaks. With the effective refeactive index n_e weakly dependent on the wavelength λ, we have
$$\Delta\lambda_{FWHM} = \frac{\lambda_m}{\pi n_e L} \cos^{-1}\left[\frac{2\alpha\tau}{1+\alpha^2\tau^2}\right] \tag{3.15}$$
- *Extinction Ratio*, defined by the ratio of the minimum transmission power to the maximum transmission power, which occurs respectively at resonance and zero-interference condition
$$r \equiv \frac{|E_{t1}|^2_{min}}{|E_{t1}|^2_{max}} = \frac{(\alpha-\tau)^2(1+\alpha\tau)^2}{(\alpha+\tau)^2(1-\alpha\tau)^2} \tag{3.16}$$
- *Free Spectral Range (FSR)* refers to the wavelength distance between two adjacent resonance peaks. The FSR of the resonance peak m is given by
$$\Delta\lambda_{FSR} = \frac{\lambda_m^2}{n_e L} \tag{3.17}$$

The optical resonance shift caused by physical parameter χ can be detected in multiple ways. One method is to investigate the transmission spectrum. With a broadband light source or tuneable laser providing the input signal, the transmitted light can be recorded by a spectrum analyzer or photo-diodes. This approach has a relatively larger interrogation range but is quite slow in response, which is fatal for ultrasonic wave detection. An alternative method is based on single-mode lasers, which can largely simplify the post-processing of the signal. By tuning the laser wavelength to the flank of the optical resonance peak around $1550\,nm$ at rest, the deformation-induced resonance shift can be directly translated into a modulation of the transmitted light intensity, as shown in Fig. 3.4 (b). The main challenge of this method lies in the limited range of measurement, as the resonance shifts can only be followed effectively if not greater than the FWHM.

Due to the above properties, micro-ring resonators show potential application for high-performance ultrasonic sensors. For typical photonic ultrasonic wave sensors, the acoustic pressure is normally employed as the influential parameter, resulting in the deformation of ring resonators and thereby changing the resonance wavelengths. Higher sensitivity can be sought by utilizing the resonance of micro-mechanical structures to amplify the deformation of ring resonators at the acoustic frequencies of interest.

3.4. Optical Micro-Machined Ultrasonic Sensors (OMUS)

Optical micro-machined ultrasonic sensors (OMUS), also known as optomechanical ultrasonic sensors or photonic micro-mechanical ultrasonic sensors, are a relatively new concept for next generation of acoustic emission sensors. Similar to other MEMS sensors, the OMUS also typically uses micro-mechanical resonators for signal amplification, but are expected to achieve higher sensitivity with optical signal conversion. With photonic devices such as micro-ring resonators and Mach–Zehnder interferometers, the mechanical signals of AE ultrasonic waves can be converted into optical signals.

In previous works, varieties of photonic sensors have been developed for untrasonic wave detection in biomedical applications and NDE technology. S. M. Leinders et al. [48] reported an optical ultrasound sensor enabled by a micro-machined membrane. In this example, the acoustic pressure acting directly on the membrane is converted to the elongation of a racetrack resonator, as shown in Fig. 3.5. The first prototype is demonstrated to be capable of detecting pressures of $0.4\ Pa$, which matches the performance of state-of-the-art piezoelectric sensors, while reducing the footprint by a factor of 65.

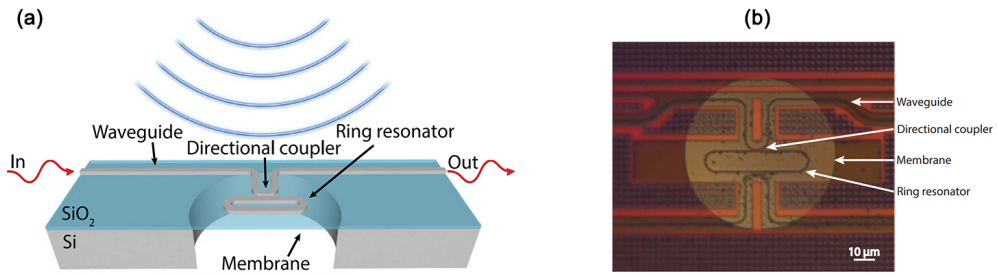

Figure 3.5: A sensitive optical micro-machined ultrasound sensor (OMUS), reproduced from [48]. (a) Schematic diagram. (b) Microscope photograph.

.

In addition to the potential in higher sensitivity and smaller footprint, the OMUS also enable lower cost and higher production efficiency in mass manufacturing, as both the micro-mechanical vibrators and the optical circuits can be fabricated with CMOS-compatible processing, eliminating the need for platform switching or rework. The photonic microchips can also avoid the complex wiring and electromagnetic interference, facilitating arrayed arrangements and large-scale integrated circuit designs that are highly scalable in the future [51].

With the above possibilities, the photonic ultrasonic sensors are highly favourable for AE applications. In addition to higher sensitivity, the conversion of dominant UGW mode among sensors at the same node can be avoided to a large extent by sensor miniaturisation and on-chip integration. However, it should be noted that there are still challenges with current photonic sensors. A common problem is the constant energy consumption of laser sources. Besides, for most existing photonic chip designs, the ultrasonic waves are coupled to the sensor with liquid medium to achieve direct acoustic pressure

detection, which is not applicable for monitoring devices that work outdoors in complex outdoor environments for long periods of time due to the reliability challenges.

There are no known examples of the OMUS being applied to AE technology. In prior works, the photon-based AE sensors are investigated and tested mostly on larger dimensions. Fibre 0ptics sensors (FOS) are one of the conventional optical approaches in AE technology, in which the fibres are roughly on the order of $100\ \mu m$ in total diameter, and the whole sensors in mm [52, 53]. This implies fundamental differences that the fibre-optic sensors have a significantly larger footprint than the OMUS and cannot be processed with the on-chip platform.

4

Design Prerequisites

4.1. Design Specifications

This project is based on SHM NEXT's existing product **UniQ** ®, which is developed for ultrasonic non-destructive detection of architectural structures. The product employs distributed sensors to detect the diffracted ultrasonic guided waves and locate the cracks. In this engineering cooperation project, the lab is dedicated to replacing conventional piezoelectric sensors with silicon photonic chips, with a view to achieving higher sensitivity and exploring the possibility of more functionalities. As a start of the whole R&D cycle, we hope to first design and fabricate a silicon photonic sensor with comparable performance to the current piezoelectric sensor, which is to be refined in the future so as to realize the full potential of our concept.

In this project, the design of opto-mechanical AE sensors based on the resonant configuration is proposed. According to technical communications with the cooperating company, the main parameters and design requirements are first defined. Based on the working conditions of the existing product, the physical characteristics of the AE signals to be detected are determined with a centre frequency of $100\,kHz$ and a bandwidth of at least $40\,kHz$.

As a prototype, the first priority of the opto-mechanical AE sensor is on sensitivity, for which the bandwidth can be sacrificed to some extent as a trade-off. To obtain comparable performance to commercial piezoelectric sensors, the design target is to achieve at least $60\,dB[V/(m/s)]$ velocity sensitivity at $100\,kHz$. Considering the characteristics of resonant AE sensors, the bandwidth is defined in two ways in this project. One is the 6-dB bandwidth around the centre frequency to investigate the frequency range where the sensor provides responses of at least half the resonance. The second is based on a preset threshold of $35\,dB$, and the bandwidth is defined with the frequency range where the sensor response is above this value. Of these, the second definition employs a widely recognized response threshold for commercial AE sensors, while the first reflects the width of the optimal frequency range of sensors within the design scope. Extreme miniaturization and integration will not be pursued in this project, but rather good compatibility with existing platforms and the mounting elements is of more importance.

4.2. Fabrication Methodology

This section involves the technical background on the manufacturing of OMUS sensors. In the first part, the manufacturing process of SOI wafer is presented. This explains the source of initial stress in layers, which is one of the most important external factors considered in this project. In the second part, the main micro-machining techniques are introduced, which determines the implementation of the proposed designs in this project.

4.2.1. Silicon-On-Insulator Wafer

The fabrication of most photonic integrated circuits, consisting of waveguides and various optical devices, are based on silicon-on-insulator (SOI) Technology. The cross section of a typical SOI wafer is shown in Fig. 4.1. The SOI technology differs from conventional bulk silicon platform that the silicon

layer sits on top of an electrical insulator, normally silicon dioxide. The standard SOI wafer is of a three-layer structure, with a $250\,\mu m$ silicon substrate at the bottom, a $2\,\mu m$ SiO_2 layer referred to as the Buried OXide (BOX) layer in the middle, and a silicon waveguide layer of $220\,nm \pm 20\,nm$ thickness on the top.

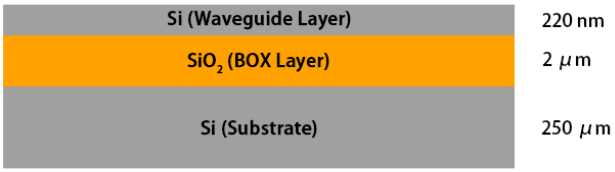

Figure 4.1: Cross-sectional schematic diagram of a silicon-on-insulator wafer.

Various platforms have been developed for SOI wafer production, such as *Separation by IMplantation of Oxygen (SIMOX)*, *Zone-Melting-Recrystallization (ZMR)*, *Wafer Bonding (WB)* and *Smart-Cut* ® techniques [54]. Among them, the Smart-Cut ®, or in the name of *Ion Split* technique, is currently the most widely used method for SOI wafer production. Smart-Cut® is a combination of ion injection and wafer bonding techniques. Initially, a hydrogen-rich layer is formed at a certain depth under the SiO_2 layer of a thermally oxidised mono-silicon wafer by high-dose hydrogen-ion injection. Subsequently, a new silicon wafer is bonded to the oxide surface and heat treated as a whole. During the annealing process, small cracks are generated in the hydrogen-rich layer, along which the bonded wafer is separated, resulting in a thin silicon layer of a thickness equal to the hydrogen-ion injection depth. The obtained SOI wafer is then etched or polished to improve the surface quality and to obtain the required silicon layer thickness.

Since most of the above processes require heat treatment over a wide range of temperature, initial stresses normally exist in the finished wafer. Depending on the actual heating temperature, time and environment, different stress levels may be generated in the SOI wafer. Considering the thermal expansion coefficient of SiO_2 ($5 \times 10^{-7} K^{-1}$) is smaller than that of Si ($2.6 \times 10^{-6} K^{-1}$), SOI wafers typically exhibit compressive stresses in the SiO_2 layer and tensile stresses in the Si layer. Apart from heat treatment, other fabrication steps can also lead to different mechanical properties of the SOI wafer and consequently the final product.

4.2.2. Micro-Machining Technology

In standard CMOS process of silicon photonic platform, the silicon waveguides and other devices are produced on the top silicon waveguide layer. In the present design, another two steps are also considered after the fabrication of photonic circuits. First, the BOX layer and silicon substrate need to be etched from the back to form a single-layer silicon membrane. Second, as an option, a SiO_2 or Si_3N_4 layer can be deposited on top of the silicon waveguide layer to achieve special optical or mechanical properties, such as customized effective refractive index or mechanical stiffness. Both the machining precision of the above steps and the mechanical effects introduced can affect the performance of the sensor, which are therefore briefly discussed in this sub-section.

Deep Reactive Ion Etching

Deep reactive ion etching (DRIE) process is capable of producing steep-side holes with high aspect ratio on SOI wafers, thus achieving the back-side removal of the silicon substrate and the BOX layer in the present project. The silicon substrate and the SiO_2 layer are etched in two steps due to differences in chemistry.

Among all existing high-rate DRIE technologies, the Bosch process is generally considered as the most widely adopted in commercial fabrication. The process involves repetitive switching between two modes, namely the standard plasma etching and the deposition of passivating layer, to achieve accurate and controllable deep etching. Though perfectly vertical etching is possible by tailoring the

balance between etching and deposition processes, the holes created with DRIE process usually exhibits a slight taper [55], which leads to $0.1\ \mu m$-dimensional errors on the pattern at an etching depth of $2\ \mu m$. In this project, a minimum design fineness of $1\ \mu m$ is considered for the determination of the etching radius.

Plasma-Enhanced Chemical Vapor Deposition

Plasma-enhanced chemical vapor deposition (PECVD), also referred to as *plasma-assisted chemical vapor deposition (PACVD)*, is a low-temperature vacuum deposition process with an important role in the semiconductor industry. Compared with conventional chemical vapor deposition (CVD) techniques, PECVD avoids high reaction temperature by introducing part of the reaction energy through plasma, which allows for relatively lower stress on the interface and thus stronger bonding.

In this project, PECVD process is employed to apply cladding on top of the waveguide layer, in which the internal stresses generated during deposition lead to different mechanical behaviors. Different initial stresses can be achieved by controlling the reaction conditions, such as reaction rate and reactant ratios. It has now been reported that the PECVD process is capable of achieving low-stress SiO_2 layer with about $50\ MPa$ tensile stress [56] and Si_3N_4 layer with tensile stresses ranging at least from $40\ MPa$ to $500\ MPa$ [57]. A detailed discussion on the effects of cladding with initial stresses on the behavior of micro-machined membranes is provided in Section. 7.3.

5

Conceptual Design

5.1. Dynamics Response of the System

The present sensor is based on the basic mass-spring-damper system, of which the mechanical model is shown in Fig. 5.1.

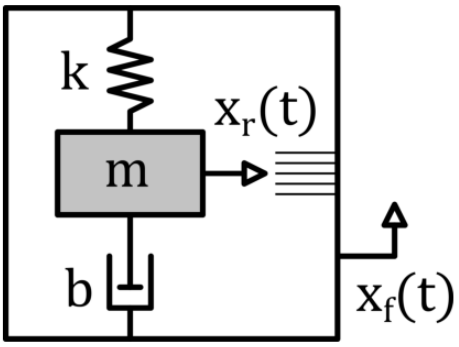

Figure 5.1: Schematic diagram of basic mass-spring system, reproduced from [34].

The governing equation is given by [34]

$$m \cdot \frac{\mathrm{d}^2 x_r(t)}{\mathrm{d}t^2} + b \cdot \frac{\mathrm{d}x_r(t)}{\mathrm{d}t} + k \cdot x_r(t) = -m \cdot \frac{\mathrm{d}^2 x_f(t)}{\mathrm{d}t^2} \tag{5.1}$$

where m represents the mass, k the spring constant, and b the damping. x_f and x_r are the displacement of the housing and the relative displacement of the resonator to the housing, respectively. The dynamics of the system can be characterized by its natural frequency, determined by the mass and spring stiffness,

$$\omega_0 = \sqrt{k/m} \tag{5.2}$$

For general cases with harmonic stimuli and responses, the displacement variable x and its derivatives can be converted into exponential form, i.e.

$$x = A \cdot \mathrm{e}^{i\omega t} \tag{5.3}$$

$$\dot{x} = A\omega i \cdot \mathrm{e}^{i\omega t} = i\omega x \tag{5.4}$$

$$\ddot{x} = -A\omega^2 \cdot \mathrm{e}^{i\omega t} = -\omega^2 x \tag{5.5}$$

The sensitivity of mass-spring transducers can be characterized in multiple ways, depending on the input signals and the way they act on the systems. For microphone-type sensors, acoustic pressure is the direct cause of spring deformation. Thus, the sensitivity can be defined by the compliance of

the system, that is, the displacement of the mass per unit force applied. For the present study, as the AE sensors are normally attached to the surface of architectural structures, the ultrasonic waves directly cause displacement of the housing and consequently drive the vibrations of the internal mass. The sensitivity can therefore be determined by transmissibility, that is, the transfer of motion from the housing to the mass. The sensor sensitivity to acceleration and displacement can be expressed in terms of its complex frequency responses, respectively

$$G_a = \frac{x_r}{\ddot{x}_f} = \frac{-m}{(i\omega)^2 \cdot m + i\omega \cdot b + k} \tag{5.6}$$

$$G_d = \frac{x_r}{x_f} = \frac{-(i\omega)^2 \cdot m}{(i\omega)^2 \cdot m + i\omega \cdot b + k} \tag{5.7}$$

whose plots are given by Fig. 5.2 and Fig. 5.3.

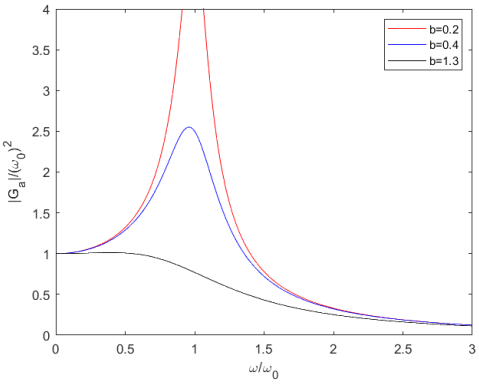

Figure 5.2: Acceleration sensitivity with regard to signal frequency for different dampings.

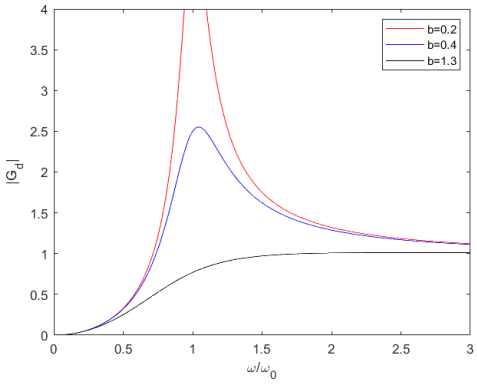

Figure 5.3: Displacement sensitivity with regard to signal frequency for different dampings.

For the cases with excitation frequency $\omega \ll \omega_0$, which is also referred to as the quasi-static range, the sensitivities of the sensor to acceleration and displacement are given by

$$|G_a| \approx \frac{1}{{\omega_0}^2} \tag{5.8}$$

$$|G_d| = \omega^2 \cdot |G_a| \approx 0 \tag{5.9}$$

In quasi-free frequency range, where $\omega \gg \omega_0$, the sensitivities are

$$|G_a| \approx \frac{1}{\omega^2} \approx 0 \tag{5.10}$$

$$|G_d| = \omega^2 \cdot |G_a| \approx 1 \tag{5.11}$$

It is suggested by the above equations that the sensor works as an accelerometer for the cases where the signal frequency much lower than the eigen frequency of the mass-spring system. For significantly high signal frequencies, the sensor works as a vibrometer.

In this project, the opto-mechanical AE sensor is designed as a vibrometer with two main considerations. First, as stated in Section. 2.2, the displacement sensitivity fundamentally determines the ability of AE sensors to detect signals at a given frequency. For AE sensors with given bottom noises from the electrical or optical systems, a higher amplification of the magnitude of displacement provides higher signal-to-noise ratio. Second, AE sensors are usually designed to respond to AE waves with frequencies at or higher than the first resonance, which is achievable with the vibrometer concept, as shown in FIg. 5.3. More details on sensitivity analysis is provided in Chapter. 9.

5.2. Design Concept

Membranes have long been considered as an ideal choice for micro-mechanical resonators of photonic sensors due to their simplicity and ease of fabrication. With a micro-ring resonator attached to the surface, the deformation of the membrane can be translated into an elongation of the micro ring circumference and subsequently into a shift of the optical resonance peak to be detected. In prior works [48], the BOX layer is used to form the membrane. Due to the thermal process during production, initial compressive stresses are usually present in this layer [58]. If the stress exceeds the critical load, the membrane will buckle unpredictably upwards or downwards at rest, which consequently leads to significant shift in the acoustic resonance frequency and great performance instability [59]. The dynamics of the membrane can become unpredictable, as it is usually not possible to determine the direction of buckling in prior.

To solve this problem, a new concept is proposed in the present project. By etching both the silicon substrate and the BOX layer from the back, a membrane can be created with only the silicon waveguide layer, as shown in Fig. 5.4. For simplicity, the bus waveguide in Fig. 5.4 (a) has been omitted.

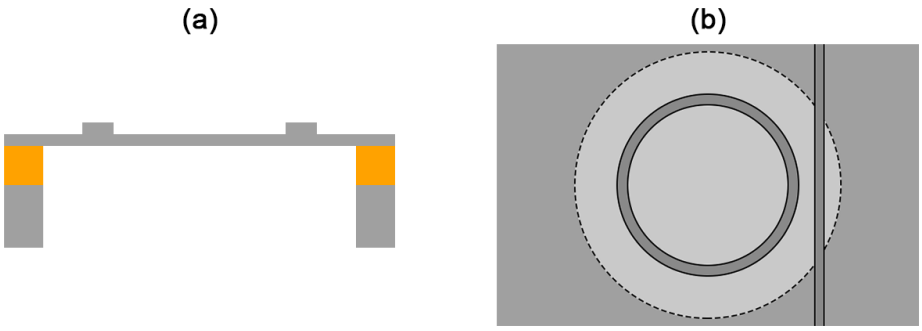

Figure 5.4: Schematic diagram of opto-mechanical AE sensors based on micro-machined membranes, with (a) cross-sectional view, (b) top view.

In this concept, the micro-ring resonator and connections are formed by rib waveguides, fabricated by etching part of the thickness of the silicon layer. The micro-ring resonator is placed in the centre of the axial-symmetric circular membrane to capture the largest possible deformation under most conditions. As mentioned in Section. 4.2, due to the different thermal expansion coefficient between Si and SiO_2, the waveguide layer is expected to have tensile stress in the wafer.

An additional design option is to apply a low-stress SiO_2 or Si_3N_4 cladding on the micro-machined membrane by PECVD process [56] to ensure mechanical stability with small tensile stress and to modulate the eigen frequency, if necessary. A schematic diagram is provided in Fig. 5.5. It should be noted that such coatings may lead to lower sensitivity [56] due to higher material damping, which will be discussed in detail in Chapter. 7.

Figure 5.5: Schematic diagram of opto-mechanical AE sensors based on micro-machined membranes with cladding, with (a) cross-sectional view, (b) top view.

As stated in Section. 4.1, the sensitivity is here taken as the most important performance specification. For general opto-mechanical sensors, the system sensitivity can be considered as the product of the mechanical sensitivity, which is also referred to as *signal amplification*, and the optical sensitivity,

$$\frac{\partial T}{\partial x_f} = \frac{\partial T}{\partial b}\frac{\partial b}{\partial x_f} \tag{5.12}$$

where T refers to the normalized transmittance, x_f the input signal, b the radius of the micro-ring resonator. It also takes the form of

$$\frac{\partial T}{\partial x_f} = \frac{\partial T}{\partial L}\frac{\partial L}{\partial x_f} \tag{5.13}$$

where l refres to the circumference of the micro-ring resonator.

The determination of sensor bandwidth also follows Section. 4.1, with two definitions. It should be noted that the present design focuses on the first-order vibration of micro-machined membranes, so responses at frequencies greater than the centre frequency of $100 kHz$ are not part of the design phase, though included in the bandwidth considerations. Due to the lack of data on actual noise levels, the limit of the second type bandwidth is set to $35\ dB$ according to the specifications of commercial AE sensors, such as R15I-AST Sensor® by Physical Acoustics.

5.3. Design Variables

To clarify the design space, the following variables are declared for the present design, as illustrated in Fig. 5.6. It should be noted that some of the symbol settings in the numerical simulation setups and in the derivation of theoretical models are different from those here.

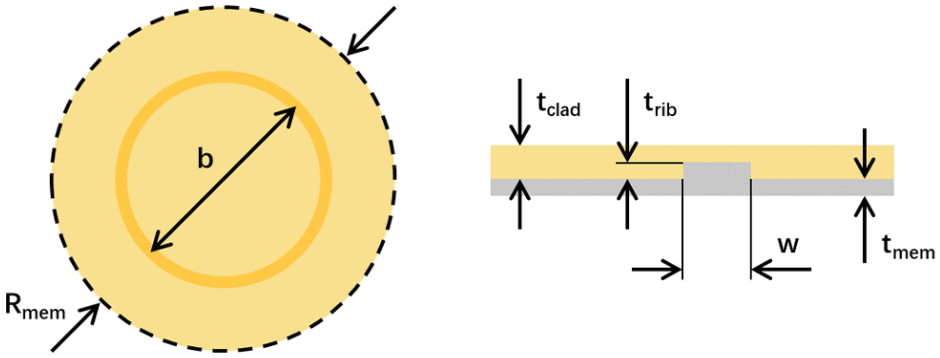

Figure 5.6: Schematic diagram of opto-mechanical AE sensors based on micro-machined membranes with cladding, with (a) cross-sectional view, (b) top view.

Table 5.1: Main design variables in the present project.

Design variables	Remark
R_{mem} or R	Radius of the micro-machined membrane
t_{mem}	Thickness of the membrane/slab thickness of the rib waveguide
t_{rib}	Rib height/Etching depth of the rib waveguide
t_{clad}	Thickness of the deposited SiO_2 or Si_3N_4 cladding
w	Width of the rib waveguide
b	Radius of the micro-ring resonator
Cladding material	Discrete variable, including SiO_2 and Si_3N_4

Of the above design variables, t_{mem} and t_{rib} are not independent, satisfying

$$t_{mem} + t_{rib} = t_{total} \tag{5.14}$$

where t_{total} refers to the total waveguide layer thickness of $220\ nm$, following the structure of typical SOI wafers. Besides, though it is possible to fabricate rib waveguides of different cross-sectional dimensions, the waveguide width is taken $450\ nm$ in the present design unless otherwise specified.

Most of the above variables are theoretically continuous. In order to fully discuss the design possibilities with a complete understanding on the operating principles, such continuous-variable assumption is adopted in Chapter. 7 and 8. The variable R_{mem} and b are usually free to design. To ensure a safe and robust design, it is specified that the etching depth t_{rib} is taken $70 \sim 120\ nm$.

In practice, the available values of design variables depend on the fabrication platform. In this project, the proposed opto-mechanical micro chips are planned to be fabricated with Cornerstone® Foundry, which provides two options for partial silicon etching processes, namely shallow etching of $70\ nm \pm 10\ nm$ and intermediate etching of $120\ nm \pm 10\ nm$. In Chapter. 9, only this two options are compared. According to the present plan, the PECVD process is to be carried out in the laboratory, such that the variable t_{clad} has complete freedom of design.

6

Modelling and Simulation

6.1. Modelling Strategy

In this project, computer modelling and numerical simulations are carried out with the solid mechanics module of COMSOL Multiphysics 6.0. Before the modelling and simulation process, global parameters, such as model dimensions, initial stresses and excitation, need to be first defined in **global definition**. Since the opto-mechanical AE sensor based on circular micro-machined membranes is characterized by three-dimensional axial symmetry, the modelling is performed within **2D axisymmetric** component for simplicity and less computational resources in simulation.

Under the created component, definitions are made on geometry, material, boundary conditions and mesh. First, 2D drawings are made within **Geometry** on the rotational cross section. An example is provided by Fig. 6.1.

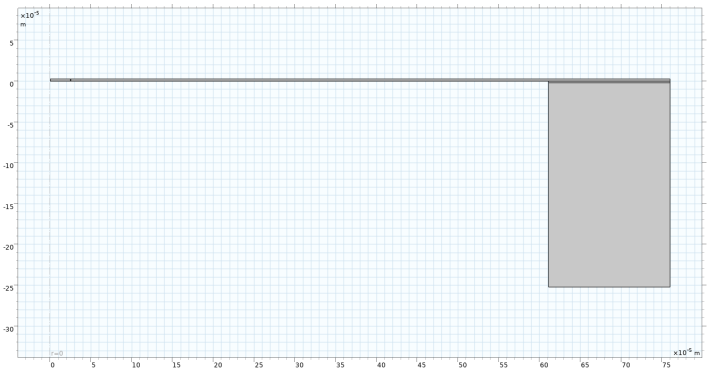

Figure 6.1: 2D drawing for modelling of membrane-based opto-mechanical AE sensors within a 2D axisymmetric component.

The grey dash-dotted line on the left side represents the rotary axis. It should be noted that the rib waveguide on micro-machined membranes is modelled separately in this project, so that the simulation results of variables, such as radial displacements or angular strain, over this area can be conveniently obtained with **Domain Probes**.

In this project, three materials are considered, namely Silicon, SiO_2 and Si_3N_4. All three are added from library, as shown in Fig. 6.2.

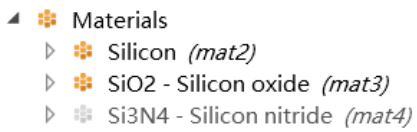

Figure 6.2: Materials involved in the present design.

As considering the configurations of bare membrane or membrane with SiO_2 cladding, one can choose to disable the Si_3N_4 material. The other two materials are always enabled, with Silicon being given to the substrate and the waveguide layer and SiO_2 being given to the BOX layer and cladding (if applicable).

The key aspect of physical scenario construction is the definition of the **solid mechanics module**, as shown in Fig. 6.3. **Linear Elastic Material** is selected for all domains in the model. In order to simulate materials with internal stresses, **Initial Stress and Strain** can be added, where the the definitions are made with matrices, as shown in Fig. 6.4. In the present project, no initial strain is involved. The initial stresses in the waveguide layer and cladding are represented with the radial and angular principal stress components, since the component on vertical direction is released.

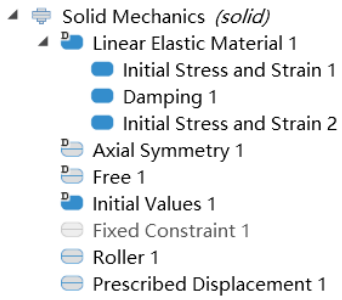

Figure 6.3: Settings in solid mechanics module.

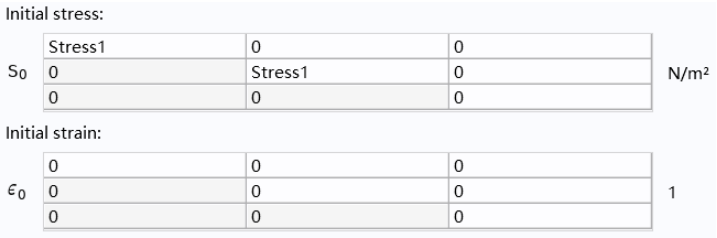

Figure 6.4: Initial stress and strain matrices.

Damping can also be added in **Linear Elastic Material**, which in this case is defined with the so-called isotropic loss factor.

Figure 6.5: Damping definition with the isotropic loss factor.

In addition, boundary conditions and initial conditions need to be defined in this module. In this simulation, a portion of the substrate, BOX layer and bonded waveguide layer are retained outside the micro-machined membrane, of which the outer cylindrical surfaces need to be set as **Roller**. Under this boundary condition, the displacement in the direction perpendicular to the surfaces equals zero, while the movement in the tangential direction is free. For simulations on eigen frequency, **Fixed Constraint** needs to be added on the bottom surface of the model, which needs to be replaced by **Prescribed Displacement** as the excitation for simulations on frequency response. No **Initial Values** are included in this simulation, which is thus set to 0. Other settings such as the **Axial Symmetry** and **Free** are automatically generated.

In the **Mesh** setup, the refinement level needs to be selected depending on the complexity of models and the variation in simulation results. For simplicity, a physics-controlled mesh type with ”extra fine” element size is employed in most cases of this project. An example of mesh distribution in vicinity of the rib waveguide is shown below.

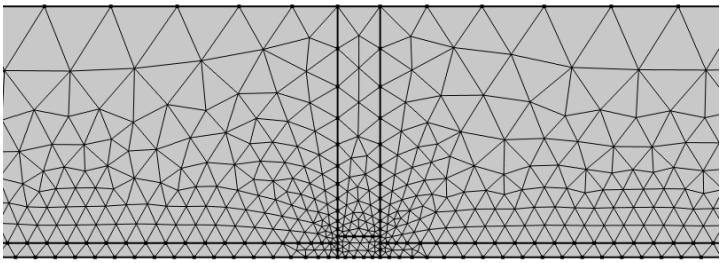

Figure 6.6: Example of mesh distribution in vicinity of the rib waveguide.

6.2. Simulation Settings

This project involves the simulation of two main studies. One is the **Eigenfrequency** in **General Studies**, which is capable of calculating the eigen frequencies of a given model. The other one is the **Frequency Domain** in **General Studies**, mainly used for calculating the frequency response of a given model under given excitation with a given simulation step size.

For **Eigenfrequency** study, special attention should be paid to checking the box **"Include geometric nonlinearity"** when dealing with cases with initial stresses, as shown in Fig. 6.7.

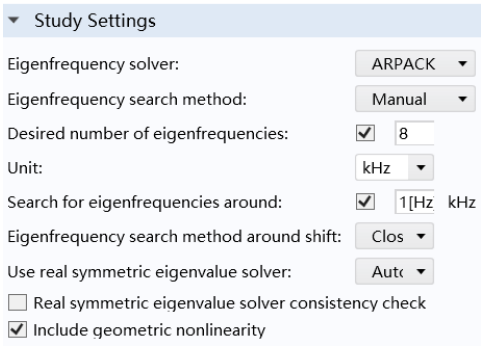

Figure 6.7: Settings of **Eigenfrequency** study on models with .

For **Frequency Domain** study, as mentioned above, an excitation needs to be included. In this project, the displacement excitation of $1\ nm$ is considered. In addition, the frequency range and step size of computation should be determined according to specific questions. As a trade-off, a larger step size leads to a less refined output over the considered range but also allows faster calculation. The specific settings of frequency range and step size for particular questions will be presented later in Chapter. 9.

In post-processing, **Tables**, **1D Plot Group**, **2D Plot Group** and **3D Plot Group** are mainly applied for directly outputting the desired graphs or exporting the data to Matlab for subsequent processing. In order to display changes in variables at a certain point or on a certain line, new **Cut Point 2D** or **Cut Line 2D** datasets are required.

7

Sensor Design: Mechanical Analysis

7.1. Mechanical Resonator Design

In this project, micro-machined membranes are employed as the mechanical resonator for ultrasonic signal amplification. In order to reduce the disturbing factors in design, the simplest circular membranes are considered, for which analytical solutions normally exist. This section will discuss in detail the approaches to the analysis of this micro-mechanical resonator.

7.1.1. Analytical Model

The dynamics of the so-called membrane resonators may be characterized with two analytical models, namely classical membranes and plates, which are applicable to different research questions and physical scenarios.

In terms of the physical models proper, the membrane is a simplified ideal model with no bending stiffness, in which the restoring force comes exclusively from tension, while the plate model does have bending stiffness as the source of the restoring force [60]. The membrane and plate models can be respectively thought as the generalisation of the one-dimensional string and bending bar models to two dimensions.

Classical Membrane Model

The membrane model is formulated as a completely flexible and infinitely thin film with uniform material and constant thickness. It is assumed to be stretched uniformly in all directions by a tension so large that the fluctuation in its value due to small deflections during vibration can be neglected. The XY plane is set coincide with the membrane plane.

The vibration dynamics of the membrane model can be studied in two ways. In an energy point of view, the increased potential energy and kinetic energy of the membrane during vibration can be obtained by

$$\begin{aligned} \Delta V &= S \cdot \Delta A \\ &= \frac{S}{2} \iint \left[\left(\frac{\partial w}{\partial x} \right)^2 + \left(\frac{\partial w}{\partial y} \right)^2 \right] dx\, dy \end{aligned} \tag{7.1}$$

where S refers to the uniform tension per unit length of the boundary, A the surface area of the membrane, and w the deflection at any point of the membrane. The kinetic energy is given by

$$K = \frac{\sigma}{2} \iint \dot{w}^2\, dx\, dy \tag{7.2}$$

where σ is the surface density of the membrane.

Considering the maximum values of both kinetic and increased potential energy occur when the other is 0, the analytical solution of the eigen frequencies can be obtained with the conservation of

energy, which formulates that the two maximums should be equal. With the deflection of the membrane assumed as

$$w = W(x, y) \cos \omega t \tag{7.3}$$

where the *mode function* $W(x, y)$ determines the shape of the normal vibration modes of the membrane, it can be concluded that

$$\omega^2 = \frac{S}{\sigma} \frac{\iint \left[\left(\frac{\partial W}{\partial x} \right)^2 + \left(\frac{\partial W}{\partial y} \right)^2 \right] dx\, dy}{\iint W^2\, dx\, dy} \tag{7.4}$$

The solutions can be subsequently obtained with, for instance, the Rayleigh-Ritz method, by taking the series form of deflection that satisfies the boundary conditions and ensuring that the difference between the maximum kinetic and increased potential energy of the system always remains zero for any possible change in the shape function under different modes. In other words, the difference between the two is insensitive to changes in the coefficients in $W(w, y)$, whose derivative should be zero.

The second approach for obtaining the eigen frequencies is based on the differential equation for the displacement of the membrane, shown as follows.

$$S \nabla^2 w = \sigma \frac{\partial^2 w}{\partial t^2} \tag{7.5}$$

The displacement w can be written as the product of the mode function W and a time-dependent function $T(t)$. For free vibration, T is harmonic and of frequency ω. Eq. 7.5 thus reduces to

$$-S \nabla^2 W = \omega^2 \sigma W \tag{7.6}$$

Knowing that the wave speed c in a membrane with tension S satisfies the following relationship [60],

$$c = \sqrt{\frac{S}{\sigma}} \tag{7.7}$$

Eq. 7.6 can be simplified as

$$\nabla^2 W + \lambda^2 W = 0 \tag{7.8}$$

where $\lambda = \omega / c$.

A circular membrane can be defined by domain $0 \leq r \leq R$, where R stands for the radius of its edge. The polar coordinates (r, θ) is employed here for axial-symmetric circular membranes, in which case the Laplacian operator ∇^2 is given by

$$\nabla^2 = \frac{\partial^2}{\partial r^2} + \frac{1}{r} \frac{\partial}{\partial r} + \frac{1}{r^2} \frac{\partial^2}{\partial \theta^2} \tag{7.9}$$

and the mode function $W(r, \theta)$ is given by

$$W(r, \theta) = R(r) \Theta(\theta) \tag{7.10}$$

Eq. 7.8 is thus reduced and separated into

$$\frac{\mathrm{d}^2 \Theta}{\mathrm{d} \theta^2} + m^2 \Theta = 0 \tag{7.11}$$

$$\frac{\mathrm{d}^2 R}{\mathrm{d} r^2} + \frac{1}{r} \frac{\mathrm{d} R}{\mathrm{d} r} + \left(\lambda^2 - \frac{m^2}{r^2} \right) R = 0 \tag{7.12}$$

for some constant m. For Eq. 7.11, since function $\Theta(\theta)$ is continuous and periodic with period 2π, it follows that

$$\Theta_m(\theta) = C_{1m} cosm\theta + C_{2m} sinm\theta \tag{7.13}$$

with m being an integer. Eq. 7.12 is a *Bessel's Equation* with the solution

$$R_m(r) = C_{3m}J_m(\lambda r) + C_{4m}Y_m(\lambda r) \tag{7.14}$$

where $J_m(\lambda r)$ and $Y_m(\lambda r)$ are m-order *Bessel's functions* of the first and second kind, respectively. It should be noted that the Bessel's function of the second kind, Y_m, is unbounded when $r \to 0$, which lead to non-physical solutions. Therefore, C_{4m} equals zero. Considering the constant C_{3m} can be absorbed later into those from $\Theta(\theta)$ and $T(t)$, Eq. 7.14 can be simplified to

$$R_m(r) = J_m(\lambda r) \tag{7.15}$$

Given that the boundary condition $W(R, \theta) = R(r)\Theta(\theta) = 0$ is true for any arbitrary angular coordinate θ, we have

$$R_m(R) = J_m(\lambda R) = 0 \tag{7.16}$$

by which we know the product $\lambda_{mn}R$ is the n^{th} zero of the m-order Bessel's function J_m. The eigen frequencies can be subsequently obtained with

$$\begin{aligned} \omega_{mn} = \lambda_{mn}c &= \lambda_{mn}\sqrt{\frac{S}{\sigma}} \\ &= \frac{\alpha_{mn}}{R}\sqrt{\frac{S}{\sigma}} \end{aligned} \tag{7.17}$$

where the constant α_{mn} actually stands for the zeros of the m-order Bessel's function J_m, whose values are given by Tab. 7.1

Table 7.1: Values of α_{mn} for different m and n.

	m = 0	m = 1	m = 2	m = 3	m = 4	m = 5
n = 1	2.405	3.832	5.136	6.380	7.588	8.772
n = 2	5.520	7.016	8.417	9.761	11.065	12.339
n = 3	8.654	10.174	11.620	13.015	14.373	15.700
n = 4	11.792	13.324	14.796	16.224	17.616	18.980
n = 5	14.931	16.471	17.960	19.409	20.827	22.218
n = 6	18.071	19.616	21.117	22.583	24.019	25.430

For the fundamental mode, only points on the edge remain stationary during vibration. The so-called *nodal circles* appear at higher vibration modes, where the displacement of points equal zero during vibration. For more general cases, the deflection of the points on the membrane is not only related to the radial coordinate r, but also to the angular coordinate θ. In this case, there are *nodal lines* along the diameters of the circular membrane, with zero displacement at each point. Several modes are shown in Fig. 7.1, where m refers to the number of nodal lines and n the number of nodal circles (with the boundary circle included). For simplicity, the vibrations of each order can be denoted as (m, n).

The mode shape takes the form of

$$W_{mn}(r, \theta) = J_m(\lambda_{mn}r)(A_{mnc}\cos m\theta + A_{mns}\sin m\theta) \tag{7.18}$$

where A_{mnc} and A_{mns} represent modified constants for the cosine and sine terms.

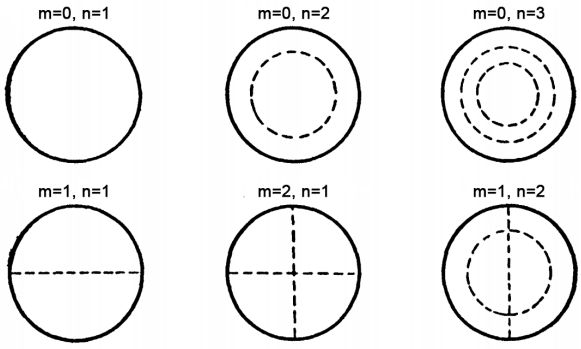

Figure 7.1: Schematic diagram of several vibration modes of a circular membrane, reproduced from [61].

Classical Plate Model

As mentioned earlier, the plate model can be considered as an extension of the bar model in two dimensions. This analogy, however, is not quite rigorous. When in bending deformation, the width of the bar model is so small that the lateral compression and expansion on both side of the neutral plane can be disregarded, whereas the effect is not negligible in a plate model of a finite width. A natural idea is that a plate of finite width can be regarded as the integral of parallel bar elements of infinitesimal width along the lateral direction. In this case, for two adjacent bar elements with equal bending deformations, lateral compression or expansion on the top and bottom sides of their neutral planes will cause a squeeze or void on their common surface, resulting in internal lateral stresses. In addition, since the area elements of a plate can be considered as belonging to two orthogonal bar elements, the planar bending of one bar can be considered as a rotation of the area elements around the normal to the bending plane. If the plate is not deformed evenly along its width, this rotation can be different in the adjacent bar, leading to twist of the orthogonal bar element. To address these inconveniences, the elementary plate theory is based on the following assumptions:

1. The deflection of a plate is small in comparison with the thickness.
2. There is no force resultant on the cross-sectional area of a plate element, so the middle plane of the plate does not undergo deformation and can be regarded as neutral.
3. The normal stresses in the orthogonal direction to the plate surface can be ignored, which means the thickness of the plate remains constant and all points on a line perpendicular to the middle plane have the same displacement.
4. Any straight line perpendicular to the middle plane before deformation remains straight and perpendicular to the neutral plane during deformation.

The differential equation for free vibration of plates can be written as follows

$$D\nabla^4 w + \sigma \frac{\partial^2 w}{\partial t^2} = 0 \tag{7.19}$$

where D denotes the *flexural rigidity* of the plate, in the form

$$D = \frac{Eh^3}{12(1-\nu^2)} \tag{7.20}$$

where E referes to the *Young's modulus*, h the thickness of the plate, and ν the *Poissons ratio*. The symbol $\nabla^4 = \nabla^2\nabla^2$ is known as the *biharmonic operator*. With the deflection written as $w = WT$, Eq. 7.19 reduces to

$$D\nabla^4 W - \omega^2 \sigma W = 0 \tag{7.21}$$

where ω stands for the eigen frequency, and the boundary conditions for a clamped edge are

$$W = 0 \tag{7.22}$$

$$\frac{\partial W}{\partial n} = 0 \tag{7.23}$$

where n denotes the coordinates in the normal direction of the boundary.

For a circular plate, Eq. 7.21 can modified into operator form under polar coordinates,

$$(\nabla^2 + \lambda^2)W_1(r,\theta) = 0 \tag{7.24}$$

$$\left[\nabla^2 + (i\lambda)^2\right] W_2(r,\theta) = 0 \tag{7.25}$$

where

$$\lambda^4 = \frac{\omega^2\sigma}{D} \tag{7.26}$$

and the boundary conditions are

$$W(R,\theta) = 0 \tag{7.27}$$

$$\left.\frac{\partial W(r,\theta)}{\partial r}\right|_{r=R} = 0 \tag{7.28}$$

Eq. 7.24 and Eq. 7.25 are in the form of Bessel's Equation. Considering the boundary conditions and physicality of the equations [60], the eigen frequencies can be obtained in the form of

$$\begin{aligned}\omega_{mn} &= \lambda_{mn}^2\sqrt{\frac{D}{\sigma}} \\ &= \frac{k_{mn}}{R^2}\sqrt{\frac{D}{\sigma}}\end{aligned} \tag{7.29}$$

where the constant k_{mn} for a given number of nodal lines m and a given number of nodal circles n is shown below.

Table 7.2: Values of k_{mn} for different m and n.

	m = 0	m = 1	m = 2	m = 3
n = 0	10.22	21.26	34.88	51.04
n = 1	39.77	60.82	84.58	111.01
n = 2	89.10	120.08	153.81	190.30
n = 3	158.18	199.06	242.71	289.17
n = 4	247.01	297.77	351.38	407.72
n = 5	355.57	416.20	479.65	545.97

The mode shape is in the form

$$W_{mn}(r,\theta) = (I_m(\lambda_{mn}R)J_m(\lambda_{mn}r) - J_m(\lambda_{mn}R)I_m(\lambda_{mn}r))(A_{mnc}\cos m\theta + A_{mns}\sin m\theta) \tag{7.30}$$

where A_{mnc} and A_{mns} represent modified constants for the cosine and sine terms.

7.1.2. Vibration of Micro-Machined Membranes

The above two classical models provide efficient tools for analytical calculations of plate- or membrane-like structures. In many cases, the calculation results from these models correspond well to the actual situation. However, for the vibration of micro-machined membranes, it is possible that the effects brought up by flexural rigidity and internal stress are present simultaneously.

In terms of geometrical features and boundary conditions, the micro-machined membranes should be categorized and calculated as clamped plates. However, as stated in Section 4.2 of Chapter 4, initial stresses can be generated inside the waveguide and BOX layers of the heat-treated SOI wafers.

This effect has also been observed in prior tests and is thought to have significant influence on the mechanical characteristics of photonic ultrasonic sensors [59, 58]. The presence of initial stresses makes the membrane resonators less of standard plates but more akin to hybrid membrane-plate structures. For designers, the dimensional parameters of the mechanical resonator is usually obtained with analytical calculation based on the required centre frequencies before modelling and simulation. It is therefore important to understand the effect of internal stress in the present physical scenarios. The actual value of internal stress varies depending on the specific materials and fabrication processes. A rough estimation of the internal stress in chemically deposited SiO_2 membranes is around $50\ MPa$.

To investigate the effect of the internal stress on the eigen frequencies of the micro-machined membrane, a standard circular membrane is modelled and simulated with different levels of internal stress. The *Eigenfrequency* module of COMSOL is applied to study the eigen frequencies of both cases, where the simulation setup is described in detail in Chapter. 6. In order to exclude the interference of other factors, the model here does not contain any waveguide, and the thickness of the membrane is simply taken as $100\ nm$. The involved geometrical parameters are shown in Tab. 7.3.

Table 7.3: Geometrical parameters of the micro-machined membrane in eigenfrequency simulations.

Parameter	Value	Remark
R_{tot}	$180\ \mu m$	radius of the whole modelling region
R_{mem}	$80\ \mu m$	radius of the micro-machined membrane
t_{mem}	$100\ nm$	thichness of the micro-machined membrane
t_{BOX}	$2\ \mu m$	thichness of the BOX layer
t_{sub}	$250\ \mu m$	thichness of the silicon substrate

The eigen frequencies without initial stress are first studied by comparing the results obtained by numerical simulations and analytical calculations, as shown below. For simplicity, only axial symmetric modes are taken into consideration.

Table 7.4: Eigen frequencies of a circular membrane without initial stress.

Order	Eigenfrequencies from COMSOL simulation / kHz	Eigenfrequencies from analytical calculation / kHz	Error / %
1	65.20	65.29	0.14
2	253.83	254.08	0.10
3	568.68	569.24	0.10
4	1009.54	1010.58	0.10
5	1576.38	1578.09	0.11
6	2269.19	2271.66	0.11

The analytical calculations are in excellent agreement with the simulation results, with an error of around 0.11%. It can be thus concluded that the micro-machined membranes with no initial stress can be modelled as classical plates.

The eigen frequencies of a geometrically identical micro-machined membrane with $50\ MPa$ initial stress is shown in Tab. 7.5

Table 7.5: Eigen frequencies of a circular membrane with $50\ MPa$ initial stress.

Order	Eigenfrequencies from COMSOL simulation / kHz	Eigenfrequencies from analytical calculation / kHz	Error / %
1	717.34	701.04	-2.27
2	1656.35	1609.05	-2.86
3	2623.90	2522.59	-3.86
4	3628.24	3437.30	-5.26
5	4680.28	4352.30	-7.01
6	5790.45	5267.60	-9.03

As is predicted, the micro-machined membrane with $50\ MPa$ initial stress does not behave like a pure membrane. The analytical model has an average shift of -5.05% for the first 6 modes from simulation results. The error increases for higher modes, for which the reason is inferred that the flexural rigidity plays more important role in higher modes due to the complex shape with smaller curvature radius. It is further deduced that a micro-machined membrane behaves more like a plate with lower initial stresses and more like a membrane with higher initial stresses. The eigen frequencies of a micro-machined membranes with different initial stress levels are shown in Fig. 7.2

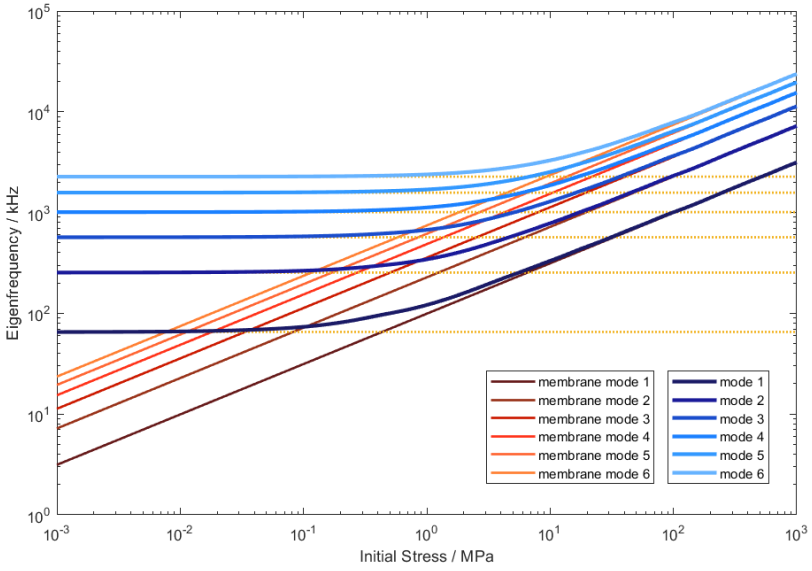

Figure 7.2: Eigen frequencies of a micro-machined circular membrane with different initial stresses. Blue curves are fittings of the simulation results. Red curves and yellow dashed lines represent the analytical membrane and plate models, respectively.

The eigen frequencies of the micro-machined membrane at different initial stress levels are consistent with the inference. Considering that the generalized stiffness of the membrane is provided by the flexural rigidity and the tensile stress together, more accurate predictions can be make by treating the stretched micro-machined membrane as an equivalent mass-spring system with two parallel springs, shown in Fig. 7.3

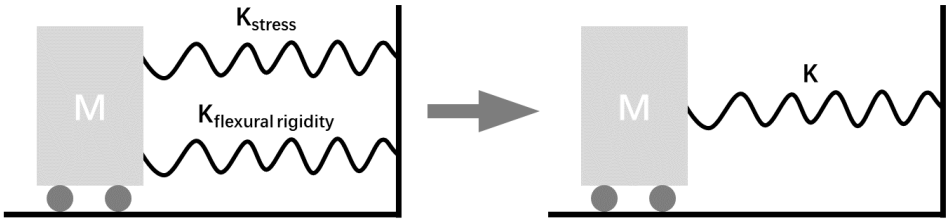

Figure 7.3: Schematic diagram of the equivalent mass-spring system of micro-machined membranes.

The generalized stiffness can be estimated with

$$K = K_{flexural \ \ rigidity} + K_{stress} \tag{7.31}$$

According to Eq. 5.2, the eigen frequency of micro-machined membranes can be estimated with

$$\begin{aligned} \omega_{mn} &= \sqrt{\omega^2_{flexural \ \ rigidity} + \omega^2_{stress}} \\ &= \frac{1}{R^2}\sqrt{\frac{k^2_{mn}D + \alpha^2_{m(n+1)}R^2S}{\sigma}} \end{aligned} \tag{7.32}$$

where m and $n = 0, 1, 2, \ldots$.

Based on the above theory, estimations can be make on the eigen frequencies of micro-machined membranes with different initial stresses. As shown in Fig. 7.4, the analytical model is in good agreement with the simulation results within tolerance. Thus, Eq. 7.32 allows fast design of micro-machined membranes with given eigen frequencies.

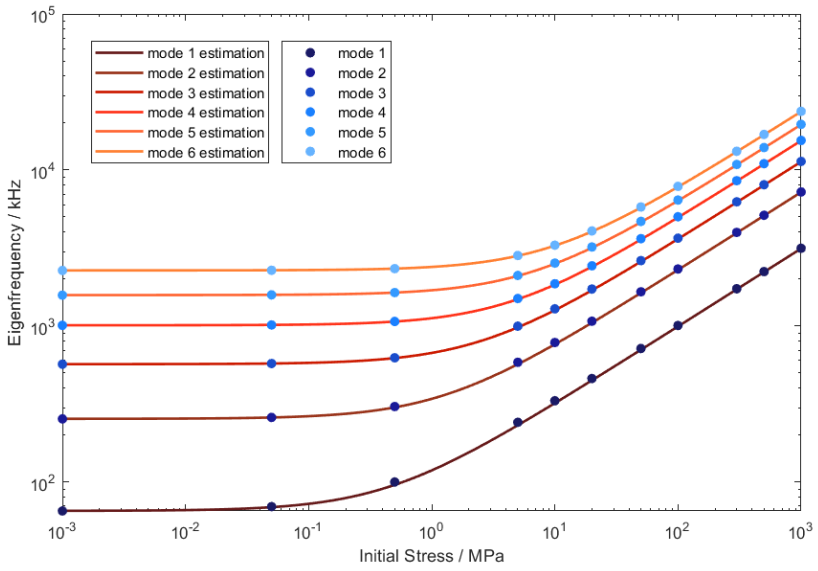

Figure 7.4: Estimation for eigen frequencies of a micro-machined circular membrane with initial stresses. Blue scatters and red curves represent the simulation results and the analytical estimations, respectively.

With the support of the above theory, the contribution of flexural rigidity and internal stresses to the overall stiffness can be roughly estimated in terms of the square of their respective angular eigen frequencies, as shown in Fig. 7.5. For the fundamental mode of the given micro-machined membrane, the overall stiffness provided by internal stresses exceeds that provided by flexural rigidity at levels above $0.4\ MPa$. With the internal stress of $50\ MPa$, the latter is less than 1% of the former.

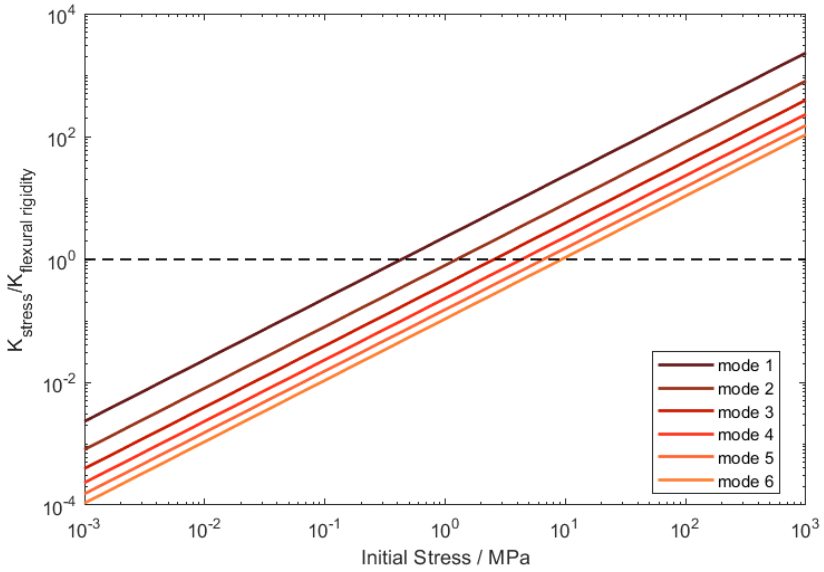

Figure 7.5: Stiffness ratio of flexural rigidity to internal stresses.

It should be noted that higher modes of substrate deformation appear at higher stress levels in simulation. These modes are usually close in frequency to the adjacent membrane-vibration mode, with a same number of nodal circle. These modes should be excluded when considering membrane deformation.

According to the classical membrane and plate models discussed in Sub-Section. , nodal circles appear in high-order modes of micro-machined membranes. In this case, if the micro-ring radius happens to be close to that of a certain nodal circle, only a small deformation can be produced at resonance. In the present design, in order to ensure the design freedom of micro-ring resonators, the first vibration mode with monotonic deflection is mainly considered. The normalized mode shapes of the micro-machined membrane and analytical models are shown in Fig. 7.6.

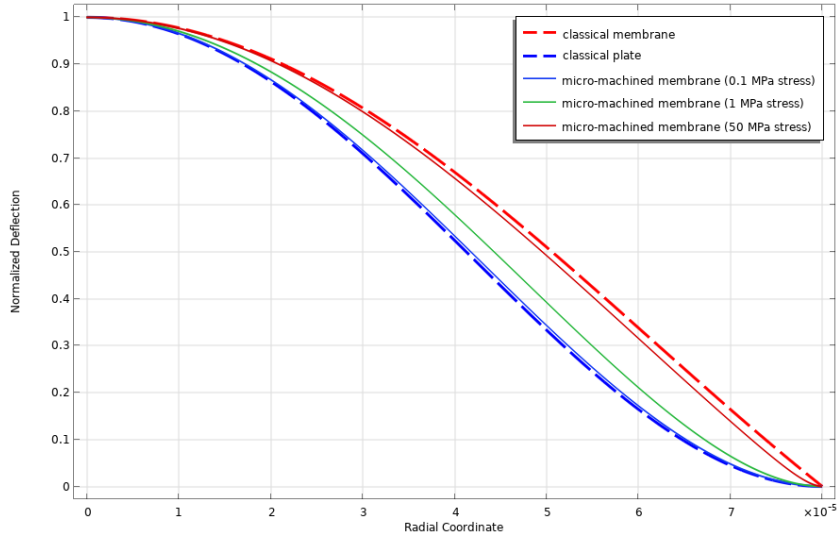

Figure 7.6: Normalized mode shapes of the micro-machined membrane (neutral plane), classical membrane and classical plate.

The mode shape of micro-machined membranes is kind of a mixture of two analytical models, which matches the classical plate model at lower stresses and the classical membrane model at higher stresses. The mode shape of micro-machined membranes with $50\,MPa$ initial stress resembles that of

the classical membrane model to a very large extent, which roughly takes the form of Bessel's function according to Eq. 7.18. Thus, the ratio of the nodal circle radius to the membrane radius of each order can be calculated approximately with the values of α_{mn} in Tab. 7.1. For example, for the vibration mode $(0, 2)$, the radius of the nodal circle is $2.405/5.520 = 0.436$ of membrane radius.

For the present design, micro-machined membranes are designed with a first-order eigen frequency of $100\,kHz$ according to the specifications in Section. 4.1, which shows up to 6 orders of eigen frequencies within the frequency range of common AE signals ($20 \sim 1000\,kHz$, Section. 2.1). Thus, approximation can be made that the deformation of micro-ring resonators with radii smaller than 13% of the membrane radius (i.e. the smallest nodal circle radius at the 6-order resonance) is hardly affected by nodal circles and is thus still safely predictable.

7.1.3. Mechanical Effect of Waveguides

In the above analyses, the mechanical effects of waveguides on the micro-machined membrane have been neglected for simplicity. However, since the micro-machined membrane is formed with the $220nm$ silicon layer and of a comparable scale with the rib waveguide, such effects may be observable.

A comparison between the eigen frequencies of a micro-machined membrane with a built-on silicon micro-ring resonator and an identical bare membrane is shown as follows, where the geometric parameters of the membranes stay the same as above.

Table 7.6: Eigen frequencies of a circular membrane with and without a built-on MRR, with $50\,MPa$ initial stress.

Order	Eigenfrequencies without MRR / kHz	Eigenfrequencies with MRR / kHz	Difference / %
1	717.34	713.98	−0.47
2	1656.35	1649.30	−0.43
3	2623.90	2629.24	0.20
4	3628.24	3651.17	0.63
5	4680.28	4693.90	0.29
6	5790.45	5765.34	−0.43

* Data from simulations by COMSOL Multiphisics 6.0.
** As an example, the MRR has a radius of $15\,\mu m$, made of a silicon rib waveguide of $120\,nm$ in height and $450\,nm$ in width.

The eigen frequencies of the micro-machined membrane do not change much (about 0.41% absolute difference) with a built-on micro-ring resonator of given dimensions. For simplicity, Eq. 7.32 will remain adopted for estimating the eigen frequencies in design. However, it is worth noticing that the effect of waveguides on vibration of micro-machined membranes may be observed in other aspects. Increasing the amount of waveguides or their relative dimensions to the membrane, which is possible in practice, can lead to more significant mechanical effects.

7.2. Deformation of Micro-Ring Resonators

The ultimate goal of mechanical resonator design is to achieve high signal amplification with the largest possible elongation of micro-ring resonators. The mechanical sensitivity of the system can be considered as the linear response of micro-ring radius change with regard to the input displacement

$$\frac{\partial b}{\partial x_f} = \frac{\partial b}{\partial w_0}\frac{\partial w_0}{\partial x_f} \tag{7.33}$$

where x_f is the housing displacement as the input signal, as stated in Section. 5.1. w_0 is the vibration amplitude, defined by the displacement on the membrane centroid. For a given micro-machined membrane, the former partial derivative on the right-hand side of Eq. 7.33 depends on the radius of the micro-ring resonator. The latter partial derivative depends on the design of micro-machined membrane, which reflects the magnification of the ultrasonic wave signal.

In practice, the mechanical sensitivity, defined by change in micro-ring radius or circumference, can be directly obtained from numerical simulation without calculating the above two derivatives. Nevertheless, an in-depth understanding of the mechanisms of micro-ring resonator deformation is essential for rational design. In this section, the analytical model for the deformation of micro-ring resonators is investigated, corresponding to the first factor in Eq. 7.33. The latter one actually defines the bandwidth of the system, which is therefore often analysed separately.

In the case of a large difference between the scale of the micro-machined membrane and the micro-ring resonator, as seen in previous works on thick BOX-layer membranes, the waveguide dimensions are often neglected. That is, the micro-ring resonator is reduced to a geometrical circle on the surface of the membrane, whose circumference change can be calculated with the radial displacement multiplied by 2π. As illustrated in Fig. 7.7, the radial displacement is given by

$$u_r = -\frac{t_{tm}}{2}\frac{\partial w}{\partial r} \tag{7.34}$$

where t_{tm} refers to the thickness of the thick membrane, w the neutral plane deflection and r the radial coordinate.

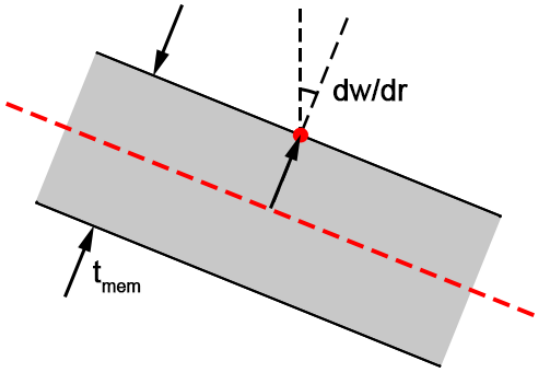

Figure 7.7: Cross-sectional diagram of a deformed thick membrane.

Based on the eigen frequency analysis in COMSOL Multiphysics 6.0, the line graphs of radial displacement on the surface of the micro-machined membrane is obtained by calculating Eq. 7.34, as shown in Fig. 7.8. The deflection of the two analytical models is calculated with the first mode shapes, given by Eq. 7.18 and 7.30. Considering that the classical membrane model does not involve thickness, the membrane deflection is employed here as the neutral plane deflection.

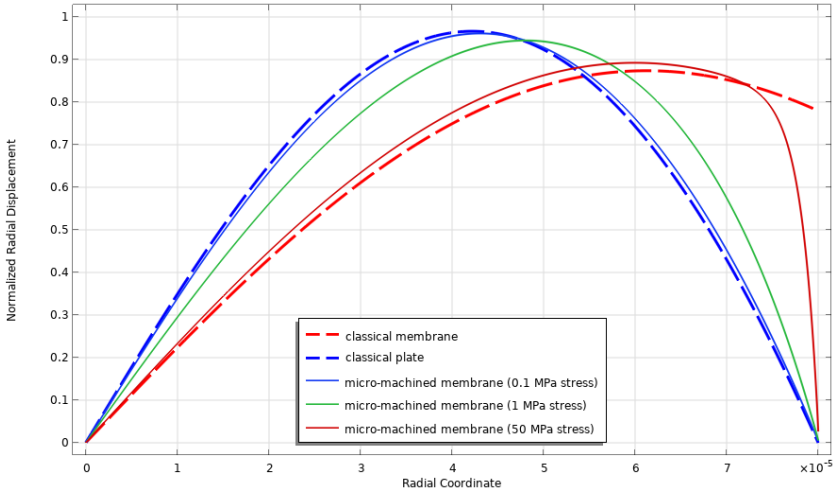

Figure 7.8: Normalized radial displacement on the surface of the micro-machined membrane, classical membrane and classical plate, obtained by COMSOL Multiphysics 6.0.

As the initial stress increases, the maximum radial displacement on the surface appears further to the edge. For the classical plate model with no initial stress, the maximum appears approximately in the middle of the membrane radius ($\approx 0.528\ R$). For the classical membrane model, the maximum appears at about $3/4$ membrane radius ($\approx 0.766\ R$) away from the centre. Therefore, the micro-ring radius should be set at $50 \sim 75\%$ membrane radius for larger elongation.

For the present design, the micro-machined membrane is of a comparable scale in thickness with the micro-ring rib waveguide. In this case, Eq. 7.34 is no longer available since the micro-ring resonator can no longer be treated as a geometrical circle. Considering that the electromagnetic field of laser is distributed in full thickness of rib waveguides, the circumference change of micro-ring resonators should be calculated with the average value of radial displacement on the whole cross section. The distribution of radial displacement on the cross section of micro-ring waveguide is shown in Fig. 7.9.

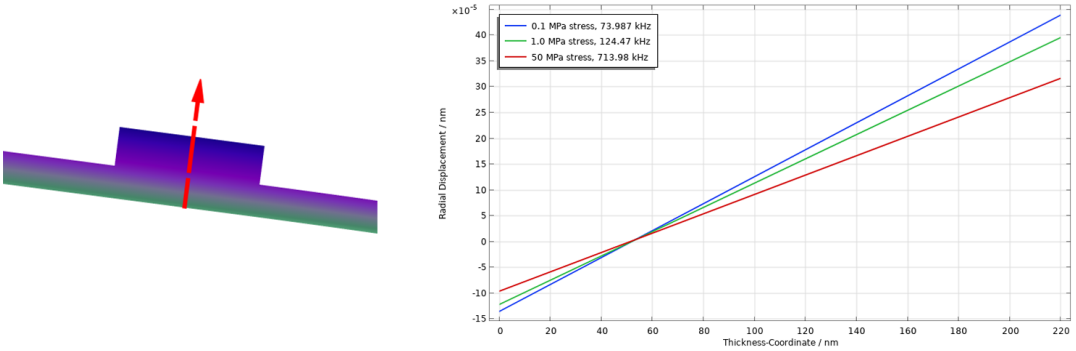

Figure 7.9: Radial displacement along the middle cut line of a micro-ring rib waveguide, obtained from eigenfrequency analysis by COMSOL Multiphysics 6.0.

At the given stress levels, the neutral plane does not experience significant shift on the whole membrane, and the radial displacement on the waveguide cross section is approximately linear with respect to the thickness-coordinate. Given that the membrane thickness is constant, The overall radial displacement on the waveguide cross section can be fairly well estimated with only the protruding part with a good accuracy, as illustrated in Fig. 7.10.

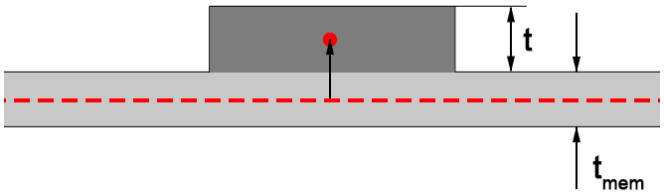

Figure 7.10: Cross-sectional diagram of a bare micro-machined membrane around the built-on rib waveguide.

Thus, one can replace the thick membrane thickness t_{tm} in Eq. 7.34 with the total thickness of rib waveguide, multiplied by the ratio of rib height to the total thickness, ending up with

$$u_r = -\frac{t}{2}\frac{\partial w}{\partial r} \tag{7.35}$$

where t refers to the rib height. Eq. 7.35 resembles well direct simulation, as shown in the table below. The simulation results are obtained from the probe output over the rib waveguide area, while the analytical calculations are carried out with Eq. 7.35, where the neutral plane deflection in $\partial w/\partial r$ is taken from the eigen frequency analysis by COMSOL Multiphysics 6.0.

Table 7.7: Normalized radial displacement of a rib MRR on micro-machined membranes with different initial stress.

Initial stress / MPa	Normalized radial displacement from COMSOL simulation	Normalized radial displacement from analytical calculation	Difference / %
0.1	0.491	0.505	2.85
1.0	0.442	0.455	2.94
50	0.356	0.363	1.97

* As an example, the MRR has a radius of $15\ \mu m$, made of a silicon rib waveguide of $120\ nm$ in height and $450\ nm$ in width.

In numerical simulation, the circumference change of micro-ring resonators can also be obtained with the integral of angular strain, which gives fairly similar results within tolerance.

7.3. Micro-machined Membranes with Cladding

In order to achieve certain mechanical or optical effects, it is sometimes necessary to add cladding on micro-machined membranes, thus introducing a new design variable, the cladding thickness t_{clad}. As introduced in Section. 4.2, one of the most popular methods for cladding fabrication is PECVD process, with a variety of materials available. In this section, the mechanical behaviour of micro-machined membranes with cladding is discussed, in which context the waveguide deformation is analyzed. Unless otherwise stated, the internal stress of the original micro-machined membrane is taken $50\ MPa$ in the following calculations.

7.3.1. Vibration of Cladded Micro-Machined Membranes

Micro-machined membranes with cladding can be decomposed into two layers, the original membrane and the cladding, with respective materials and initial stresses. Following a similar approach to that in Section. 7.1.2, both of the layers can be considered as equivalent mass-spring systems, whose eigen frequencies can be calculated with Eq. 7.32

$$\omega_m = \frac{1}{R^2}\sqrt{\frac{k^2 D_m + \alpha^2 R^2 S_m}{\sigma_m}} \tag{7.36}$$

$$\omega_c = \frac{1}{R^2}\sqrt{\frac{k^2 D_c + \alpha^2 R^2 S_c}{\sigma_c}} \tag{7.37}$$

where the subscript m denotes the original membrane, and c denotes the cladding. For simplicity, the original subscripts representing different modes are omitted.

A natural idea is that, since the two layers are bound at the interface, the cladded micro-machined membrane can be imagined as the two masses being connected. In this case, the springs are in parallel, as shown in Fig. 7.11.

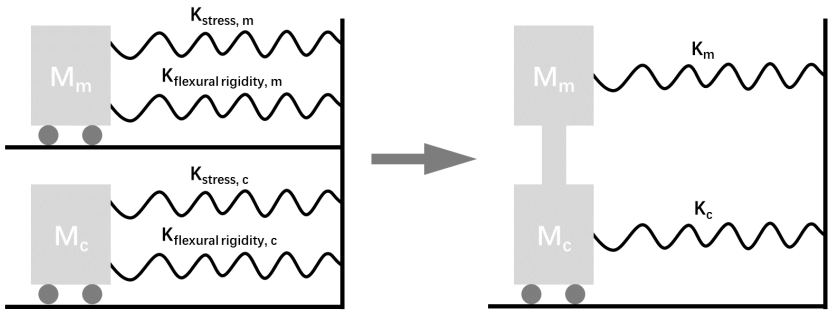

Figure 7.11: Schematic diagram of the equivalent mass-spring system of micro-machined membranes with cladding.

The generalized mass and stiffness of the cladded micro-machined membrane can be obtained with

$$M = M_m + M_c \tag{7.38}$$
$$K = K_m + K_c \tag{7.39}$$

where $K_m = M_m\omega_m^2$, $K_c = M_c\omega_c^2$. The eigen frequencies

$$\Omega = \sqrt{\frac{K}{M}} \tag{7.40}$$

The effects of waveguides are neglected. Based on Eq. 7.40, the estimated eigen frequencies of the micro-machined membrane with cladding of different initial stresses is shown in Fig. 7.12

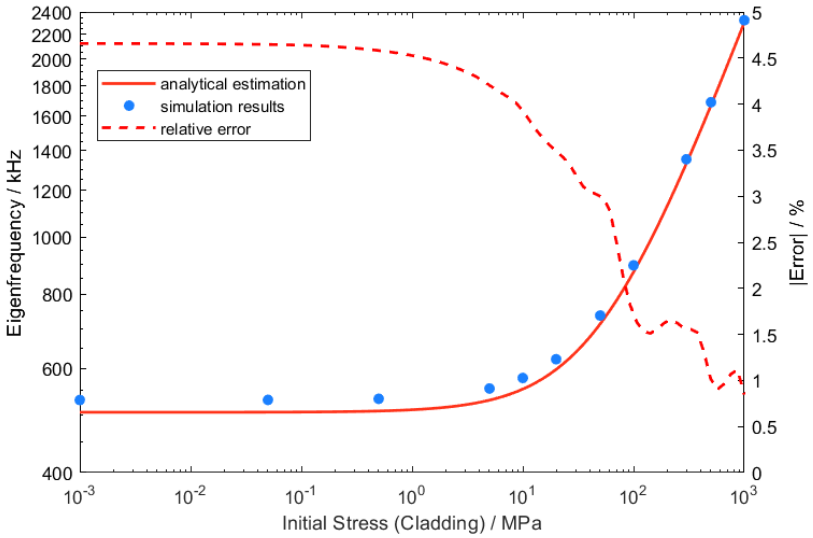

Figure 7.12: Estimation for first-order eigen frequencies of a micro-machined circular membrane with a $100\,nm$ SiO_2 cladding under different initial stresses.

It emerges that the above analytical model is in good agreement with the simulation results for higher initial stress levels in the cladding, but encounters some difficulties at lower stresses, where the error increases from about -0.85% to -4.66%. This is attributed to the fact that micro-machined membranes with cladding are anisotropic in thickness and thus suffer from non-uniform shear deformation, which is neglected in classical plate model. Therefore, errors are introduced in the above method where the generalized plate stiffness of the two layers are calculated separately and added up.

To reduce the error, classical laminated plate theory [62] is employed, where multi-layer plates are constructed of isotropic thin plates bonded without sliding. The element of such laminated plates is shown in Fig. 7.13

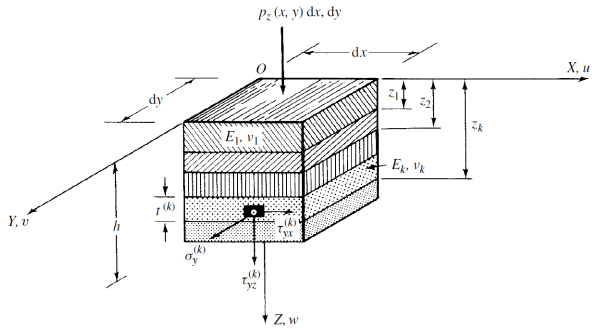

Figure 7.13: Multi-layer plate element, reproduced from [62].

The *transformed flexural rigidity* is given by

$$D^* = \frac{AC - B^2}{A} \tag{7.41}$$

where

$$A = \sum_k \frac{E_k}{1-\nu_k^2}(z_k - z_{k-1}) \tag{7.42}$$

$$B = \sum_k \frac{E_k}{1-\nu_k^2}\frac{z_k^2 - z_{k-1}^2}{2} \tag{7.43}$$

$$C = \sum_k \frac{E_k}{1-\nu_k^2}\frac{z_k^3 - z_{k-1}^3}{3} \tag{7.44}$$

And the overall surface density is given by

$$\sigma^* = \sum_k \rho_k h_k \tag{7.45}$$

In the above equations, $k = 0, 1, 2, \ldots$ indicates the number of layers, and z_k refers to the z-coordinate of the boundaries between layer k and $k+1$. Substituting D^* and σ^* into Eq. 7.29, the corrected eigen frequencies of multi-layer plates can be obtained. Since the flexural rigidity of two layers are calculated jointly, the equivalent mass-spring system consists of three parallel springs representing the stiffnesses from the overall flexural rigidity and the initial stresses in two layers, respectively.

$$K = K_{stress,\ m} + K_{stress,\ c} + K_{flexural\ \ rigidity} \tag{7.46}$$

The corrected estimation is shown in Fig. 7.14. For comparison, the first-order eigen frequency of the original bare membrane with $50\ MPa$ initial stress is also plotted with a black dashed line.

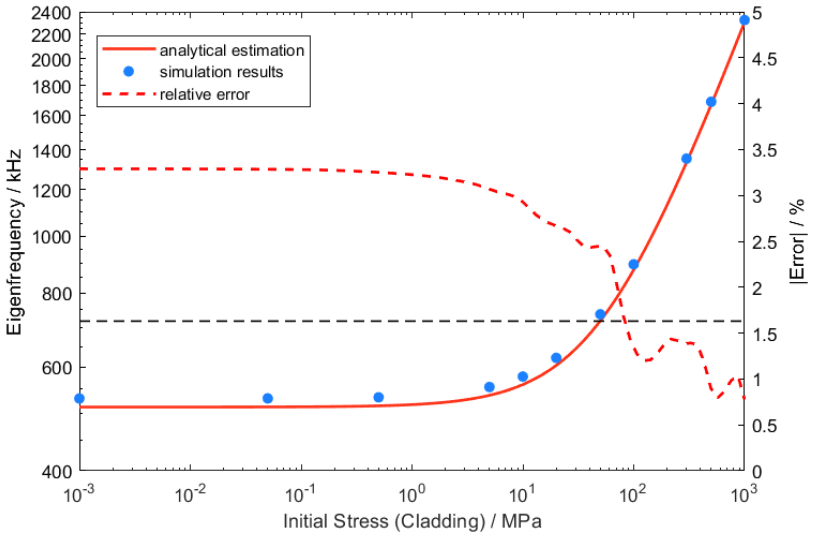

Figure 7.14: Corrected estimation for first-order eigen frequencies of a micro-machined circular membrane with a $100\ nm$ SiO_2 cladding under different initial stresses.

The corrected estimation proved to have a reduced error, ranging from -0.78% to -3.29%. The above theory provides an approach for fast design of micro-machined membranes with cladding. Comparing the dashed reference line with the estimation curve, it can also be concluded that the deposition of a lower-stressed cladding on a micro-machined membrane with a certain initial stress can reduce the eigen frequency of the system.

Following the above theory, the behavior of multi-layer micro-machined membranes is analogous to that of the original homogeneous membranes, especially in cases where the mechanical properties of the layers do not differ too much. In the subsequent discussions, the conclusions on the mode shape in Section. 7.1.2 will be adopted consistently.

7.3.2. Deformation of Micro-Ring Resonators with Cladding

Owing to elevated neutral planes, the deposition of cladding above micro-machined membranes with rib waveguides normally reduces the net circumference change of micro-ring resonators, thus decreasing the mechanical sensitivity. A solution is to increase the cladding thickness t_{clad} so that the neutral plane can be higher than the middle plane of the rib waveguide.

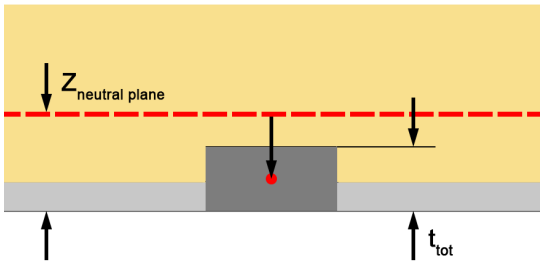

Figure 7.15: Cross-sectional diagram of a cladded micro-machined membrane around the built-on rib waveguide.

For quantitative design, it is necessary to locate the neutral plane of multi-layer micro-machined membranes. For classical laminated plates, the position of neutral planes can be calculated with [63]

$$Z_{neutral\ \ plane} = \frac{\frac{1}{2}\sum_k E_k(z_k^2 - z_{k-1}^2)}{\sum_k E_k t_k} \tag{7.47}$$

following the coordinate system in Fig. 7.13.

For practical multi-layer micro-machined membranes, the presence of internal stress also contributes to the neutral plane position. Nevertheless, a comparison with simulation results shows that Eq. 7.47 can still provide satisfactory estimation within the considered stress range, shown in Fig. 7.16.

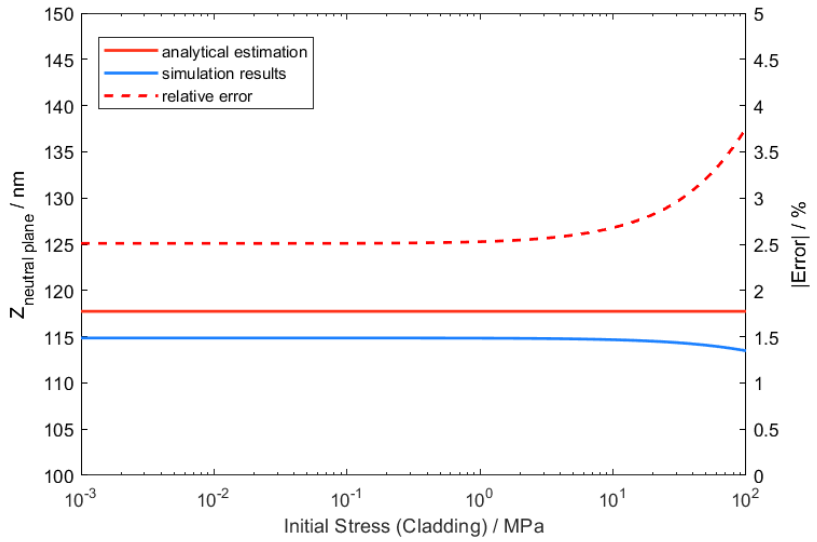

Figure 7.16: Comparison in $Z_{neutral\ \ plane}$ of a micro-machined circular membrane with a $200\ nm\ SiO_2$ cladding under different initial stresses, calculated from classical laminated plate theory and numerical simulation.

Care needs to be taken, as the neutral plane position is not constant along the radial direction, the above estimation may present larger errors for micro-machined membranes with larger radii.

As illustrated in Fig. 7.15, the radial displacement of the waveguide can be estimated with

$$u_r = \left(Z_{neutral\ \ plane} - \frac{t_{tot}}{2} \right) \frac{\partial w}{\partial r} \tag{7.48}$$

where t_{tot} refers to the total thickness of the rib waveguide. In the present work, t_{tot} is a constant value of $220\ nm$.

8

Sensor Design: Photonic Design

8.1. Photonic System Setup

Since silicon is a “passive” material with indirect band gap at the common telecommunication wavelength around $1550\ nm$, it is unable to electronically detect or generate light [42]. A natural idea is to connect the passive photonic chip to external laser sources and interrogation devices with optical fiber. This is now one of the commonly used packaging and integration techniques for photonic chips because of its technical maturity and low design effort. An example of a packaged photonic chip in prior work is provided in Fig. 8.1

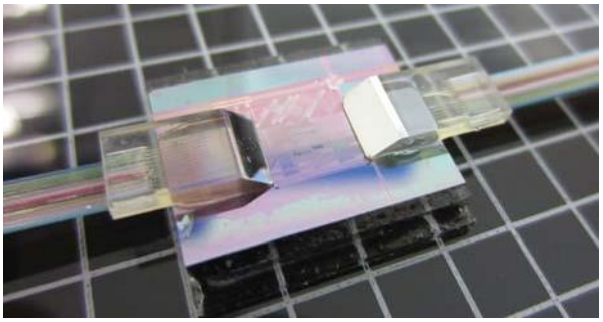

Figure 8.1: Fiber-coupled photonic sensor chip, reproduced from [59].

A schematic diagram is provided in Fig. 8.2, where the thick arrows represent fibre-optic transmission while the thin ones represent on-chip transmission through the silicon waveguides. The laser is coupled from the input fibre to the photonic chip and back into the output fibre via grating couplers, and finally detected by an external photo-detector. As trade-offs, this approach is reported to have a relatively high fiber-to-waveguide peak insertion loss of $4.5\ dB$ [64], and can result in a bulky system due to its incompleteness of integration.

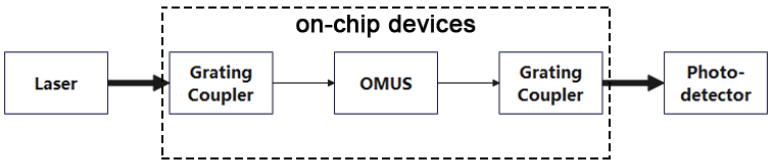

Figure 8.2: Schematic diagram of fibre-coupled photonic setups.

For lower transmission loss and higher robustness, a more integrated and fully packaged photonic system can be achieved by introducing on-chip active devices, such as laser sources and detectors. Both passive and active photonic chips need to be subsequently connected to external drive and control electronics. In terms of performance, the second flavor is a better example of miniaturization and reliability, but can also lead to higher individual costs and longer design cycles, which is only practical and beneficial in massive industrial production. As the first step of small-scale laboratory research and development, we will firstly focus on the passive chip configuration in this project, which is expected to fully reflect the working principles while reducing the difficulty of implementation.

8.2. Photonic Resonator Design

For photonic ultrasonic wave sensors based on micro-ring resonators, the detected resonance shift is brought by mainly two factors: the circumference change of the ring, and the effective refractive index shift of the waveguides due to the Poisson effect and the photo-elastic effect. The change in effective refractive index is neglected in the present work, though it may reduce the sensitivity by a factor of $1/3$ [65]. The linear response of transmittance to micro-ring radius change is thus considered

$$\frac{\partial T}{\partial b} = \frac{\partial T}{\partial \theta}\frac{\partial \theta}{\partial b} \tag{8.1}$$

For a micro-ring resonator with one symmetric directional coupler, the resonance condition is given by Eq. 3.8, and the transmission spectrum is given by Eq. 3.12 and Eq. 3.14. Thus the two factors on the right-hand side of Eq. 8.1 are respectively

$$\frac{\partial T}{\partial \theta} = \frac{2\alpha\tau(1-\alpha^2)(1-\tau^2)\sin\theta}{(1+\alpha^2\tau^2-2\alpha\tau\cos\theta)^2} \tag{8.2}$$

and

$$\frac{\partial \theta}{\partial b} = \frac{4\pi^2}{\lambda} n_e \tag{8.3}$$

To complete the analyses, the refractive effective index ne, the loss coefficient α and the transmission coefficient τ remain to be determined, which are related to the design of the micro-ring resonator and coupler. In addition, it should be noted that the design variable b is also included in θ, and the laser wavelength still remains to be discussed. In this section, the criteria for calculating or selecting the above parameters will be determined in turn, based on which the design principles of ring resonators and the optical coupling is presented.

8.2.1. Effective Refractive Index Analysis

For channel waveguides, the effective refractive index depends mainly on the material and the shape of waveguide cross-section. In the present design, the micro-ring resonators are formed by rib waveguides, whose diagrams are given by Fig. 8.3.

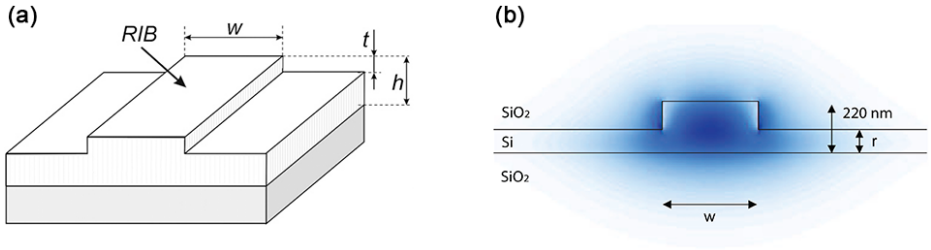

Figure 8.3: Schematic diagrams of rib waveguides. (a) Structure of rib waveguides, adapted from [66]. (b) Cross-sectional sketch of a rib waveguide with profile of the fundamental mode, adapter from [42]

In general, rib waveguides can be described with geometrical parameters, namely layer thickness h, rib width w and rib height t or corresponding slab thickness r, and optical parameters, refractive indices of the cladding n_c, waveguide n_{wg} and BOX layer n_{BOX}. The effective index method [67, 66] is applied to calculate the effective refractive index n_e of waveguides, of which the procedure is as follows:

1. Decompose the rib waveguide into two orthogonal slab waveguides;
2. Calculate the effective refractive index of the asymmetric horizontal slab waveguide n_{ei}, using [67]

$$k_0 n_{wg} d \cos\theta_i - m\pi = \tan^{-1}\left[\frac{\sqrt{\sin^2\theta_i - (n_{BOX}/n_{wg})^2}}{\cos\theta_i}\right] + \tan^{-1}\left[\frac{\sqrt{\sin^2\theta_i - (n_c/n_{wg})^2}}{\cos\theta_i}\right] \tag{8.4}$$

where $k_0 = 2\pi/\lambda$ is the free space wave number, $d = h$ or r is the corresponding thickness, $m = 0, 1, 2, \ldots$ is the mode number. θ_i is the propagation angle, with $i = 1, 2, \ldots$ indicating different areas. The effective refractive index

$$n_{ei} = n_{wg} \sin\theta_i \tag{8.5}$$

By convention, $i = 1$ refers to the core and other numbers represent the sides.

3. Calculate the effective refractive index of the symmetric vertical slab waveguide n_e, with n_{e1} taken as the refractive index of the core, using [67]

$$k_0 n_{e1} w \cos\theta_{wg} = 2\tan^{-1}\left[\frac{\sqrt{\left(\frac{n_{e1}}{n_{e2}}\right)^2 \sin^2\theta_{wg} - 1}}{\left(\frac{n_{e1}}{n_{e2}}\right)\cos\theta_{wg}}\right] \tag{8.6}$$

where n_{e2} refers to the effective refractive index of the surrounding. For typical strip waveguides, $n_{e2} = n_c$. And the overall effective refractive index

$$n_e = n_{e1} \sin\theta_{wg} \tag{8.7}$$

For rib waveguides, the second step should be taken twice for the "rib" ($i = 1$) and the "slab" ($i = 2$) on both sides. In the third step, the refractive index of the "slab" area should be adopted as the surrounding refractive index on both sides of the decomposed vertical slab.

Specifically, for bare rib waveguides with no BOX substrate in vacuum or gas surroundings, $n_c = 1$, n_{wg} equals the refractive index of Silicon, and n_{BOX} should be replaced by n_c. For rib waveguides with cladding under the same condition, n_c should be taken as the refractive indices of the considered cladding materials, shown in Tab. 8.1, and $n_{BOX} = 1$.

Table 8.1: Refractive indices of involved materials at $1550\ nm$ wavelength.

Material	Refractive index (reference value)	Refractive index (approximate value)
Air [68]	1.0003	1.00
Silicon, Si [69, 70]	3.4777	3.48
	3.4757	
Silicon dioxide, SiO_2 [71, 72]	1.4657	1.45
	1.4431	
Silicon nitride, Si_3N_4 [73]	1.9963	2.00

In practice, the calculation of effective refractive index can be more complicated as the waveguides can possibly support more than one mode of light, each with their own effective refractive indices. In the

present design, the effective refractive indices are calculated with the mode solver for $2D$ multi-layer waveguides provided by M. Hammer [74]. It is just as important to clarify that the above method as well as all related numerical solvers are only capable of providing reference values as an approximation. In many cases, the calculation results deviate from the experimental measurements, which is manifested in both the computational values and the supported modes.

Based on the above considerations, only the dominant $TE_{0,0}$ mode is taken into account in design, while the other modes are treated as exclusion conditions if their field strengths are comparable to that of the $TE_{0,0}$ modes. The calculation results of bare and buried rib waveguides of $450\ nm$ width and $220\ nm$ total thickness in air surroundings are shown in Fig. 8.4, where the cladding thickness is taken $200\ nm$ and the 'etching depth' is the rib height put another way.

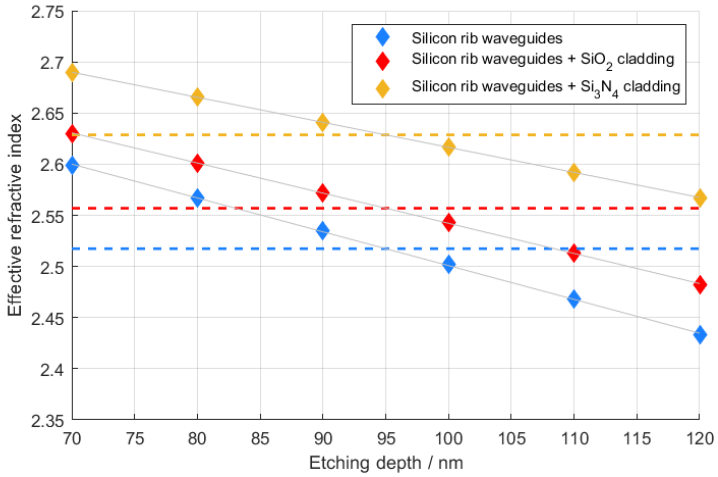

Figure 8.4: $TE_{0,0}$ effective refractive index of bare and buried rib waveguides of different etching depth, calculated with the mode solver for $2D$ multi-layer waveguides [74]. The dashed lines refer to the average value within the range.

It emerges that the effective refractive index is approximately linearly correlated with the etching depth, with the average values of respectively 2.52, 2.56 and 2.63 for the three waveguides over the considered range. In general, for a given total thickness h, greater slab thickness r leads to higher effective refractive index, and thus higher optical sensitivity. However, this is accompanied by possibly higher optical losses, which will be discussed in the next sub-section.

The effective refractive indices of rib waveguides with SiO_2 and Si_3N_4 claddings versus etching depth and cladding thickness are shown in Fig. 8.5. Within the considered range of parameters, the effect of cladding thickness is much weaker than that of etching depth. This is attributed to the fact that the cladding of considered thickness can almost completely accommodates the electromagnetic field of light in the rib waveguide. Therefore, in the determination of the cladding thickness t_{clad}, the main consideration will be given to its mechanical effects.

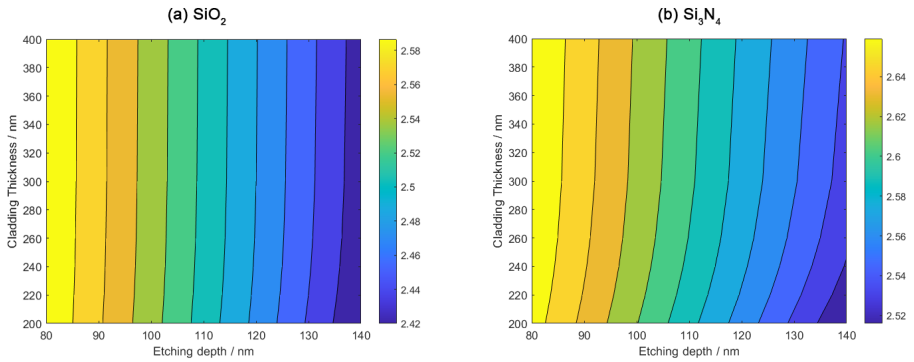

Figure 8.5: Effective refractive index of buried rib waveguides of different etching depth with SiO_2 and Si_3N_4 claddings of different thickness, calculated with the mode solver for $2D$ multi-layer waveguides [74].

8.2.2. Waveguide Loss Analysis

Typical SOI waveguides exhibits three main sources of losses: propagation loss, bending loss and slab leakage loss. Propagation losses exist in all types of waveguides and are inevitable, mainly caused by material defects or processing effects, such as sidewall roughness and width variation of waveguides [42]. Bending losses only exist in curved waveguides, in which radiation happens due to the failure of photons to maintain the phase velocity beyond a certain radius. Slab leakage losses are a special type of losses in rib waveguides, caused by coupling to the slab. For rib waveguides in micro-ring resonators, all three sources exist.

A rigorous study of all loss mechanisms is, unfortunately, beyond the scope of this work. In fact, due to limited knowledge of the materials, structural properties and processing of waveguides, analytical calculation of optical losses is often impractical. However, it is still possible to make a reasonable estimation for the potential loss levels in this design based on previous work.

For the first type of losses mentioned, the propagation loss, current processing technology has allowed a level of $2 \sim 3\ dB/cm$ [75]. For simplicity, the median of $2.5\ dB/cm$ is taken for estimation in this project. Both other losses depend on the actual design of micro-ring resonators. For bending losses in channel waveguides, it has been reported with semi-empirical relations [76]

$$\alpha_{bend} \sim 0.72\frac{4\pi}{\lambda}(n_c - n_s)10^{-\frac{1}{7.6}\frac{2\pi}{\lambda}bn_s\frac{\sqrt[3]{n_c^2-n_s^2}}{n_c^2}} \tag{8.8}$$

where n_c and n_s refer to the refractive index of the waveguide and the surroundings, respectively. λ refers to the laser wavelength. It emerges that the bending losses increase rapidly as the radius decreases. In waveguides with high refractive index contrast, related electromagnetic fields are strongly confined and therefore produce lower bending losses.

It is generally accepted that for rib waveguides with constant total thickness, greater slab thickness leads to greater leakage loss. And vigorous bending can also exacerbate light leakage to the slab. However, A. Brimont et al. [77] have demonstrated in their previous work that for rib waveguides, the bending-induced total losses reach a local minimum in a certain range of small bending radius, as shown in Fig. 8.6. The deviation at a bending radius of $20\ \mu m$ is explained as a result of inaccuracies in spectral normalization. The optimal loss region is produced by the opposite evolution of bending losses and slab leakage losses over a certain range of bending radii.

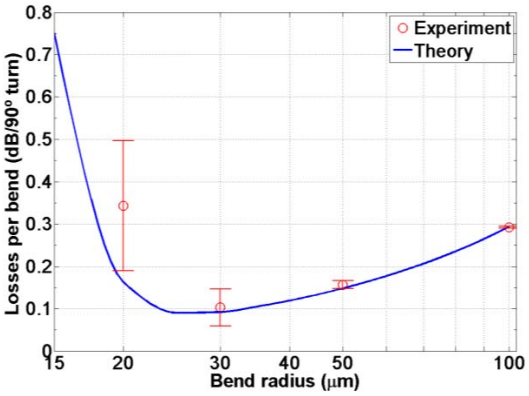

Figure 8.6: Bending-induced losses per $90°$ bend versus the bending radius at $1550\ nm$ wavelength, reproduced from [77].

The bending-induced losses of the rib waveguides in the present design can be estimated according to the numerical simulation by A. Brimont et al. [77], as shown in Fig. 8.7. In the range of parameters considered, the minimum bending-induced losses is below the level of $0.09\ dB/90°\ turn$, and the corresponding optimum bending radius occurs below $40\ \mu m$. Considering that the sensitivity of losses to the bending radius is lower after the point of minima, a slightly larger micro-ring radius is preferred in practical design. A more in-depth discussion is provided in next chapter.

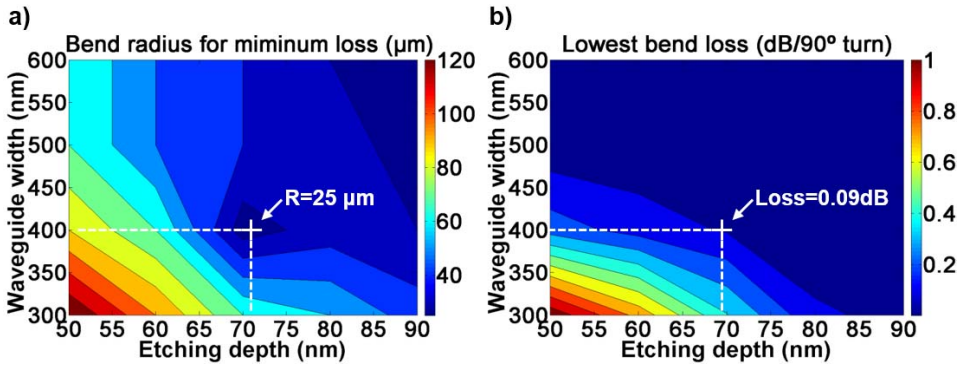

Figure 8.7: Evolution of (a) the bending radius for minimum loss and (b) lowest bending loss versus waveguide width and etching depth, reproduced from [77].

8.2.3. Operation of Micro-Ring Resonators

The operation of micro-ring resonators comes down to two main aspects, the micro-ring design and the optical coupling process. By describing the waveguide properties in terms of its effective refractive index n_e, the deign of a standard passive micro-ring resonator reduces to its geometry, determined by micro-ring radius b. In the configuration considered in the present design, the opitcal coupling process is realized with directional couplers, described with the transmission coefficient τ. In addition, the selection of the laser wavelength λ is related to the shape and position of the resonance peaks, which should therefore also be taken into account.

With the goal of achieving maximum optical sensitivity, the optimal values of all the above parameters can be determined according to the following method. Considering that both the loss coefficient α and transmission coefficient τ within the design space should be close to 1, the FWHM $\Delta\lambda_{FWHM}$ of resonance peaks, given by Eq. 3.15, is small. Thus, the phase delay θ can be described as small shift $\Delta\theta$ from the resonance, that is

$$\theta = 2m\pi + \Delta\theta \tag{8.9}$$

With small-angle approximation $\sin^2\theta/2 = \sin^2\Delta\theta/2 \approx \Delta\theta^2/4$ in Eq. 3.13, the transmittance can be estimated with

$$T \approx 1 - (1 - T_{min})\frac{\frac{1}{4}\Gamma^2}{\frac{1}{4}\Gamma^2 + \Delta\theta^2} \tag{8.10}$$

where T_{min} refers to the transmittance at resonance, and Γ the FWHM, given by

$$T_{min} = \frac{(\alpha - \tau)^2}{(1 - \alpha\tau)^2} \tag{8.11}$$

$$\Gamma = \frac{2(1 - \alpha\tau)}{\sqrt{\alpha\tau}} \tag{8.12}$$

To obtain the maximum sensitivity $\partial T/\partial\theta$, the laser should be tuned to achieve its inflection point, that is

$$\Delta\theta = \frac{\sqrt{3}\Gamma}{6} \tag{8.13}$$

with the maximum sensitivity

$$\left(\frac{\partial T}{\partial\theta}\right)_{max} = \left(\frac{\partial T}{\partial\Delta\theta}\right)_{\Delta\theta=\sqrt{3}\Gamma/6} = (1 - T_{min})\frac{3\sqrt{3}}{4\Gamma} \tag{8.14}$$

For a micro-ring resonator with certain loss α, the transmission coefficient τ should be set for maximising the selected slope $(\partial T/\partial\theta)_{max}$, at

$$\tau = \sqrt{\alpha} \tag{8.15}$$

Eq. 8.15 can be achieved by adjusting the gap between the micro-ring waveguide and the directional coupler. However, due to the unpredictability of waveguide losses, this requirement is difficult to fulfill precisely in design phase. In practice, the optimum design is normally found by performing measurements on directional couplers with varying gap scales within a certain range.

With the above insights in mind, the optical sensitivity in practice can be written as follows according to Eq. 8.1, 8.14 and 8.3

$$\begin{aligned} \frac{\partial T}{\partial b} &= \left(\frac{\partial T}{\partial \theta}\right)_{max} \cdot \frac{\partial \theta}{\partial b} \\ &= (1 - T_{min}) \frac{3\sqrt{3}}{4\Gamma} \cdot \frac{4\pi^2}{\lambda} n_e \\ &= (1 - T_{min}) \frac{3\sqrt{3}\pi^2 n_e}{\Gamma \lambda} \end{aligned} \tag{8.16}$$

There are two more conclusions that can be drawn from the above derivation. Under the condition of Eq. 8.13, it can also be observed from Eq. 8.9, 8.3 and 3.14 that

$$\begin{aligned} \frac{\partial \theta}{\partial b} &= \frac{2m\pi + \Delta\theta}{b} \\ &= \frac{12m\pi + \sqrt{3}\Gamma}{6b} \end{aligned} \tag{8.17}$$

Considering that the variation of the loss coefficient α is relatively small, it can be concluded from Eq. 8.16 and 8.17 that the maximum optical sensitivity of a micro-ring resonator system is inversely proportional to the micro-ring radius b.

The next discussion is about the approximation of the laser wavelength λ. Within the design space, the Free Spectral Range (FSR) of the resonance peak around the telecommunication wavelength of $1550\ nm$ can be estimated with Eq. 3.17 to the order of approximately $10^1 \sim 10^2\ nm$. Therefore, it is quite easy to select a resonance peak near the $1550\ nm$ wavelength, with a difference of no more than 10%. In the calculation of the optical sensitivity $\partial T / \partial b$, the laser wavelength can be estimated as $1550\ nm$ without much error, though it should be tuned on the nearby resonance peak in practice.

9

Results and Assessment

9.1. Complete Opto-Mechanical Sensor Design

In Chapter. 7 and 8, the analyses are carried out from the mechanical and optical aspects, based on which the criterion for the determination of the design variables are presented. However, a comprehensive analysis reveals that two design variables, membrane thickness t_{mem} and micro-ring radius b, are inherently opto-mechanically coupled and exhibit opposite effects on the mechanical and optical sensitivity. In this section, some more in-depth discussions are performed within the multi-physics scope, and the evaluation criterion for the present opto-mechanical AE sensor is provided.

9.1.1. Opto-Mechanical Analysis

Membrane Thickness

Since the proposed concept involves a micro-machined membrane with built-on micro-ring resonator, the design variable t_{mem} actually plays the role of both the membrane thickness and the slab thickness of the rib waveguide.

In the context of bare membrane configuration, according to Eq. 7.35, the increase of membrane thickness can reduce the net micro-ring elongation and thus the mechanical sensitivity under the same membrane deformation. Fig. 8.4 reveals an opposite pattern, that is, a larger membrane thickness brings a higher effective refractive index and thus the optical sensitivity.

In the equations of system sensitivity, both the radial displacement and the effective refractive index of the micro-ring waveguide appear as first-order factors. In comparison, the effective refractive index shows a much slower trend. Thus, one can confidently select the smallest possible membrane thickness t_{mem} in design space to obtain largest micro-ring elongation.

The membrane-with-cladding configuration is slightly different. According to Eq. 7.48, with a constant total thickness of silicon waveguides, the micro-ring deformation is only related to the height of neutral plane. For a standard two-layer micro-machined membrane, Eq. 7.47 reduces to

$$Z = \frac{E_1 t_1^2 + E_2 t_2^2 + 2E_2 t_1 t_2}{2(E_1 t_1 + E_2 t_2)} \tag{9.1}$$

where the subscript 1 stands for the silicon waveguide layer, and 2 the SiO_2 or Si_3N_4 cladding. The subscript of neutral plane is omitted for brevity.

Deriving the above equation for t_1 and t_2 respectively, we have

$$\frac{\partial Z}{\partial t_1} = \frac{1}{2} + \frac{(E_1 - E_2)E_2 t_2^2}{2(E_1 t_1 + E_2 t_2)^2} \tag{9.2}$$

$$\frac{\partial Z}{\partial t_2} = \frac{E_1 E_2 t_1^2 + 2E_1 E_2 t_1 t_2 + E_2^2 t_2^2}{2(E_1 t_1 + E_2 t_2)^2} \tag{9.3}$$

Both Eq. 9.2 and Eq. 9.3 are obviously greater than 0. Therefore, the mechanical sensitivity of the system increases as the thickness of each layer increases, which leads to an opposite conclusion that a greater silicon layer thickness should be considered for the configuration with cladding.

There are two other points to be made about the above discussion. First, the stiffness variation due to different flexural rigidity is neglected in the above discussion due to its small ratio to that from initial stresses, nor the damping ratio difference. In other words, the shift in resonance frequency and amplitude caused by the above variables is not taken into account. In practice, however, excessive membrane thickness may indeed lead to a decrease in mechanical response, thus design decisions requires reference to actual simulation results. The second note is that both the slab thickness and the cladding thickness can affect the electromagnetic wave modes supported by the waveguides. For simplicity, only the $TE_{0,0}$ mode is considered.

Micro-Ring Radius

According to Section. 7.2, micro-ring radii of $50 \sim 75\%$ the membrane radius result in largest radial displacement thus largest elongation. Simultaneously, Eq. 8.17 demonstrates that the optical sensitivity of the system is inversely proportional to the micro-ring radius. Since the optical sensitivity changes more rapidly with the micro-ring radius than the mechanical sensitivity, it seems reasonable to have the smallest possible micro-ring radius b.

However, all of these inferences are made with an assumption of low optical losses, which is very likely to be undermined as the micro-ring radius decreases. For further clarification, an estimation is made with regard to the numerical simulations by A. Brimont. et al. [77]. For a micro-ring resonator of $15\,\mu m$ radius, the bending-induced losses reaches a level of $0.75\,dB/90°$, which consequently results in an overall loss $\alpha^2 = 0.50$ ($-3.02dB$). This goes well beyond the acceptance of optical losses. Hence, a threshold for optical losses of $\alpha^2 = 0.90$ ($-0.46dB$) should be set beforehand as a criteria for micro-ring radius determination, with a corresponding radius of around $25\ \mu m$.

9.1.2. Performance Evaluation

As stated in Section. 2.2, the performance of AE sensors is usually determined with the systematic frequency response. In the present design, since only the first eigen mode of the micro-machined membrane is considered, the performance specifications of the opto-mechanical AE sensor are assessed around the first-order resonance frequency instead of the whole frequency range. The performance evaluation involves the following main aspects:

Frequency Response

The evaluation is first performed in terms of the mechanical frequency response via numerical simulations on COMSOL Multiphysics 6.0. Considering that the responses at all levels of the system are linear, the resonance peaks and the corresponding 6-dB bandwidths of the sensor can be primarily determined in terms of the displacement at the micro-machined membrane centroid or the average radial displacement within the rib waveguide area.

Sensitivity Analysis

As the second step, the systematic sensitivity is calculated according to Eq. 5.12, Eq. 7.33 and Eq. 8.1. The sensitivity of the proposed opto-mechanical ultrasonic wave sensor can be described in terms of the partial derivative $\partial T/\partial x_f$ in the extended form

$$\frac{\partial T}{\partial x_f} = \frac{\partial T}{\partial \theta}\frac{\partial \theta}{\partial b}\frac{\partial b}{\partial w_0}\frac{\partial w_0}{\partial x_f} \tag{9.4}$$

where the values of the first two factors are provided by Eq. 8.16 and the rest by numerical simulations.

Bandwidth Analysis

The bandwidth of the proposed sensors can be characterized in two ways, as specified in Section. 4.1. The 6-dB resonant bandwidth can be obtained from the mechanical frequency response. Since the frequency of AE signals in civil engineering materials is generally ranged from $20\ kHz$ to $1\ MHz$ [22], the operating frequency range above $35\ dB$ is determined with the frequency response curves within this range.

Signal-to-Noise Ratio

Third, the SNR of the sensor is estimated on the basis of the specifications of involved devices and some assumptions.

The systematic noise consists of two main aspects: the thermo-mechanical noise from the mechanical resonator, and the electro-optical noises from the optical system. The respective definitions and calculation approaches are as follows:

- **Thermo-mechanical noise**: For most MEMS sensors, the fundamental noise limit is imposed by thermo-mechanical motions of the micro-mechanical resonators. Briefly, the modes of the resonator can be excited by a thermo-mechanical noise force even in the absence of any external loads. The equivalent pressure is in the form of

$$P_{noise} = \sqrt{4kT\Delta f R_a} \tag{9.5}$$

  where $k = 1.38 \times 10^{-23}\, J/K$ is Bolzmann's constant, T the thermodynamic temperature and Δf the specified bandwidth. R_a is the acoustic resistance, related with the system damping.

  Due to the fact that the AE sensors in this project are mostly used in outdoor environments with a wide range of temperature variations, and due to the lack of detailed information on the damping of the system, it is very difficult and of little significance to estimate the thermo-mechanical noise. In this project, more emphasis are placed on the noises in the electro-optical system, which is indeed the main difference from conventional piezoelectric and MEMS sensors.
- **Laser Noise**: The noises of the laser source can be broadly divided into two parts, namely amplitude and frequency noise. The laser produced by an ideal laser source has a constant amplitude and single frequency. In practice, however, both the two values change randomly within some range. Since the sensing system is designed to detect ultrasonic waves by measuring transmitted light intensity, the variation in laser amplitude can directly lead to errors in output transmittance. The frequency noise, also referred to as wavelength noise, can lead to random shifts on the transmittance spectrum of micro-ring resonators, and thus errors in the measurement.
- **Photo-Detector Noise**: There is some noise introduced by photo-detectors in the conversion of optical intensity to voltage. Such noise can be obtained from the product instructions as *output noise* or *integrated noise*, representing the range of fluctuation in voltage output.

It should be noted that, since latter two types do not influence the noise level of passive opto-mechanical sensors, they are not necessarily part of the design phase in this project. However, for integrated photonic sensors with on-chip laser sources and photo-detectors, or complete, AE detection nodes with embedded laser sources and photo-detectors, the design or selection of such devices can be an important part for product design. Therefore, rough estimations of the above noises are still provided in this paper for each design. The SNR of the system is defined as

$$SNR = 20 \log_{10}\left(\frac{V_{signal}}{V_{noise}}\right) \tag{9.6}$$

9.2. Prototype 1: Design and Assessment

In the thesis, two configurations are investigated for AE detection, one based on bare micro-machined membranes and the other based on micro-machined membranes with cladding.

For reasons of manufacturing cost and simplicity, a bare membrane configuration without cladding is first considered. On the basis of the design guidelines in Section. 9.1, the opto-mechanically coupled design variables, membrane thickness t_{mem} and micro-ring radius b can be determined. For achieving largest possible waveguide deformation, the membrane thickness t_{mem} is set to $100\ nm$, being the minimum within design space. The micro-ring radius is set $25\ \mu m$ to achieve highest possible optical sensitivity within the optical loss threshold $\alpha^2 = 0.90$.

Based on the required centre frequency as design specification in Section. 4.1, the micro-machined membrane should exhibit the first-order eigen frequency at $100\ kHz$. According to Eq. 7.20 and transformed Eq. 7.32, we have

$$f_c = \frac{\sqrt{k_{00}^2 D + \alpha_{01}^2 R^2 S}}{2\pi\sqrt{\sigma} R^2} \tag{9.7}$$

$$D = \frac{E t_{mem}^3}{12(1-\nu^2)} \tag{9.8}$$

where f_c refers to the centre frequency of $100\ kHz$. Eq. 9.7 and 9.8 lead to a membrane radius of $561\ \mu m$ with $50\ MPa$ initial stress assumed.

Subsequently, Eigenfrequency analysis is carried out on this model in COMSOL Multiphysics 6.0. The calculated first-order eigen frequency is $100.25\ kHz$, which is acceptable within tolerance. This results in the first prototype design, as shown in Fig. 9.1 and 9.2.

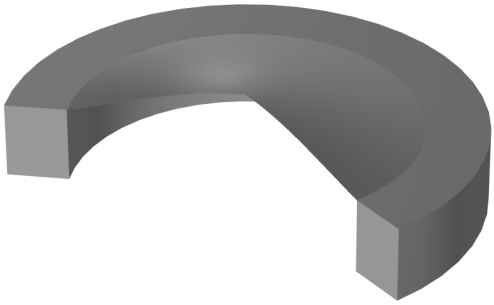

Figure 9.1: 3D model of the opto-mechanical ultrasonic wave sensor (prototype 1).

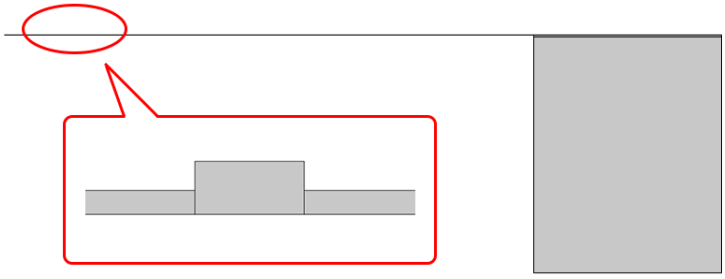

Figure 9.2: Cross-sectional diagram of the photonic micro-mechanical ultrasonic wave sensor (prototype 1).

9.2.1. Frequency response

The frequency response of the proposed prototype is carried out with the frequency domain module in COMSOL Multiphyiscs 6.0. A displacement input of $1\,nm$ is imposed on the bottom of the substrate and the frequency range is set as an exponential function (base 10) from 10 to $1000\,kHz$ with an interval of $exp10(0.001)\,kHz$. Based on engineering experiences, the material damping of silicon is estimated with 0.01 isotropic loss factor. The response at the membrane centroid under $1\ nm$ displacement excitation over the considered frequency range is shown in Fig. 9.3.

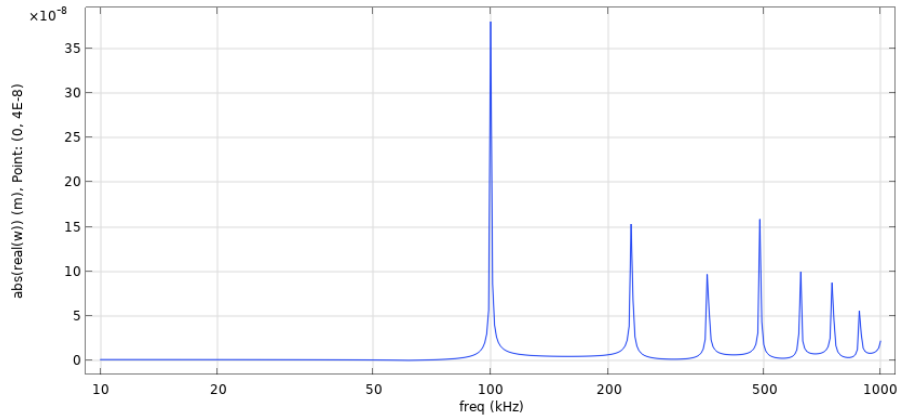

Figure 9.3: Frequency responses of micro-machined membrane, under $1\ nm$ displacement excitation.

As seen in the plot, the micro-machined membrane shows the first resonance peak at about$100\,Hz$.

As mentioned earlier, since the resonance of the micro-machined membrane does not necessarily correspond to the maximum elongation of the attached micro-ring resonator, the higher order resonance peaks here are not part of the operating frequency range.

Two main problems are exposed in the investigation of frequency response. First, the system bandwidth around the centre frequency of $100\ kHz$ is quite narrow. With the current damping level and a refined simulation step size of $exp10(0.00002)\ kHz$, the system exhibits a 6-dB bandwidth of about $0.02kHz$. Second, the mechanical effect of the rib waveguide can no more be neglected in forced vibration. As shown in Fig. 9.4, anomalous bending is evident in the vicinity of the micro-ring resonator both at rest and under $100\ kHz$ excitation. This implies that the micro-ring resonator exhibits non-uniform shortening at rest and remains shortened throughout the whole vibration cycle around resonance, even in the case of membrane up-convexity.

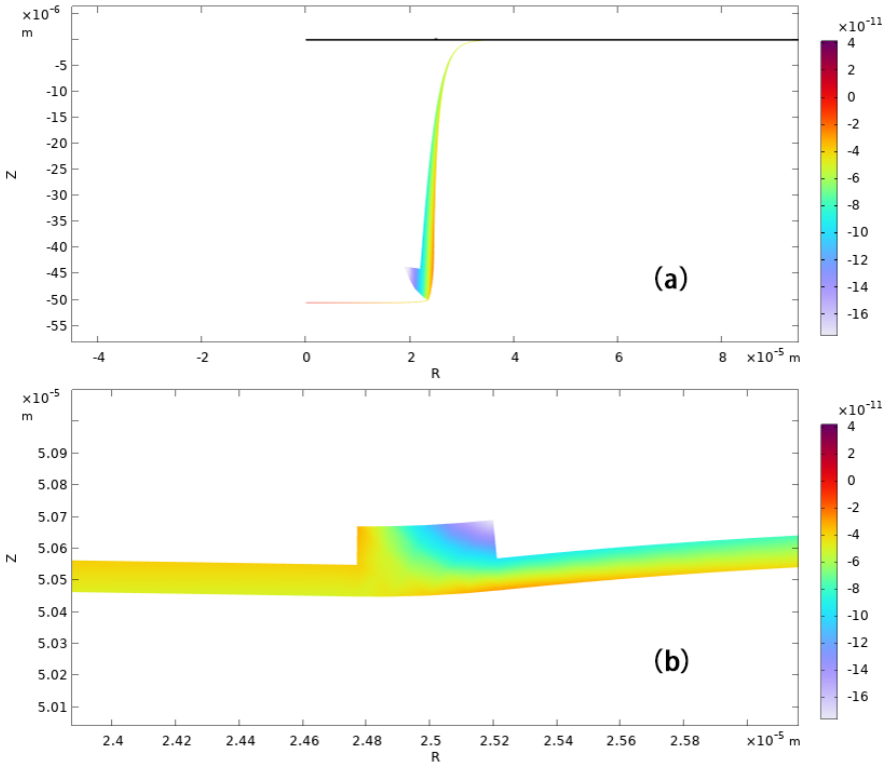

Figure 9.4: Radial displacement (unit: m) in and around the rib waveguide, (a) at rest, (b) under $1\ nm$, $100\ kHz$ displacement excitation, membrane up-convexity.

Since the AE wave detection relies on the circumference change of micro-ring resonators, the effective deformation is embodied by the radial displacement under excitation minus that at rest. From numerical simulations by COMSOL Multiphysics 6.0, the radial displacement over the micro-ring waveguide area is $-7.87\times10^{-11}m$ at rest, which is in the same order of magnitude as that under $1nm, 100kHz$ displacement excitation ($-7.16\times10^{-11}\ m$). Such an insignificant difference in displacement is inconsistent with the original design intent and does not allow for effective perception of AE waves.

9.2.2. Failure Analysis

In this present design, micro-machined membranes with tensile initial stresses are considered. For the cases without the rib waveguide, stresses are uniformly distributed in the membrane. The mechanical analysis for an arbitrary piece of the membrane is shown in Fig. 9.5, where subplot (a) and (b) show the distribution of internal tensile stresses on the radial cross section of the membrane at rest and under vibration, respectively. In the material reference system, the internal stresses are larger on the convex side due to the inertial force during vibration.

In micro-machined membranes with rib waveguides, since the radial component of initial stresses in the rib is released, the stress transmission is cut off. As a result, the radial stress on the membrane top surface is no longer continuous. The micro-machined membrane is divided into an outer ring-

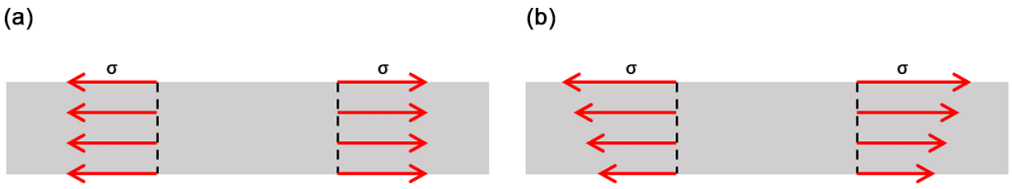

Figure 9.5: Schematic diagram of internal stress distribution on the radial cross section of micro-machined membranes without rib waveguides. The inertial force and membrane deformation have been omitted.

shaped area and an inner circle by the ”rigid” micro-ring resonator, and the vibration of the micro-machined membrane no longer follows the single membrane or ”membrane-plate” model. In terms of the generalised mass-spring system, the micro-machined membrane should now be modelled as two springs in series, where the inner part, due to its smaller radius, has a much higher equivalent stiffness than the outer part. As a result, the motion of the outer ring still approximately follows the analytical ”membrane-plate” model, while the inner part remains almost horizontal in tension, with only vertical translation.

The radial stress distribution inside the membrane with rib waveguides during vibration is shown schematically in Fig. 9.6 (a). Since the membrane at the outside of the micro-ring resonator is further stretched during vibration, its average stress along the thickness direction is higher than that of the circled portion. Under this pair of forces, the rib waveguide tends to rotate or bend along the ϕ axis.

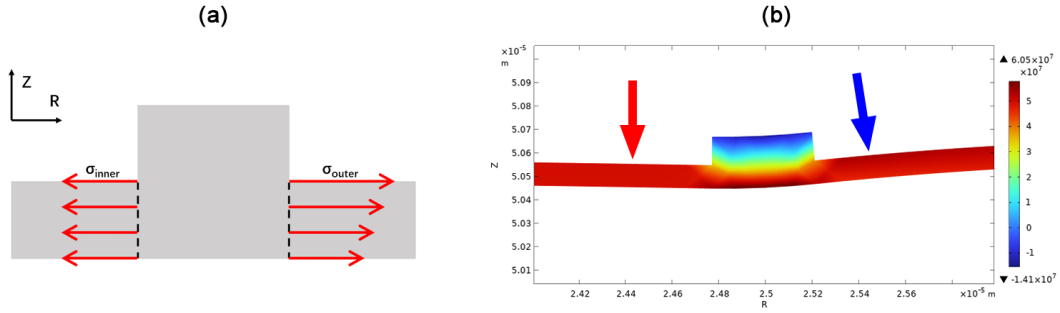

Figure 9.6: Internal stress distribution on the cross section of micro-machined membranes with rib waveguides. (a) Schematic diagram, with the membrane deformation omitted. (b) Simulation result (unit: MPa), showing the radial component of internal stress.

The above inference is confirmed by simulation results. As shown in Fig. 9.5 (b), under $100\ kHz$ excitation, the internal stress at the inner portion of the membrane (red arrow) remains approximately $50\ MPa$, while the highest stress level on the outer top surface (blue arrow) reaches around $54\ MPa$. This strong force causes the silicon rib waveguide to bend in the radial cross section.

9.3. Prototype 2: Design and Assessment

Due to the above problems, modifications need to be made on the first prototype. The introduction of an on-membrane cladding is expected to help with maintaining the continuity of the internal stress, thereby eliminating local deformation under forced vibration. Among the considered cladding materials, Si_3N_4 has the advantage of higher refractive index. However, due to the lack of knowledge on manufacturing details, such as cost and precision, both SiO_2 and Si_3N_4 claddings are considered.

According to the discussion in Section. 9.1, the original silicon membrane thickness is taken the maximum within the design space, i.e. $150\,nm$, to achieve the largest possible micro-ring elongation as well as high effective refractive index. According to Eq. 7.47, in order to ensure that the neutral plane is higher than half of the total waveguide thickness, the thickness of SiO_2 and Si_3N_4 cladding should be at least $138\,nm$ and $62\,nm$. For Si_3N_4 cladding, the thickness should not be less than $80\,nm$ to ensure proper coverage of the rib waveguide. Though it emerges in theory that larger cladding thickness leads to greater micro-ring elongation, the optimal value should be determined with simulation results due to possible complex effects. To minimize the sensor footprint, cladding with lower initial stress should be

selected. Here, we consider tensile stress of $50\ MPa$ for predictable design outcomes.

The rest of the design process is similar to that in the previous section. According to the theory in Section. 7.3, the membrane radius can be roughly determined, which is subsequently checked via numerical simulation on COMSOL Multiphysics 6.0. This leads to the second design prototype, as shown in Fig. 9.7 and 9.8.

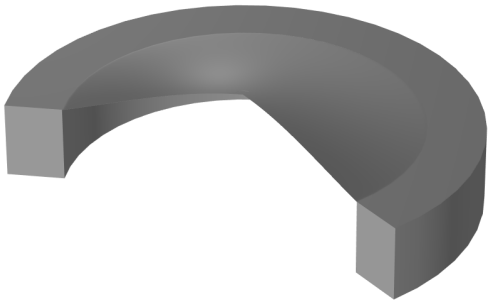

Figure 9.7: 3D model of the opto-mechanical ultrasonic wave sensor (prototype 2).

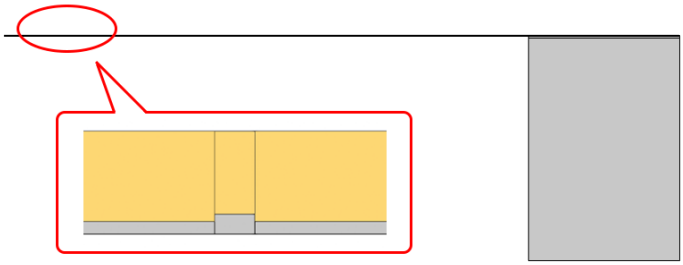

Figure 9.8: Cross-sectional diagram of the photonic micro-mechanical ultrasonic wave sensor (prototype 2).

The correspondence between the radius of micro-machined membranes of $100\ kHz$ centre frequency and two cladding thicknesses is shown below. The Si_3N_4 cladding allows smaller membrane radius for the given centre frequency. Since the membrane radius does not change much with the cladding thickness, it can be approximated that the change in cladding thickness has minor effect on the system stiffness.

Table 9.1: Radii of micro-machined membranes of $100\ kHz$ centre frequency with different cladding thicknesses.

Cladding thickness / nm	Membrane radius (SiO_2 cladding) / nm	Membrane radius (Si_3N_4 cladding) / nm
600	584	514
1000	590	519

It is also evident from Tab. 9.1 that the micro-ring radius of $25\ \mu m$ is less than 5% of the membrane radius, which bodes well for the potential of the sensor to operate at higher frequencies. According to Sub-Section. 7.1.2, micro-ring resonators of such scale are hardly affected by nodal circles at higher-order resonance. The operating frequency range of the proposed sensor will be discussed in more detail below.

9.3.1. Frequency Response

As described in the previous section, the functioning of proposed AE sensors can be determined with the response around the $100\ kHz$ centre frequency. Here, the average radial displacement over the rib waveguide area is employed. Taking the SiO_2 cladding as an example, the radial displacement at resonance with regard to cladding thickness is shown in Fig. 9.9.

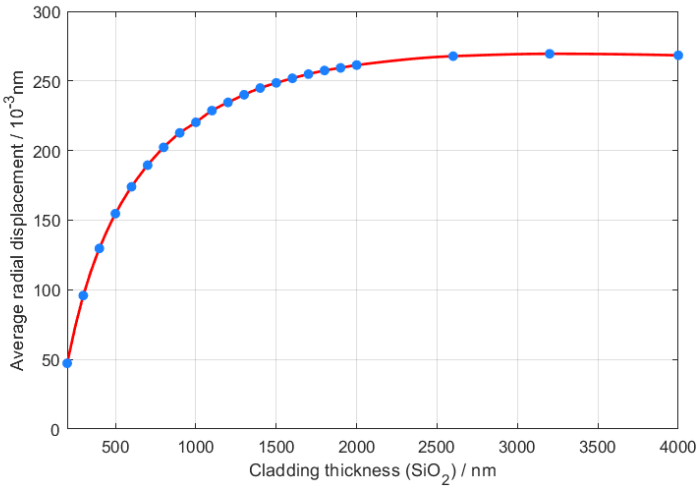

Figure 9.9: Resonant radial displacement of micro-machined membranes with SiO_2 cladding of different thickness, under $1\ nm$ displacement excitation.

It should be noted that, due to the extremely narrow bandwidth of the system, the simulation step size needs to be refined to capture the resonant frequency response. In this part, we set the step size at $exp10(0.00001)\ kHz$.

As discussed in theoretical analyses, according to Eq. 7.48, 9.1 and 9.3, the increase in cladding thickness leads to greater radial deformation of the micro-ring resonator. However, due to the induced larger material damping, the radial displacement almost ceases to grow at cladding thickness larger than $2500\ nm$. Considering that larger cladding thickness results in larger sensor footprints and higher processing cost, it is reasonable to choose the thinnest possible cladding if the performance difference is not significant. Therefore, the optimal thickness of SiO_2 cladding with $50\ MPa$ initial stress is determined $2500\ nm$, corresponding to a membrane radius of around $611\ \mu m$.

As a comparison to the previous prototype design, the radial displacement of prototype 2 at resonance is shown in Fig. 9.10. The displacement field is proved smooth and free of anomalous local deformations.

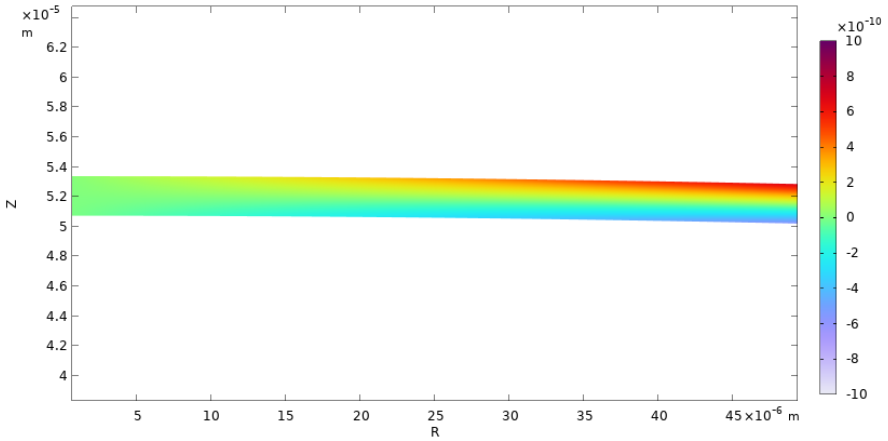

Figure 9.10: Radial displacement in and around the rib waveguide on the micro-machined membrane with $2500\ nm\ SiO_2$ cladding at resonance, under $1\ nm$ displacement excitation.

The mechanical frequency response of a micro-machined membrane with $2500\ nm$-thick SiO_2 cladding around resonance is shown below. The present design exhibits two resonance peaks around $100\ kHz$. Though with a dip in the middle, such phenomenon actually extends the frequency range of resonance. The 6-dB bandwidth of the present model is about $0.265\ kHz$, which is about 13 times larger than that of prototype 1.

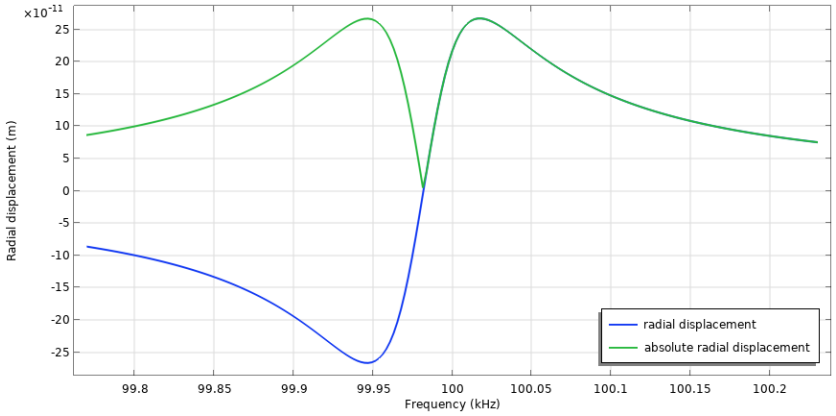

Figure 9.11: Frequency response of micro-machined membrane with $2500\ nm$-thick SiO_2 cladding, under $1\ nm$ displacement excitation.

The bi-modal phenomenon in Fig. 9.11 alerts to the mechanical complexity of micro-machined membranes with cladding. Although predictions can be made about the overall behavior of such membranes with the generalized mass-spring system and the classical laminated plate theory, the actual vibration phenomenon still shows more details than the simplified model. The difference in mechanical properties between the silicon layer and the cladding is the underlying cause of this phenomenon. In the above simulations, assumed constant isotropic loss factors are applied to both layers, which results in a slight phase difference in vibration between them. This consequently forms two adjacent resonance peaks, which are very close to each other but in opposite phases, around the overall eigen frequency.

This effect also emphasizes the importance of step-size refinement in numerical simulations of frequency response. Since the geometrical parameters that satisfy the required overall eigen frequency ($100\ kHz$) can produce two resonance peaks, it is not always possible to determine the maxima with larger step sizes. Most likely, the simulation yields a value that lies between the two peaks, leading to significant scattering of numerical results. An example is provided in Fig. 9.12, where the step size is set to $exp10(0.01)\ kHz$.

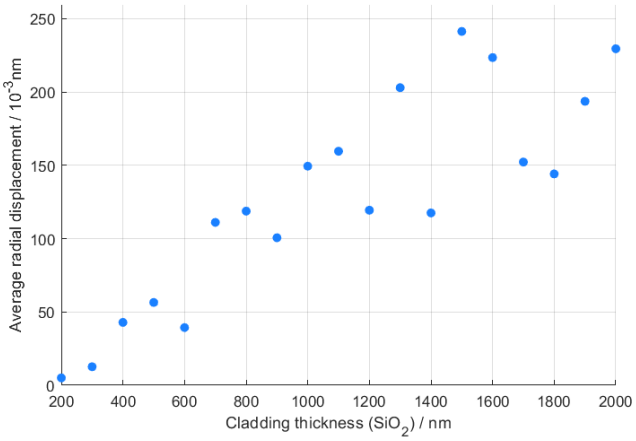

Figure 9.12: Resonant radial displacement of the micro-machined membrane with SiO_2 cladding of different thickness, under $1\ nm$ displacement excitation of $exp10(0.01)\ kHz$ step size.

In terms of the absolute amplitude, as is mentioned, there is a narrow dip near the centre frequency. Since the phase difference between the two resonance peaks is very small, the dip does not have dramatic effects on the functioning of the sensor, but rather expands the resonant bandwidth. It is therefore an advantage.

In addition to SiO_2, Si_3N_4 cladding is also investigated, whose optimal thickness appears at around $1000\ nm$. The corresponding membrane radius is $519\ \mu m$. The mechanical frequency response of the

micro-machined membrane with $1000\,nm$-thick Si_3N_4 cladding around resonance is shown in Fig. 9.13. The resulting resonant radial displacement under $1\ nm$ excitation is approximately $196.7 \times 10^{-3}\ nm$, and the 6-dB bandwidth is about $0.214\,kHz$.

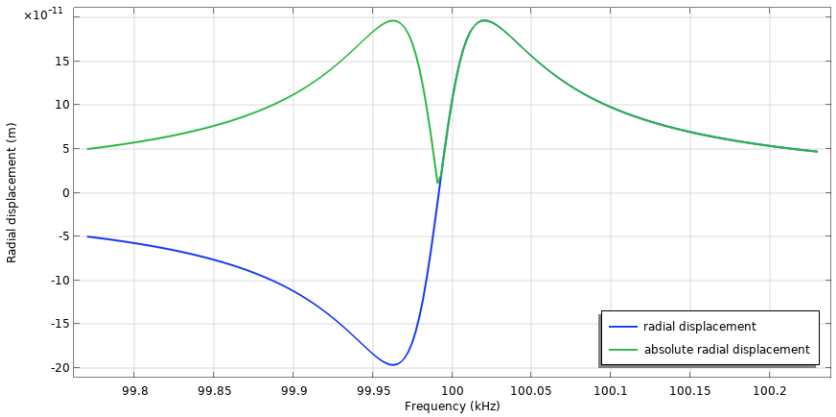

Figure 9.13: Frequency response of micro-machined membrane with $1000\,nm$-thick Si_3N_4 cladding, under $1\,nm$ displacement excitation.

9.3.2. Sensitivity

The displacement sensitivity of opto-mechanical AE sensor with SiO_2 cladding is first calculated. According to Fig. 9.11, for a micro-machined membrane with SiO_2 cladding of $2500\ nm$ thickness under a displacement excitation of $1\ nm$ at $100\ kHz$, the radial displacement of the rib waveguide is $2.671 \times 10^{-10}\ m$. This yields a mechanical sensitivity

$$\frac{\partial b}{\partial x_f} = 0.2671 \tag{9.9}$$

The optical sensitivity can be calculated with Eq. 8.16, 8.11 and 8.12 under the condition of 8.15. As stated in Section. 9.1, the squared loss coefficient α^2 of a micro-ring resonator of $25\ \mu m$ radius is taken 0.9. For the given silicon rib waveguide with $2500\ nm\ SiO_2$ cladding, the effective refractive index $n_e = 2.63123915$, calculated with the mode solver for $2D$ multi-layer waveguides provided by M. Hammer [74]. The optical sensitivity is thus determined as

$$\frac{\partial T}{\partial b} = 4.896 \times 10^8\ m^{-1} \tag{9.10}$$

According to Eq. 9.4, the systematic sensitivity is given by

$$\frac{\partial T}{\partial x_f} = 1.33 \times 10^8\ m^{-1} \tag{9.11}$$

As stated before, the optical signals in photonic systems can be converted into electric signals with photo-detectors. Here the 1811-FC InGaAs Fiber-Optic Receiver® of Newport Corporation is employed, whose conversion gain is $4 \times 10^4\ V/W$. The overall sensitivity can be described with

$$\frac{\partial V}{\partial x_f} = \frac{\partial V}{\partial T}\frac{\partial T}{\partial x_f} \tag{9.12}$$

Assuming an optical power of $1\ mW$ into the photo-detector, the overall displacement sensitivity off the sensor is $5.32\ V/nm$, at the centre frequency of $100\ kHz$. As introduced in Section. 2.2, the velocity sensitivity can also be derived from the displacement sensitivity by dividing it with the angular frequency. This ends up with $8467.04\ V/(m/s)$ or $78.55\ dB(V/(m/s))$. Following the same steps, the displacement and velocity sensitivities of the opto-mechanical AE sensor with $1000\,nm\ Si_3N_4$ cladding are $3.95\,V/nm$ and $75.96\,dB(V/(m/s))$, respectively. The maximum velocity sensitivities of two design options are roughly in the order of magnitude of current commercial piezoelectric sensors, both of which exceed the design target of $60\ dB(V/(m/s))$.

Bases on the above equations, the frequency response curves of the proposed opto-mechanical AE sensors with two cladding materials are shown in Fig. 9.14, obtained with simulations by COMSOL Multiphysics 6.0. The simulation step size is set to $exp10(0.002)kHz$. As predicted earlier in this section, the deformation of micro-ring resonators is not affected by the nodal circles at higher frequencies, thus the frequency response of proposed AE sensors shows all 5 or 6 resonance peaks in the frequency range of $20 \sim 1000kHz$. In fact, the curves are conservative in their reflection on the performance of both sensor designs, since there are actually asymmetric vibration modes that are not considered in this project. Two design options exhibit very similar performance within the considered frequency range, of which the sensor with SiO_2 cladding shows slightly higher sensitivity.

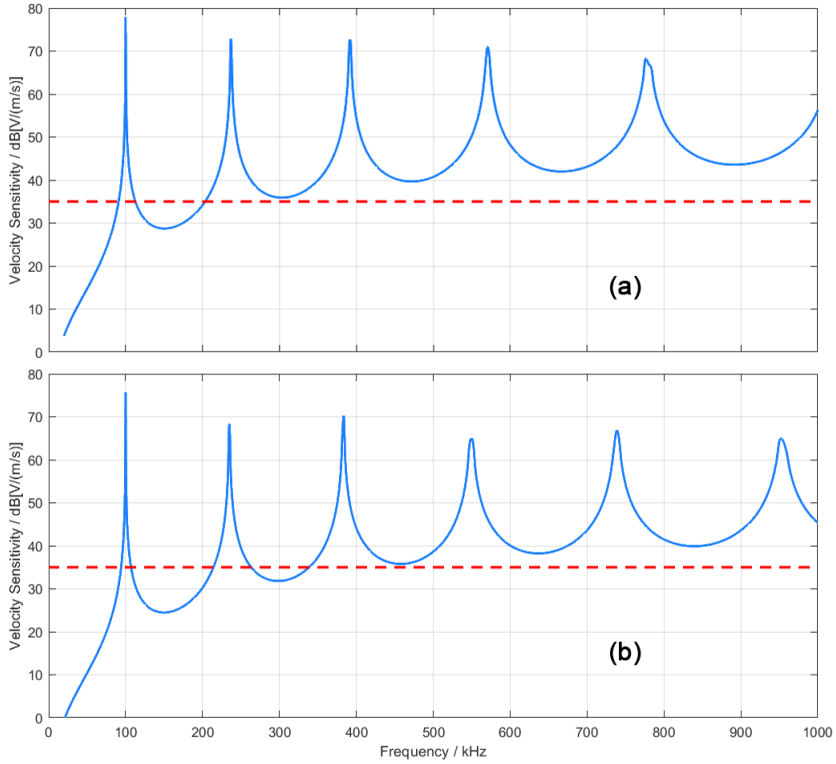

Figure 9.14: Frequency response curves of opto-mechanical AE sensors with (a) SiO_2 and (b) Si_3N_4 cladding.

9.3.3. Bandwidth

According to the definition of sensor bandwidth in Section. 4.1, the 6-dB bandwidth around the $100\,kHz$ resonance frequency and the operating frequency range with $35\,dB$ threshold are investigated. From Sub-Section. 9.3.1, the proposed AE sensors with SiO_2 and Si_3N_4 cladding exhibit 6-dB resonant bandwidths of $0.265\,kHz$ and $0.214\,kHz$, respectively.

By adding external damping, such as gases with different pressures, a larger resonant bandwidth can be achieved. An example on the AE sensor with SiO_2 cladding is provided in Fig. 9.15, obtained with simulation by COMSOL Multiphysics 6.0. Though with a dip at around $100kHz$, the 6-dB bandwidth around the first-order resonance exceeds $50\,kHz$. Since the discussions on the micro-chip packaging form is beyond the scope of this project, the increased damping in this example is realized simply with a larger isotropic loss factor of 5. This treatment is definitely not rigorous, but provides a good demonstration of the damping effect.

It is also observed in Fig. 9.15 that the two resonance peaks are much lower than that with smaller damping. This is consistent with the theoretical analysis illustrated with Fig. 5.2 and 5.3, that is, the increase in damping leads to lower peaks at resonance. According to Section. 4.1, sensitivity is the first priority of this work. Therefore, such design trade-off requires extremely careful consideration. In other words, though a narrow resonant bandwidth is usually the case for resonant AE sensors, it is not necessarily to be avoided, especially if sensitivity is sacrificed.

In terms of the second definition of bandwidth in this project, the proposed AE sensors with SiO_2

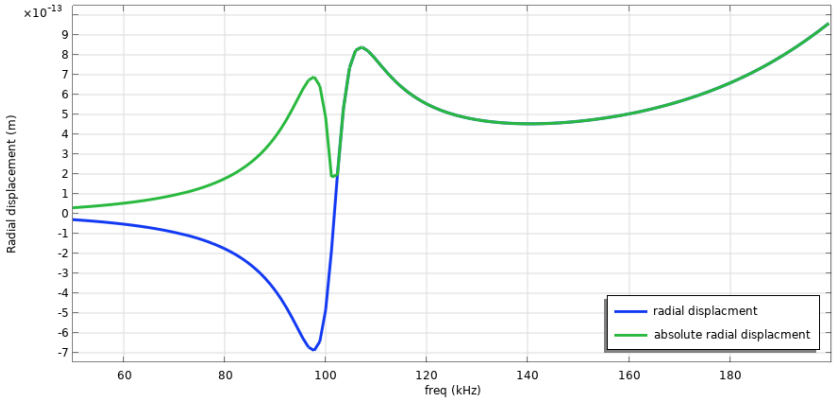

Figure 9.15: Frequency responses of micro-machined membrane with $1000\,nm$-thick SiO_2 cladding, under $1\,nm$ displacement excitation and isotropic loss factor of 5.

and Si_3N_4 cladding both exhibit an operating frequency range of $100 \sim 1000\,kHz$ with above $35\,dB$ response, though a truncated interval occurs within $100 \sim 200\,kHz$. Such kind of transient drop in frequency response is also very common in conventional piezoelectric sensors, and its actual effect on AE detection is to be further explored by sensor characterization and signal testing in laboratory. So far, considering the effects of ignored asymmetric vibration modes, optimistic prediction is made on this issue.

9.3.4. Signal-to-Noise Ratio

In this project, the estimation of system noise mainly involves the laser noise and the photo-detector noise, as described in Section. 9.1.2. Here the laser source 81940A Compact Tunable Laser Source® from Keysight Technologies is selected. The photo-detector selection is the same as in sensitivity calculation, i.e. 1811-FC InGaAs Fiber-Optic Receiver®.

According to the User's Guide, the selected laser source exhibits a relative wavelength accuracy of $\pm 10\,pm$, which is defined by half the span of the maximum and minimum value of difference between the displayed wavelength and the actual wavelength over the full wavelength range.

The laser amplitude noise, or in the name of laser power noise, is estimated with the provided *Relative Intensity Noise (RIN)* in dB/Hz, defined by

$$RIN_{dB/Hz} = 10\log_{10}\left(\frac{\Delta P^2 \cdot 1Hz}{P_{avg}^2 \cdot B}\right) \tag{9.13}$$

where ΔP refers to the optical power fluctuation amplitude, P_{avg} is the average optical power. B is the bandwidth of $3\,MHz$.

Following the same setting as the previous sub-section, the average optical power is $1mW$. According to the User's Guide, the 81940A Compact Tunable Laser Source® exhibits a RIN of $-145dB/Hz$. This yields an optical power fluctuation amplitude of $9.74 \times 10^{-5}\,mW$

The effect of laser wavelength noise on the system output is through influencing the optical sensitivity $\partial T/\partial b$. According to Eq. 8.16, 8.11 and 8.12, the output transmittance fluctuation due to laser wavelength noise is given by

$$\Delta\left[\frac{\partial T}{\partial b}\right] = (1 - T_{min})\frac{3\sqrt{3}\pi^2 n_e}{\Gamma} \cdot \left(\frac{1}{\lambda - \Delta\lambda} - \frac{1}{\lambda + \Delta\lambda}\right) \tag{9.14}$$

Thus we have

$$\Delta\left[\frac{\partial T}{\partial b}\right]_{SiO_2 \ \ cladding} = 6.32 \times 10^3\ m^{-1} \tag{9.15}$$

$$\Delta\left[\frac{\partial T}{\partial b}\right]_{Si_3N_4 \ \ cladding} = 6.47 \times 10^3\ m^{-1} \tag{9.16}$$

The laser power noise acts directly on the transmittance spectrum, causing a transmitted power fluctuation.

According to the Law of propagation of error, the overall laser-induced noise is given by

$$\begin{aligned} Noise^2\left[\frac{\partial V}{\partial x_f}\right] &= Noise^2\left[\frac{\partial V}{\partial T}\frac{\partial T}{\partial x_f}\right] \\ &= Noise^2\left[4\times 10^4 \cdot P_{laser}\cdot \frac{\partial T}{\partial x_f}\right] \\ &= 1.6\times 10^9 \cdot \left[\left(\frac{\partial T}{\partial x_f}\right)^2 Noise^2\big[P_{laser}\big] + P_{laser}^2 Noise^2\big[\frac{\partial T}{\partial x_f}\big]\right] \\ &= 1.6\times 10^9 \cdot \left[\left(\frac{\partial T}{\partial x_f}\right)^2 Noise^2\big[P_{laser}\big] + P_{laser}^2\left(\frac{\partial b}{\partial x_f}\right)^2 Noise^2\big[\frac{\partial T}{\partial b}\big]\right] \end{aligned} \tag{9.17}$$

where $Noise\big[P_{laser}\big]$ refers to the laser power noise and $Noise\big[\frac{\partial T}{\partial b}\big]$ refers to the laser wavelength noise.

For the design with SiO_2 and Si_3N_4 cladding, the laser-induced noise are respectively

$$Noise\left[\frac{\partial V}{\partial x_f}\right]_{SiO_2\ \ cladding} = 5.15\times 10^{-4}\, V/nm \tag{9.18}$$

$$Noise\left[\frac{\partial V}{\partial x_f}\right]_{Si_3N_4\ \ cladding} = 3.88\times 10^{-4}\, V/nm \tag{9.19}$$

It is evident that the laser-induced noise is 4 orders of magnitude less than the signal, representing a small percentage of the total output.

According to the data sheet of 1811-FC InGaAs Fiber-Optic Receiver®, the photo-detector exhibits an integrated noise of around $5\ mV$, which is about 3 orders of magnitude less than the signal for nano-meter-scale displacement input of AE signals.

Thus, the SNR of the present system with regard to laser- and photo-detector-induced noises is around 60 to $80\ dB$. In practical application, the thermal-mechanical noise should also be taken into consideration, which is highly dependent on the micro-chip packaging form and the environmental temperature.

10

Design Proposal and Conclusion

10.1. Design Proposal

On the basis of all the above theoretical analyses, analytical calculation and numerical simulation, two promising design options are proposed. Both of the designs are based on the second prototype discussed in Section. 9.3, that is, opto-mechanical acoustic emission wave sensors based on micro-machined membranes with cladding.

The main difference between the two design options is the utilization of different cladding materials, namely SiO_2 and Si_3N_4. Since the mechanical and optical properties, such as Young's modulus, Poisson's ratio, refractive indices, etc., of these two materials are wildly divergent, design results with different footprints and performances are produced at the given operating frequency. A detailed comparison is made in the table below.

Table 10.1: Comparison on design variables and performances between design options with SiO_2 and Si_3N_4 cladding.

Design variable	Design 1 (SiO_2 cladding)	Design 2 (Si_3N_4 cladding)
membrane radius R_{mem}	$611\ \mu m$	$519\ \mu m$
cladding thickness t_{clad}	$2500\ nm$	$1000\ nm$
etching depth t_{rib}	$70 \pm 10\ nm$	
rib waveguide width w	$450\ nm$	
micro-ring radius b	$25\ \mu m$	
Performance specification	**Design 1 (SiO_2 cladding)**	**Design 2 (Si_3N_4 cladding)**
displacement sensitivity $[V/nm]$	5.32	3.95
velocity sensitivity $[dB(V/(m/s))]$	78.55	75.96
resonance frequency $[kHz]$	99.98	99.99
6-dB resonant bandwidth $[kHz]$	0.265	0.214
operating frequency range ($\geq 35\ dB$) $[kHz]$	$100 \sim 1000$	
signal-to-noise ratio (SNR)	$60 \sim 80\ dB$	

As a conclusion, the design option with SiO_2 cladding achieves a higher sensitivity, while the sensor with Si_3N_4 has a smaller radius of about 15% and thus better miniaturization, although the sensitivity is lower by $2.59\ dB$. Whereas, the sensitivity of both designs meets the target specification.

The bandwidth of proposed AE sensors are evaluated in two ways. One is the 6-dB bandwidth around the centre frequency of $100\ kHz$, which represents the frequency range where the system response drops to half of the resonance peak. The 6-dB bandwidth of both design options is within $0.2 \sim 0.3\ kHz$, due to the low damping coefficient of solid materials. A larger resonant bandwidth can be obtained by introducing external damping, such as pressurized gases, to the micro-chip package. However, extra care should be taken when introducing external damping as this can significantly reduce the sensitivity. The second bandwidth evaluation is built on a threshold of $35dB$ velocity response, which matches the commonly used value of commercial AE sensors. Both design options exhibit sufficient sensitivity within an operating frequency range of $100 \sim 1000\ kHz$.

In addition, the SNR of proposed AE sensors are estimated mainly in terms of the laser-induced and photo-detector noises. Both design options are expected to achieve a SNR of $60 \sim 80dB$. Thermo-mechanical noise is not accounted for in this project due to the lack of exact information on environmental temperature and system damping. Though in fact, this type of noise may plays a considerable part in the total system noise [56]. In terms of miniaturization, both design options are capable of a smaller footprint of about $1/40$ the size of conventional piezoelectric AE sensors.

In the design process, assumptions are employed due to the lack of some relevant information. The most important assumption is made on the initial stresses within layers of micro-machined membranes. The initial stress in the silicon waveguide layer is mainly due to thermal processes in the production of SOI wafers. The initial stresses in cladding is introduced by PECVD process, with a range of variation depending on the reaction conditions. In the present design, stresses in both layers are assumed $50MPa$, which is reasonable, but not necessarily the case in reality. In fact, initial stresses are related to the overall processing history, thus a wide range of values may be obtained. Since the initial stress has a significant effect on membrane dynamics, it is recommended that this parameter be characterized prior to actual modeling, processing and testing. A convenient method is to measure the eigen frequencies of a membrane with a certain thickness and radius.

Another important assumption is the damping. In this project, an isotropic loss factor of 0.01 is adopted as an empirical estimation of material damping. Since damping has a very pronounced effect on the vibration amplitude and hence the sensitivity of AE sensors, it is also essential to be characterized. Similarly, the damping of a micro-machined membrane with defined geometrical parameters can be determined by measuring the vibration amplitude. However, considering that the actual AE sensors consist of complex components such as optical and electrical elements, connections and packaging, it may not be economical to investigate the membrane damping separately. A more cost-effective option is to directly characterize the frequency response curves of complete AE sensors so that the contribution of all factors to damping is included.

In addition to this, the effects of processing errors and on-membrane connecting waveguides are neglected, which are minor but possibly have an impact on the final design results. Bottom line, all effective products come from extensive testing.

10.2. Conclusion

In this project, a photonic micro-mechanical ultrasonic wave sensor for acoustic emission non-destructive testing is proposed. Two design options based on different cladding materials are obtained, both of which not only meet the design requirements on technical specifications but also match the performance of mainstream commercial acoustic emission sensors. Technically, the design options with SiO_2 and Si_3N_4 cladding offer displacement sensitivity of $5.32\,V/nm$ and $3.95\,V/nm$, and velocity sensitivity of $78.55\ dB$ and $75.96\ dB$, respectively, around the centre frequency of $100\ kHz$. Both designs operate in a frequency range of $100 \sim 1000\ kHz$. Among them, the option with SiO_2 cladding provides higher sensitivity, while the option with Si_3N_4 cladding achieves a smaller footprint. The optimal solution can be determined by users according to the actual needs of the engineering application.

The above design outcomes are based on both theoretical analysis and numerical simulation. Thus, it is of necessity to revise the assumptions and designs based on extensive testings in the future. In addition to the specific design results, another important outcome of this work is the proposal of a design methodology for opto-mechanical acoustic emission sensors. This method includes, but is not limited to, the estimation of eigen frequencies of single- and multi-layer micro-machined membranes, the determination of rib waveguide deformation, and the optimization of opto-mechanical sensors with coupled design variables. Based on the experimental determination of necessary physical parameters, these

approaches allow for rapid designs of acoustic emission sensors and therefore provide convenience for designers.

During the design process, some experiences have been accumulated for later reference. For example, single-layer micro-machined membranes with rib waveguides may suffer from local deformation due to stress discontinuity on the surface, which leads to failure in operation. The multi-layer micro-machined membranes have two adjacent resonance peaks near the overall eigen frequency, so extra care needs to be taken in numerical simulations to properly select the simulation step size so to avoid skipping the resonance responses.

Despite the progress made in this project, there are still some valuable topics that remain to be investigated. For example, the non-axisymmetric vibration of micro-machined membranes are neglected in this study, while these vibration modes may also play an important role in the detection of AE signals. In addition, there is still a gap in the exploration of the optical connection and packaging of the opto-mechanical micro-chip sensors, which is important for AE systems operating outdoors for long periods of time. Further, the integration of the proposed optical AE sensors with already existing electronic and signal processing systems is also a worthy endeavor.

In the future, the real engineering application of photonic micro-mechanical acoustic emission sensors still requires extensive work. For example, as mentioned above, the assumptions and approximations in the design phase need to be checked carefully. Besides, processability verification and performance characterization are necessary for the operation and fabrication of proposed AE sensors.

References

[1] Wai-Fah Chen and Eric M Lui. *Principles of structural design*. CRC Press, 2005.

[2] Maria V Felice and Zheng Fan. “Sizing of flaws using ultrasonic bulk wave testing: A review”. In: *Ultrasonics* 88 (2018), pp. 26–42.

[3] Isaac Animah and Mahmood Shafiee. “Condition assessment, remaining useful life prediction and life extension decision making for offshore oil and gas assets”. In: *Journal of loss prevention in the process Industries* 53 (2018), pp. 17–28.

[4] C Guedes Soares and Yordan Garbatov. “Reliability of maintained, corrosion protected plates subjected to non-linear corrosion and compressive loads”. In: *Marine Structures* 12.6 (1999), pp. 425–445.

[5] Felix Rioja. “What is the value of Infrastructure Maintenance? A Survey”. In: *Infrastructure and land policies* 13 (2013), pp. 347–365.

[6] Edoka Augustine Ijigah et al. “An assessment of environmental impacts of building construction projects”. In: (2013).

[7] Mahmood Shafiee and John Dalsgaard Sørensen. “Maintenance optimization and inspection planning of wind energy assets: Models, methods and strategies”. In: *Reliability Engineering & System Safety* 192 (2019), p. 105993.

[8] Sandeep Kumar Dwivedi, Manish Vishwakarma, and Akhilesh Soni. “Advances and researches on non destructive testing: A review”. In: *Materials Today: Proceedings* 5.2 (2018), pp. 3690–3698.

[9] Stefano Mariani, Yuan Liu, and Peter Cawley. “Improving sensitivity and coverage of structural health monitoring using bulk ultrasonic waves”. In: *Structural Health Monitoring* 20.5 (2021), pp. 2641–2652.

[10] AR Dakak et al. “Deep learning-based defect detection in industrial CT volumes of castings”. In: *Insight-Non-Destructive Testing and Condition Monitoring* 64.11 (2022), pp. 647–658.

[11] Els Verstrynge et al. “Experimental study of failure mechanisms in brittle construction materials by means of x-ray microfocus computed tomography”. In: *Proceedings of the ninth international conference on fracture mechanics of concrete and concrete structures—FraMCoS-9. Berkeley, California, USA*. Vol. 29. 2016.

[12] Branko Šavija et al. “Corrosion induced cover cracking studied by X-ray computed tomography, nanoindentation, and energy dispersive X-ray spectrometry (EDS)”. In: *Materials and Structures* 48 (2015), pp. 2043–2062.

[13] Max Linke et al. “On the accuracy of monitoring inter-fibre fractures in composites using passive infrared thermography extended by microscopic analysis”. In: *Nondestructive Testing and Evaluation* 36.6 (2021), pp. 654–666.

[14] Quang Huy Tran et al. “Passive infrared thermography technique for concrete structures health investigation: case studies”. In: *Asian Journal of Civil Engineering* (2023), pp. 1–9.

[15] Siavash Doshvarpassand, Changzhi Wu, and Xiangyu Wang. “An overview of corrosion defect characterization using active infrared thermography”. In: *Infrared Physics & Technology* 96 (2019), pp. 366–389.

[16] Victor Giurgiutiu. *Structural health monitoring: with piezoelectric wafer active sensors*. Elsevier, 2007.

[17] Joseph L Rose. “A baseline and vision of ultrasonic guided wave inspection potential”. In: *J. Pressure Vessel Technol.* 124.3 (2002), pp. 273–282.

[18] Christian U Grosse et al. *Acoustic emission testing: Basics for research–applications in engineering*. Springer Nature, 2021.

[19] Charlotte Van Steen et al. “Localisation and characterisation of corrosion damage in reinforced concrete by means of acoustic emission and X-ray computed tomography”. In: *Construction and Building Materials* 197 (2019), pp. 21–29.

[20] Christopher B Scruby. “An introduction to acoustic emission”. In: *Journal of Physics E: Scientific Instruments* 20.8 (1987), p. 946.

[21] Arabinda Sharma and Neeraj Mehta. “Structural health monitoring using image processing techniques-a review”. In: *International Journal of Modern Computer Science* 4.4 (2016).

[22] A-D Nguyen and V Godinez. “Integrated health and corrosion monitoring systems in the aerospace industry”. In: *Corrosion Control in the Aerospace Industry*. Elsevier, 2009, pp. 151–171.

[23] JQ Huang. “Non-destructive evaluation (NDE) of composites: Acoustic emission (AE)”. In: *Non-Destructive Evaluation (NDE) of Polymer Matrix Composites*. Elsevier, 2013, pp. 12–32.

[24] DG Eitzen and HNG Wadley. “Acoustic emission: establishing the fundamentals”. In: *Journal of research of the National Bureau of Standards* 89.1 (1984), p. 75.

[25] Pooria Lotfollah Pahlavan et al. “Acoustic emission health monitoring of steel bridges”. In: *EWSHM-7th European Workshop on Structural Health Monitoring*. 2014.

[26] Daniel Tonelli et al. “Structural health monitoring based on acoustic emissions: validation on a prestressed concrete bridge tested to failure”. In: *Sensors* 20.24 (2020), p. 7272.

[27] Kanji Ono. “On Acoustic Emission Sensor Characterization”. In: *Journal of Acoustic Emission* 34 (2017), S10–S10.

[28] Amir Manbachi and Richard SC Cobbold. “Development and application of piezoelectric materials for ultrasound generation and detection”. In: *Ultrasound* 19.4 (2011), pp. 187–196.

[29] Jacques Curie and Pierre Curie. “Développement par compression de l’électricité polaire dans les cristaux hémièdres à faces inclinées”. In: *Bulletin de minéralogie* 3.4 (1880), pp. 90–93.

[30] Weijian Ding et al. “Cement-based piezoelectric ceramic composites for sensing elements: a comprehensive state-of-the-art review”. In: *Sensors* 21.9 (2021), p. 3230.

[31] Rui Guo et al. “Feasibility evaluation of the development of type 1-3 acoustic emission sensors for health monitoring of large bridge structures”. In: *Ceramics International* (2023).

[32] Simon Laflamme et al. “Roadmap on Measurement Technologies for Next Generation Structural Health Monitoring Systems”. In: *Measurement Science and Technology* (2023).

[33] Didem Ozevin. “MEMS acoustic emission sensors”. In: *Applied Sciences* 10.24 (2020), p. 8966.

[34] Jan Niklas Haus et al. “MEMS vibrometer for structural health monitoring using guided ultrasonic waves”. In: *Sensors* 22.14 (2022), p. 5368.

[35] Jan Niklas Haus et al. “Robust Pressure Sensor in SOI Technology with Butterfly Wiring for Airfoil Integration”. In: *Sensors* 21.18 (2021), p. 6140.

[36] Paul Muralt. “Recent progress in materials issues for piezoelectric MEMS”. In: *Journal of the American Ceramic Society* 91.5 (2008), pp. 1385–1396.

[37] Pauline Butaud et al. “Towards a better understanding of the CMUTs potential for SHM applications”. In: *Sensors and Actuators A: Physical* 313 (2020), p. 112212.

[38] Jonas Welsch et al. “Ultrathin, High Sensitivity Polymer-based Capacitive Micromachined Ultrasound Transducers (polyCMUTs) for Acoustic Emission Sensing in Fiber Reinforced Polymers”. In: *2022 IEEE International Ultrasonics Symposium (IUS)*. IEEE. 2022, pp. 1–5.

[39] Junaid Munir, Quratul Ain, and Hyunjoo Jenny Lee. “Reliability issue related to dielectric charging in capacitive micromachined ultrasonic transducers: A review”. In: *Microelectronics Reliability* 92 (2019), pp. 155–167.

[40] Yongfang Li et al. “Improved Piezoelectric MEMS Acoustic Emission Sensors”. In: *2021 21st International Conference on Solid-State Sensors, Actuators and Microsystems (Transducers)*. IEEE. 2021, pp. 238–241.

[41] Richard Soref. “The past, present, and future of silicon photonics”. In: *IEEE Journal of selected topics in quantum electronics* 12.6 (2006), pp. 1678–1687.

[42] Wouter J Westerveld and H Paul Urbach. *Silicon Photonics: Electromagnetic Theory*. IOP Publishing, 2017.

[43] Marianna Pantouvaki et al. “50Gb/s silicon photonics platform for short-reach optical interconnects”. In: *Optical Fiber Communication Conference*. Optica Publishing Group. 2016, Th4H–4.

[44] Ken Giewont et al. “300-mm monolithic silicon photonics foundry technology”. In: *IEEE Journal of Selected Topics in Quantum Electronics* 25.5 (2019), pp. 1–11.

[45] Erman Timurdogan et al. “AIM process design kit (AIMPDKv2. 0): Silicon photonics passive and active component libraries on a 300mm wafer”. In: *Optical Fiber Communication Conference*. Optica Publishing Group. 2018, M3F–1.

[46] Andy Eu-Jin Lim et al. “Review of silicon photonics foundry efforts”. In: *IEEE Journal of Selected Topics in Quantum Electronics* 20.4 (2013), pp. 405–416.

[47] Patrick Steglich et al. “Silicon photonic micro-ring resonators for chemical and biological sensing: A tutorial”. In: *IEEE sensors journal* 22.11 (2021), pp. 10089–10105.

[48] Suzanne M Leinders et al. “A sensitive optical micro-machined ultrasound sensor (OMUS) based on a silicon photonic ring resonator on an acoustical membrane”. In: *Scientific reports* 5.1 (2015), p. 14328.

[49] Griffiths and DavidJ. *Introduction to electrodynamics /-3rd ed*. Introduction to electrodynamics /-3rd ed, 2006.

[50] Rüdiger Paschotta. *Field guide to lasers*. Vol. 12. SPIE press Bellingham, 2008.

[51] Niels Quack et al. “MEMS-enabled silicon photonic integrated devices and circuits”. In: *IEEE Journal of Quantum Electronics* 56.1 (2019), pp. 1–10.

[52] James Owen Willberry, Mayorkinos Papaelias, and Gerard Franklyn Fernando. “Structural health monitoring using fibre optic acoustic emission sensors”. In: *Sensors* 20.21 (2020), p. 6369.

[53] Jaime Mata-Falcón et al. “Combined application of distributed fibre optical and digital image correlation measurements to structural concrete experiments”. In: *Engineering Structures* 225 (2020), p. 111309.

[54] TE Rudenko, AN Nazarov, and VS Lysenko. “The advancement of silicon-on-insulator (SOI) devices and their basic properties.” In: *Semiconductor Physics, Quantum Electronics & Optoelectronics* 23.3 (2020).

[55] Franz Laermer et al. “Deep reactive ion etching”. In: *Handbook of silicon based MEMS materials and technologies*. Elsevier, 2020, pp. 417–446.

[56] Wouter J Westerveld et al. “Sensitive, small, broadband and scalable optomechanical ultrasound sensor in silicon photonics”. In: *Nature Photonics* 15.5 (2021), pp. 341–345.

[57] *PECVD Overview from Oxford Instruments*. 2003. URL: `https://nanolab.berkeley.edu/public/manuals/process_manual.shtml`.

[58] Markku Tilli et al. *Handbook of silicon based MEMS materials and technologies*. Elsevier, 2020.

[59] WJ Westerveld et al. “Optical micro-machined ultrasound sensors with a silicon photonic resonator in a buckled acoustical membrane”. In: *2019 20th International Conference on Thermal, Mechanical and Multi-Physics Simulation and Experiments in Microelectronics and Microsystems (EuroSimE)*. IEEE. 2019, pp. 1–7.

[60] Leonard Meirovitch. *Analytical Methods in Vibrations*. 1st ed. Pearson, 1967. ISBN: 0023801409; 9780023801402.

[61] William Weaver Jr, Stephen P Timoshenko, and Donovan Harold Young. *Vibration problems in engineering*. John Wiley & Sons, 1991.

[62] Rudolph Szilard. “Theories and applications of plate analysis: classical, numerical and engineering methods”. In: *Appl. Mech. Rev.* 57.6 (2004), B32–B33.

[63] Vasile Nastasescu. “The Using of the Multilayer Plate Concept in the Calculus of Functionally Graded Plates”. In: *Applied Sciences* 12.21 (2022), p. 10695.

[64] Bradley Snyder and Peter O’Brien. “Packaging process for grating-coupled silicon photonic waveguides using angle-polished fibers”. In: *IEEE Transactions on Components, Packaging and Manufacturing Technology* 3.6 (2013), pp. 954–959.

[65] Wouter J Westerveld et al. “Characterization of integrated optical strain sensors based on silicon waveguides”. In: *IEEE Journal of Selected Topics in Quantum Electronics* 20.4 (2013), pp. 101–110.

[66] P Karasiński et al. “Optical rib waveguides based on sol-gel derived silica–titania films”. In: *Thin Solid Films* 519.16 (2011), pp. 5544–5551.

[67] Graham T Reed and Andrew P Knights. *Silicon photonics: an introduction*. John Wiley & Sons, 2004.

[68] Richard J Mathar. “Refractive index of humid air in the infrared: model fits”. In: *Journal of Optics A: Pure and Applied Optics* 9.5 (2007), p. 470.

[69] Calvin D Salzberg and John J Villa. “Infrared refractive indexes of silicon germanium and modified selenium glass”. In: *JOSA* 47.3 (1957), pp. 244–246.

[70] HH Li. “Refractive index of silicon and germanium and its wavelength and temperature derivatives”. In: *Journal of Physical and Chemical Reference Data* 9.3 (1980), pp. 561–658.

[71] Lihong Gao, Fabien Lemarchand, and Michel Lequime. “Exploitation of multiple incidences spectrometric measurements for thin film reverse engineering”. In: *Optics express* 20.14 (2012), pp. 15734–15751.

[72] Jan Kischkat et al. “Mid-infrared optical properties of thin films of aluminum oxide, titanium dioxide, silicon dioxide, aluminum nitride, and silicon nitride”. In: *Applied optics* 51.28 (2012), pp. 6789–6798.

[73] Kevin Luke et al. “Broadband mid-infrared frequency comb generation in a Si 3 N 4 microresonator”. In: *Optics letters* 40.21 (2015), pp. 4823–4826.

[74] Manfred Hammer. *Mode solver for 2-D multilayer waveguides, variational effective index approximation*. URL: `https://www.computational-photonics.eu/eims.html`.

[75] Wim Bogaerts et al. “Silicon microring resonators”. In: *Laser & Photonics Reviews* 6.1 (2012), pp. 47–73.

[76] Cinzia Sada, Dominik Gerhard Rabus, et al. “Integrated Ring Resonators A Compendium”. In: (2020).

[77] Antoine Brimont et al. “Low-loss and compact silicon rib waveguide bends”. In: *IEEE Photonics Technology Letters* 28.3 (2015), pp. 299–302.